IMPROVED CEMENT QUALITY AND GRINDING EFFICIENCY BY MEANS OF CLOSED MILL CIRCUIT MODELING

A Dissertation

by

GLEB GENNADIEVICH MEJEOUMOV

Submitted to the Office of Graduate Studies of
Texas A&M University
in partial fulfillment of the requirements for the degree of

DOCTOR OF PHILOSOPHY

December 2007

Major Subject: Civil Engineering

IMPROVED CEMENT QUALITY AND GRINDING EFFICIENCY

BY MEANS OF CLOSED MILL CIRCUIT MODELING

A Dissertation

by

GLEB GENNADIEVICH MEJEOUMOV

Submitted to the Office of Graduate Studies of
Texas A&M University
in partial fulfillment of the requirements for the degree of

DOCTOR OF PHILOSOPHY

Approved by:

Chair of Committee,	Dan Zollinger
Committee Members,	Dallas Little
	Donald Saylak
	Sergiy Butenko
	Vladimir Zhukov
Head of Department,	David Rosowsky

December 2007

Major Subject: Civil Engineering

ABSTRACT

Improved Cement Quality and Grinding Efficiency
by Means of Closed Mill Circuit Modeling. (December 2007)
Gleb Gennadievich Mejeoumov, B.S., Ivanovo State Power University, Russia;
M.S., Ivanovo State Power University, Russia
Chair of Advisory Committee: Dr. Dan Zollinger

Grinding of clinker is the last and most energy-consuming stage of the cement manufacturing process, drawing on average 40% of the total energy required to produce one ton of cement. During this stage, the clinker particles are substantially reduced in size to generate a certain level of fineness as it has a direct influence on such performance characteristics of the final product as rate of hydration, water demand, strength development, and other. The grinding objectives tying together the energy and fineness requirements were formulated based on a review of the state of the art of clinker grinding and numerical simulation employing the Markov chain theory.

The literature survey revealed that not only the specific surface of the final product, but also the shape of its particle size distribution (PSD) is responsible for the cement performance characteristics. While it is feasible to engineer the desired PSD in the laboratory, the process-specific recommendations on how to generate the desired PSD in the industrial mill are not available.

Based on a population balance principle and stochastic representation of the particle movement within the grinding system, the Markov chain model for the circuit consisting of a tube ball mill and a high efficiency separator was introduced through the matrices of grinding and classification. The grinding matrix was calculated using the selection and breakage functions, whereas the classification matrix was defined from the Tromp curve of the separator. The results of field experiments carried out at a pilot cement plant were used to identify the model's parameters. The retrospective process

data pertaining to the operation of the pilot grinding circuit was employed to validate the model and define the process constraints.

Through numerical simulation, the relationships between the controlled (fresh feed rate; separator cut size) and observed (fineness characteristics of cement; production rate; specific energy consumption) parameters of the circuit were defined. The analysis of the simulation results allowed formulation of the process control procedures with the objectives of decreasing the specific energy consumption of the mill, maintaining the targeted specific surface area of the final product, and governing the shape of its PSD.

DEDICATION

To my mother and father

ACKNOWLEDGMENTS

First of all, I would like to thank my academic advisor Dr. Dan Zollinger and the rest of the committee members: Dr. Dallas Little, Dr. Don Saylak, Dr. Sergiy Butenko, and Dr. Vladimir Zhukov for their expert advice in the preparation of this dissertation.

I would like to express particular gratitude to my teacher and mentor, Dr. Saylak, for his faithful support of all of my undertakings during my studies at Texas A&M University. Without his fatherly advice, timely jokes, and sound auspices, my stay in the program would not have been the same. His remarkable eloquence, tireless perseverance, and strong affection for applied research will always keep me enthused. I thank Dr. Saylak for his every day encouragements and editorial input to this dissertation.

I am greatly indebted to my dear teachers, Dr. Vadim Mizonov and Dr. Vladimir Zhukov, whom I first met in the classroom in my freshman year of high school, for their enormous contribution to my scholastic attainments and their patient guidance in my search for scientific self-actualization. I truly admire their great passion and novel approach for teaching and research. I will always dwell on the special atmosphere they created at the Department of Applied Mathematics at Ivanovo State Power (Engineering) University and the enlightening conversations they inspired at the department's tea table. Without their direction and support, this work simply would not have been possible.

I gratefully acknowledge the role Ms. Dorit Hammerling and Mr. Mark Morgan played in granting me the opportunity to perform this research and gain the invaluable hands-on experience in the field. My special thanks go to my friend and colleague, Ross Taylor, for his generosity in sharing with me his profound knowledge and experience in manufacturing and process control.

I would like to express my sincere appreciation to my close friends: Tracy Lostak, Bogusia Styblinski, Tomasz Styblinski, Ania Kaminski, Tatyana Paramonova, Xenia Sharonova, Kim Tessanne, Edith Arambula, Nina Britt, Anna and Stanislav Glagolenko, Amaury Vuillaume, David Haubrich, Reza Ashtiani, Jose Gavinha, and everybody else who cares about me, for their faithful support of my endeavors during the past years.

Finally, I am endlessly grateful to my parents for their love, support, and patience.

NOMENCLATURE

ASTM	American Society for Testing and Materials
B	Flow rate of a material stream, mass per time unit
Blaine	Specific surface area value as per ASTM C 204, m^2/kg or cm^2/g
C	Matrix of classification
C.L.	Circulation load
F	Particle size distribution state vector
f(x)	Density probability (frequency) function, percent or fraction
G	Matrix of grinding
GEC	Grade efficiency curve
HES	High efficiency separator
M	Matrix of the closed grinding circuit
PDH	Process data historian
PSD	Particle size distribution
Q(x)	Cumulative passing function, percent or fraction
rpm	Revolutions per minute
RR	Rosin-Rammler
STD	Standard deviation
tph	Tons per hour
w/c	Water to cement ratio
x	Particle size, μm
x_{50}	Cut size of the separator

TABLE OF CONTENTS

Page

Page

LIST OF FIGURES

Page

Page

LIST OF TABLES

Page

1. INTRODUCTION

1.1. CEMENT AS A CONSTRUCTION MATERIAL

Cement is a common construction material; a binder in mortars and concretes that hardens in the presence of water. Cement is called *hydraulic*, when the hardened product is stable in an aqueous environment. The most widespread hydraulic cement today is *portland cement* – a finely ground gray-to-white powder composed primarily of calcium silicates, calcium aluminates, and calcium ferrites, derived from mineral ingredients (Figure 1.1).

Figure 1.1. Portland Cement (after Bhatty et al., 2004).

When mixed with water, portland cement sets (stiffens) in a few hours and hardens over a period of weeks and months. These phenomena are caused by chemical reactions associated with hydration between the components of cement and water.

The most common use of portland cement is in the production of concrete. Concrete is a composite consisting of aggregate (gravel and sand), cement, and water. As a construction material, concrete can be cast in almost any shape desired, and once hardened, can become a structural (load bearing) element. Portland cement is also used in mortars (with sand and water only) for plasters and screeds, and in grouts (cement-water mixes) placed into gaps to consolidate brick walls, foundations, etc.

The format of this dissertation follows the *Journal of Materials in Civil Engineering*.

1.2. CEMENT MANUFACTURING PROCESS DESCRIPTION

There are three fundamental stages in the cement manufacturing process:

- Raw mix preparation
- Clinker formation
- Cement grinding

1.2.1. Raw Mix Preparation

The chemical analysis of the raw materials is expressed in terms of oxides and the most important of these are CaO, SiO_2, Fe_2O_3, and, Al_2O_3. Theoretically, any material that can contribute these oxides may constitute the raw mixture.

The major raw mineral used in cement production that provides CaO is limestone ($CaCO_3$). It is usually quarried from a calcareous rock, which in some locations already has the desired mineralogical composition. The rest of the oxides are obtained by the addition of clay or shale, which are complementary with limestone in meeting the stoichiometric needs for developing portland cement. Minor adjustments to the chemistry of the cement are made by adding sand (SiO_2), iron ore (Fe_2O_3), and/or bauxite (Al_2O_3).

After the raw materials have been quarried and brought to the plant, the individual *raw mix* ingredients are crushed to particle sizes below 100-120 mm, proportioned to produce the desired cement chemistry, and supplied to a *raw mill* shown in Figure 1.2. This schematic illustrates a dry cement manufacturing process, which operates with a nearly dry raw mix containing less than 20% moisture by mass. This is opposed to a wet process, in which water is added to the raw mix to form a slurry, which is then transported to the kiln.

The raw mill shown in Figure 1.2 is a vertical roller mill with an internal particle classification. In this arrangement, the raw mix is fed onto a rotating table, on top of which four steel rollers compact the material under 1 MPa pressure. An upward stream of hot gas sweeps the ground material from the rotating table to a separator, which rejects the oversized particles back to the table. The finer particles are carried out with the gas flow to the raw mix storage silo or directly to the next stage of the manufacturing process.

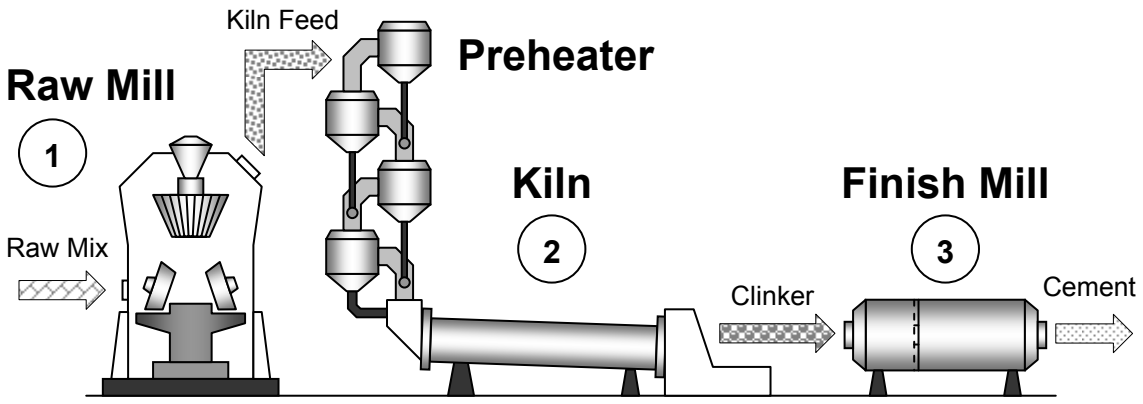

Figure 1.2. A Simplified Schematic of a Dry Cement Manufacturing Process.

In case of a dry process, the raw mix goes through drying, blending, and pulverization inside the raw mill. All these generate a suitable material for clinker production – so called *kiln feed*. The hot exhaust gases from the kiln are usually directed into the raw mill for drying the raw mix and improving the overall plant efficiency by reusing the otherwise squandered hot gases. The pulverization reduces the raw mix to a powder with particle sizes less than 100-150 μm. This is necessary for producing a well-blended, chemically-homogeneous mix that will facilitate a thorough completion of the chemical reactions in the kiln.

1.2.2. Clinker Formation

The formation of clinker requires very high temperatures. Modern dry process cement plants use *preheater* towers such as shown in Figure 1.2 to pre-process the kiln feed and thus save energy. The hot exit gases from the kiln heat the raw materials as they swirl down through the cyclones of the preheater tower, so the kiln has less subsequent processing to do. In addition, the preheater may be equipped with a precalciner – an extra heat generating unit, which drives off carbon dioxide (CO_2) from the limestone ($CaCO_3$) in the raw mix isolating calcium oxide (CaO) for further chemical reactions in the kiln. Up to 95% of the required calcination may be achieved in the precalciner.

The pre-processed raw materials then enter a large rotating furnace called the *kiln* (Figure 1.2). It is a sloped cylinder, lined with firebricks, which turns at about one to three revolutions per minute. From the preheater tower, the kiln feed enters the kiln at the upper end and moves down through progressively hotter zones toward the flame. Different fuels, such as powdered coal, natural gas, and petroleum coke as well as alternative waste fuels (e.g., old car tires), are used to produce that flame. Here in the hottest part of the kiln, the raw materials reach the sintering temperature of about 1400-1450°C and become partially molten.

A complex succession of chemical reactions take place as the temperature rises, converting the calcium and silicon oxides into calcium silicates – cement's primary constituent. At the lower end of the kiln, the raw materials emerge as a new nodular substance called *clinker*.

The four major mineralogical phases of clinker are:

- $3CaO{\cdot}SiO_2$ – tricalcium silicate; alite (C_3S)
- $2CaO{\cdot}SiO_2$ – dicalcium silicate; belite (C_2S)
- $3CaO{\cdot}Al_2O_3$ – tricalcium aluminate; aluminate (C_3A)
- $4CaO{\cdot}Al_2O_3{\cdot}Fe_2O_3$ – tetracalcium aluminoferrite; ferrite (C_4AF)

Items in parentheses indicate cement industry notation for the clinker phases. According to Zhang and Napier-Munn (1995), the alite phase, due to its reactive nature, is responsible for the setting characteristics and development of the early strength of cement (1 to 28 days). Belite is known to contribute mainly to the development of a late strength (28 days plus). Aluminate is the most reactive of all clinker phases and responsible for a very early strength (1-2 days). Ferrite has little effect on properties of cement other than color.

After exiting the kiln, clinker falls onto a grate cooled by large air fans. To save energy, the heat recovered from the cooling process is recirculated back to the kiln or preheater tower. Once clinker is cooled, it is ready for the final stage of the cement manufacturing process – pulverization in a *finish mill*.

1.2.3. Cement Grinding

Clinker is transported to the finish mill (see Figure 1.2) by a conveyor belt to be ground into a fine powder – cement. A small amount of gypsum is added during grinding to control the set properties of the produced cement. It is quite typical to add a certain amount of water and small quantities of organic grinding aids to control mill temperature and facilitate the pulverization process. Blended cements and masonry cements may include large additions (up to 40%) of natural pozzolans, fly ash, limestone, silica fume, or metakaolin (Bhatty et al., 2004).

The most common equipment for cement grinding is a ball mill – a horizontal steel tube filled with steel balls. Material fed through the mill is crushed by impact and ground by attrition between the balls. For increased efficiency, the closed-circuit systems are widely used in cement grinding, in which the material exiting the ball mill is directed to the separator and divided into coarse and fine fractions. The coarse fraction is sent to the mill's inlet for regrind, whereas the fine fraction becomes the cement.

The rate of initial reaction of cement and water is directly proportional to the specific surface of cement (Mehta, 1986); therefore the grinding process is closely controlled to obtain a product with the desired fineness characteristics: targeted percent passing through a 45-μm sieve and specific surface area (the total particle surface area of a unit mass of cement).

The ground cement is conveyed by belt or powder pump into a silo for storage. At this stage, it is ready for bagging and/or shipping in bulk by trucks, rail, or barge.

1.2.4. Cement Manufacturing Energy Demand

The production of cement is an energy-intensive process. The typical energy consumption of a modern cement plant is about 110-120 kWh per ton of produced cement (Alsop, 2001). While the continuously increasing world's cement demand grows, the plant's energy demand grows as well. Despite the technological innovations in recent decades targeted at improving the efficiency of the manufacturing process (dry process vs. wet; use of preheaters, precalciners, high efficiency dynamic separators, etc.), a cement plant today has a steadily increasing overall power consumption due to higher

production rates, reversion to coal, increased fineness of cement, and more rigorous demands for environmental protection (Alsop, 2001). According to Bhatty et al. (2004), usage of more efficient equipment, utilization of waste materials and fuels, relentless process control of the manufacturing equipment, implementation of a plant-wide energy management strategy, preventive maintenance, and personnel training are among measures that can help to reduce the electrical and fuel consumption per unit of output of the various cement production stages.

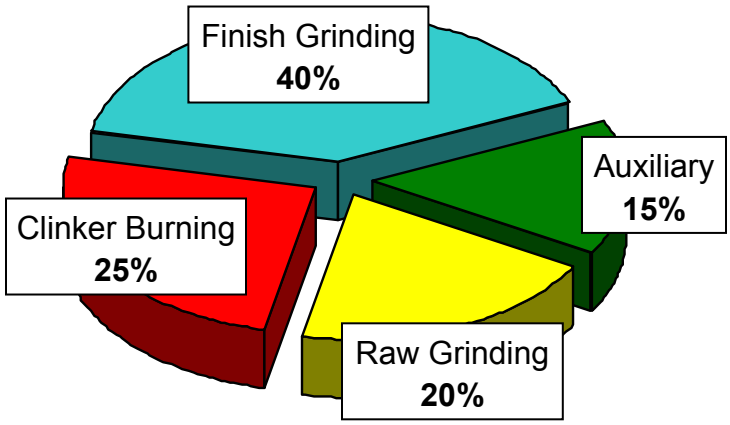

Figure 1.3. Energy Distribution among Cement Manufacturing Equipment.

A common distribution of the total energy consumed by a cement plant among the stages of the manufacturing process is shown in Figure 1.3. While the kiln is the largest moving piece of equipment at the cement plant, it is not the most energy-intensive one, utilizing only 25% of the plant's energy. The most energy-consuming cement manufacturing process is finish grinding, drawing, on average 40%, of the total energy required to produce a ton of cement (Alsop, 2001). Such a high value can be justified by the fact that a considerable amount of energy supplied by the mill's motor is released in the form of heat, produced by friction in the grinding media. Furthermore, the grinding energy demand increases hyperbolically with increasing fineness of the cement particles (Bhatty, 2004).

1.3. FINISH MILLING EFFICIENCY IMPROVEMENT

The term "improving efficiency" suggests decreasing the power consumption of the finish grinding; and being the most energy-consuming stage of the cement manufacturing process, it is, indeed, the most likely place to save. However, efficiency can also be viewed as achieving the most beneficial properties of the final product that deliver the best performance characteristics of the cement. First of all, the cement performance is a direct consequence of the clinker chemistry and mineralogy as it is shown in Figure 1.4 via arrow (1). The formation of the clinker mineralogical phases takes place inside the kiln so that the finish grinding has virtually no influence on the final composition of the produced cement, except for the inclusion of certain amounts of gypsum and other additives. The main impact that the finish milling has on the cement's performance characteristics is achieved through the fineness properties of the final product.

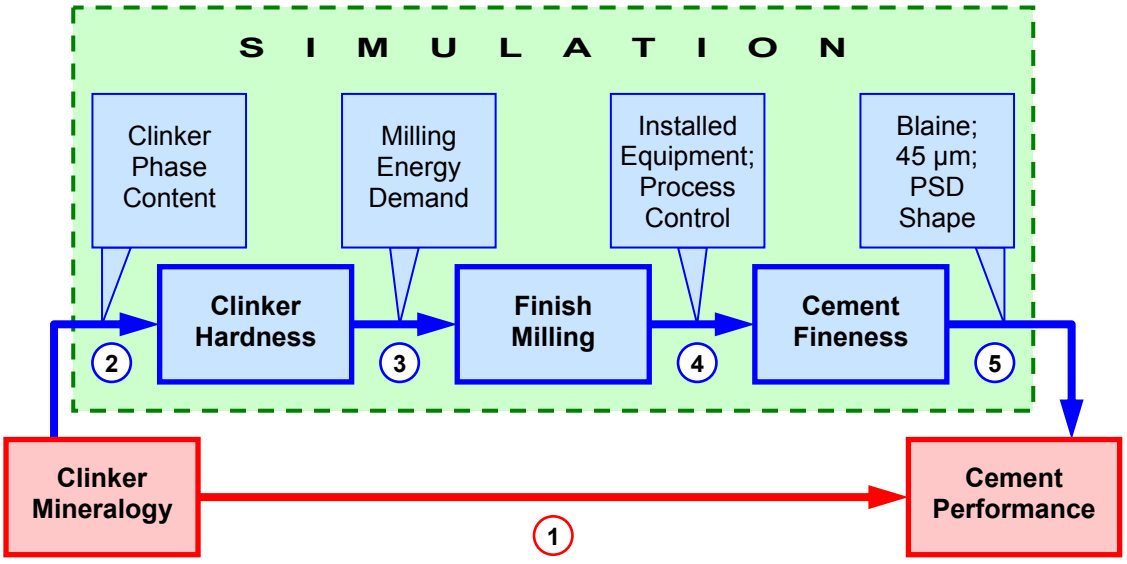

Figure 1.4. Factors of the Finish Grinding Influencing the Cement Performance.

The mineralogical composition defines the hardness of the clinker nodules: see arrow (2) in Figure 1.4. The hardness of clinker accounts for the specific energy demand of the grinding process: arrow (3). The harder the nodule, the more energy is required to

break it into pieces. The installed grinding equipment and the way the equipment is controlled determine the fineness properties of the product: arrow (4). Ultimately, different aspects of the fineness (specific surface area, amount of the material passing through a certain sieve size, and shape of the product's particle size distribution) have an effect on the performance characteristics of the produced cement: arrow (5).

The main goal of the proposed dissertation was to reveal the relationships among the factors, affecting the finish grinding process (see Figure 1.4). To reduce the volume of otherwise required experimental work, the numerical modeling and simulation were employed to examine these relationships. The modeling was performed using the Markov chain theory, which was shown as a suitable and effective tool in simulating the grinding process in a closed circuit. Knowing the relationships among the cement's performance characteristics, its fineness properties, process parameters of the circuit, and hardness of the clinker nodules, it became possible to suggest the process control steps towards improving both *energy* and *fineness* aspects of efficiency of the cement finish grinding.

1.4. RESEARCH OBJECTIVES AND OUTLINE OF THE DISSERTATION

This dissertation concentrates on the following objectives:

1. To reveal the relationships between the fineness aspects of the cement (specific surface area, shape of the particle size distribution, etc.) and its performance characteristics via a literature review.
2. To apply the Markov chain theory to simulate clinker grinding in a closed circuit.
3. To arrange and complete a sampling procedure at a pilot cement plant.
4. To perform analysis of the field data obtained in (3).
5. To identify the plant-specific values of the model parameters based on (4).
6. To conduct numerical simulation and analysis of the grinding circuit parameters, affecting production rate, particle size distribution of the final product, and specific energy consumption of the mill, using the model identified in (5).
7. Based on findings in (6), to suggest the energy and product quality objectives of the grinding process and outline the regulatory steps to achieve them.

In the beginning, this dissertation reviews the state of the art of clinker grinding. It shows that the cement performance characteristics depend on its fineness properties, whereas the current cement fineness requirements set the targets for the intensity of clinker reduction. The grinding equipment then produces the required fineness by utilizing various mills and separators. Simulation and analysis efforts are used to improve the energy efficiency of the grinding equipment, and the Markov chain model stands as a suitable and accurate tool for modeling and analyzing the cement milling circuits.

The detailed description of the Markov chain model reveals the underlying principles of the approach and presents matrices of grinding and classification. The section on the field sampling depicts how the on-site procedure at a pilot cement plant was fulfilled in order to obtain the data for identification and validation of the model. The numerical simulation performed to produce cement of the targeted fineness and improve the milling efficiency is described next. The simulation results allowed an outlining of the control strategy for the pilot milling circuit, which is presented in the subsequent section. Conclusions and recommendations for future work finalize the dissertation.

2. STATE OF THE ART OF CLINKER GRINDING AND SIMULATION

This section of the dissertation provides an overview of a modern state of clinker grinding technology, cement fineness requirements, finish mill circuit simulation, and automated control.

2.1. CEMENT FINENESS AND ITS SIGNIFICANCE

A lot of research work has been done examining the relationship between the portland cement particle fineness and performance properties of the cement paste such as the hydration kinetics, setting time, and others. To describe this relationship, it is necessary to assign some numerical values to the cement fineness characteristics. These values should be clearly defined, unique, and measurable in practice.

2.1.1. Cement Fineness Characteristics

Behavior of cement is strongly dependent on the properties of the individual particles, and the size effects become more important as the particles become smaller. However, the evaluation and precise definition of particle size are not simple tasks.

Physical characterization of cement, or any powder, would be much easier if all the particles were spheres and of the same size. Unfortunately, it is not the case since systems composed of identical particle sizes are extremely rare and the individual characteristics vary from one particle to another.

The principal particle characteristic is its size and can be represented as a linear dimension, an area (e.g., surface area), a volume, or a mass (Fuerstenau and Han, 2003). The relationships among these different representations depend on particle shape and, in case of mass, density.

For a sphere of diameter x and density ρ, the surface area, A_s, is given by:

$$A_s = \pi x^2 \tag{2.1}$$

The volume, V, is given by:

$$V = \frac{\pi x^3}{6} \tag{2.2}$$

The mass, m, is given by:

$$m = \rho \frac{\pi x^3}{6} \tag{2.3}$$

In general, the particle size characteristic of a powder can be represented by a distribution expressed as discrete values or continuous functions in either incremental (frequency) or cumulative form. Regardless of how the size is measured, the almost universal practice is to represent size as a linear diameter, x, of an equivalent sphere (Fuerstenau and Han, 2003). Size is an intrinsically continuous variable, and corresponding data are usually classified into appropriate size intervals.

2.1.1.1. Particle Size Distribution

Different methods for measuring particle size distribution (PSD) involve different quantity representations. Counting methods usually give number distributions, gravimetric methods give mass or volume distributions, and some optical methods give area distributions. To describe the distribution of particle sizes, we must represent:

- The value of the size itself
- The relative amount of material that has that size value

The most common way to obtain the PSD of a dry powder material by mass is to perform a dry sieve analysis. The Tyler and U.S. Standard sieve series are most commonly used for this procedure. Both series use a geometric progression of sieve apertures with a constant ratio between adjacent members. The number in the sieve notation represents the amount of mesh openings per linear inch, e.g., No. 200-sieve.

The sieves are stacked on top of one another in such a way that the sieve with a largest mesh opening is at the top of the stack and the sieve with a smallest mesh opening is at the bottom and followed by a pan. A representative sample of the powder material of known mass is placed in the top sieve, and the whole stack is mechanically

vibrated for a fixed period of time letting particles drop through the sieves. The mass of the material retained on each sieve is measured and converted into percentages of the total mass of the sample. A good way to check the overall procedure is to compare the initial mass of the sample with the sum of masses retained on individual sieves. Some loss of the material is inevitable due to sticking of fine particles to the sieve surfaces and in apertures. These losses should not exceed 1% (Fuerstenau and Han, 2003).

The obtained PSD data can be assessed by tabular, graphical, or mathematical representations. The tabular PSD of an arbitrary material is shown in Table 2.1. This table shows relative fractions of the material retained on individual sieves with respect to the total mass of the measured sample (frequency) as well as cumulative percentage values of the material that passed through a corresponding sieve.

Table 2.1. Tabular Representation of Particle Size Distribution.

Sieve Number	Sieve Aperture, *x*	Sieve Mass	Sieve + Material Mass	Material Mass	Individual Retained, *f(x)*	Cumulative Passing, *Q(x)*
#	μm	g	g	g	%	%
3/4 "	19050	1047.2	1047.2	0.0	0.0	100.0
3/8 "	9525	997.3	1695.7	698.4	19.2	80.8
#4	4750	1127.9	2347.0	1219.1	33.6	47.2
#8	2360	839.2	1601.8	762.6	21.0	26.2
#16	1180	690.4	1068.0	377.6	10.4	15.8
#30	600	670.2	926.3	256.1	7.1	8.8
#50	300	574.0	746.5	172.5	4.8	4.0
#100	150	671.9	765.3	93.4	2.6	1.4
#200	75	688.7	718.4	29.7	0.8	0.6
Pan	-	662.7	684.9	22.2	0.6	0.0
		Mass After Sieving		**3631.6**		
		Initial Mass		**3632.3**		
		Percent Mass Loss		**0.02%**		

The data shown in Table 2.1 is also presented graphically in Figure 2.1. Since the sequence of the sieve aperture sizes form a geometric progression, it is convenient to plot the data using a logarithmic scale along the *x*-axis. This straightens the S-shaped

cumulative curves and helps interpreting the PSD data. The graph shows the individual percent retained and cumulative percent passing values in discrete and continuous modes.

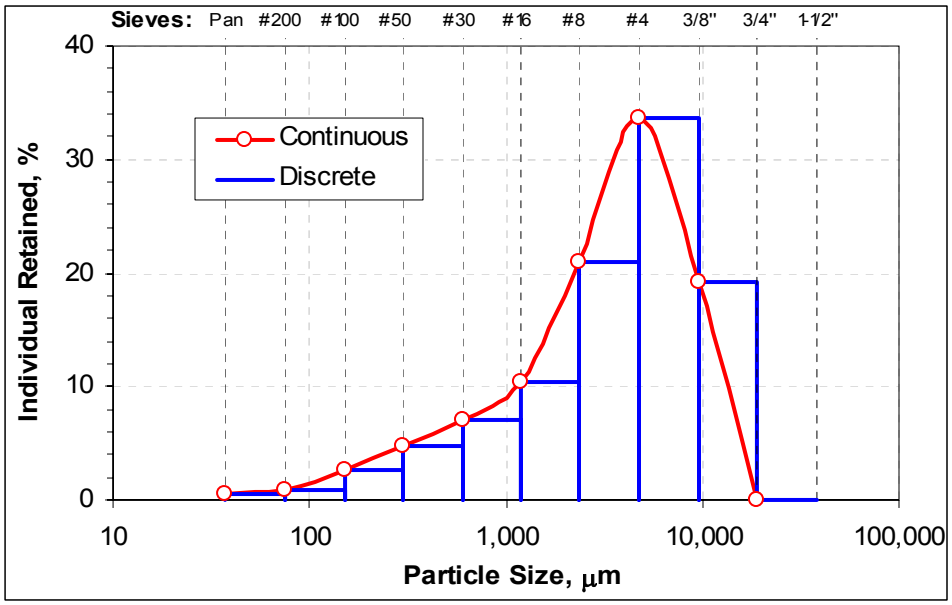

(a)

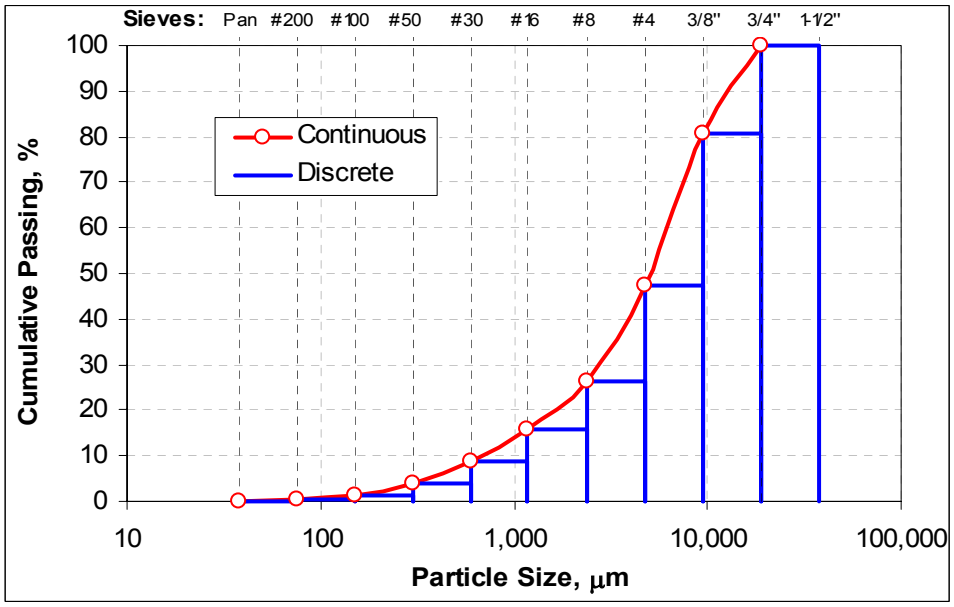

(b)

Figure 2.1. Graphical Representation of Particle Size Distribution (a – Individual Retained PSD; b – Cumulative Passing PSD).

Despite the versatility of the sieving procedure and its applicability to a majority of dry powders, it is not quite suitable for cement. The portland cement particles are so small that the sieve analysis method can not provide a good representation of the sample throughout the entire range of particle sizes. Alsop (2001) reports that the two smallest sieves normally used in the cement industry have apertures of 45 μm (No. 325-sieve) and 75 μm (No. 200-sieve). The cement particle sizes span between approximately 0.1 and 100 μm, and 90-95% of the cement material turns out to be finer than 45 μm. Other measuring techniques should be utilized to obtain a meaningful PSD of the cement.

There is only one standardized test procedure to characterize the PSD of cement: ASTM C 115 "Standard Test Method for Fineness of Portland Cement by the Turbidimeter" (Wagner test). It is really designed to determine the "fineness" of cement and based on sedimentation of cement powder dispersed in kerosene. This method can produce the PSD in a much broader spectrum than the sieve analysis procedure, but it is limited in measuring the cement particles to a minimum size of 7.5 μm.

Besides ASTM C 115 method, today there is no generally recognized method for determining the complete PSD of the cement powder. ASTM committee C01.25.01 has organized a research program to develop a standard test method for determining the cement PSD and establish a reference distribution using a standard cement sample. A report prepared by National Institute of Standards and Technology (U.S. Department of Commerce) summarizes the various approaches available to measure the PSD of cement and analyzes the data generated throughout the program (Ferraris et al., 2002).

According to Ferraris et al. (2002), the particle size measurement methods used in characterizing the cement powders include, but not limited to:

- Laser Light Scattering (Wet and Dry)
- Electrical Zone Sensing (Coulter Principle)
- Sedimentation (X-Ray and Optical Sensing)
- Scanning Electron Microscopy (Particle Counting)
- Sieving

The laser light scattering techniques are becoming more available, less expensive, and thus, more popular for characterizing the fine particles. In the cement industry, the laser scattering measurement with dispersion of the cement powder in liquid is currently the most frequently used method (Ferraris et al., 2002). Laser light scattering system is not limited to any particular size and constrained only by the equipment utilized.

The Fraunhofer diffraction and Mie scattering theories underlie the measuring principles of the most modern laser scattering size analyzers. The Mie scattering theory is derived from a strict application of Maxwell's Electromagnetic Equation. From this theory, it is possible to determine the intensity of the scattered light, when the particle is illuminated from any arbitrary angle. The angular scattering patterns depend on the relative refractive index and particle size; therefore, it is possible to calculate the size of a particle by comparing the observed scattering pattern with the theoretical derivations.

According to the Fraunhofer diffraction theory, when a suspension of particles is illuminated by a beam of light of a known wave length, a certain diffraction pattern is produced on the surface of a detector. This pattern consists of a series of concentric rings, which radii are uniquely related to a particular particle size (Fuerstenau and Han, 2003).

A typical particle size distribution of a Type I portland cement sample is shown in Figure 2.2. It was obtained in the laboratory conditions using Horiba Laser Scattering Particle Size Analyzer LA-910. This analyzer was the principal particle size measuring device for this study and has the following characteristics:

- Range of Measured Particle Sizes: 0.02 to 1020 μm
- Light Sources: 632.8 nm He-Ne laser, 1 mW; Tungsten halogen lamp 50 W
- Photo-cell detectors: 18-divison, ring shaped silicon photo-diode
- Mechanical stirrer: speed of up to 1,000 rpm
- Circulation pump: discharge volume of 1,000 ml/min
- Ultrasonic chamber: 39 kHz, 40 W

The graphical representation of the PSD created by the laser scattering device is identical to that of the sieve analysis procedure. Even though the cement particles are not "retained" on any kind of sieves inside the laser analyzer, the measured data is reported

for a grid of fixed size values. For the working range between 0.02 and 1020 µm, Horiba LA-910 produces a grid of 81 data points (80 size intervals) that are associated with the individual retained and cumulative passing values.

The vertical dashed lines in Figure 2.2 represent apertures in the sieves employed by the cement industry at the lower size end: 45 µm for sieve No. 325, 75 µm for sieve No. 200, and 150 µm for sieve No. 100. This plot shows that approximately 94% of the tested cement particles are smaller than 45 µm (sieve No. 325), whereas virtually all particles would pass through the 75-µm openings of a No. 200 sieve.

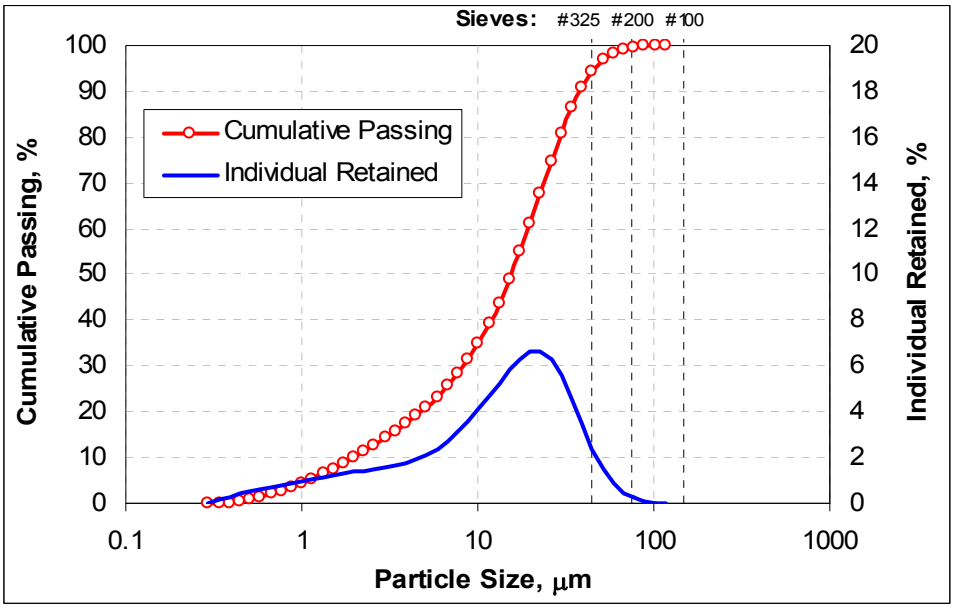

Figure 2.2. Typical Particle Size Distribution of a Type I Portland Cement Sample.

The particle size distribution can be characterized by several parameters adapted from the statistical data analysis:

- **Mode:** the most frequently occurring particle diameter (corresponding to the maximum point on the individual retained frequency plot).
- **Median:** the particle size equivalent to 50% of the cumulative distribution; half of all particles are smaller than this size and the other half are larger.

- **Mean:** the average particle diameter, defined as:

$$Mean = \sum_i x_i f(x_i), \tag{2.4}$$

where,

i – Count of particle size intervals (fractions) between the "sieves",

x_i – Typical diameter in the i-th size fraction (μm),

$f(x_i)$ – Normalized frequency value in the i-th size interval.

- **Standard Deviation:** the measure of degree of data spread, defined as:

$$STD = \sqrt{\sum_i (x_i - Mean)^2 f(x_i)}, \tag{2.5}$$

where,

Mean – Mean diameter, defined by Equation (2.4).

- **Coefficient of Variation:** standard deviation divided by mean diameter:

$$C.V. = \frac{STD}{Mean} \tag{2.6}$$

While the tabular and graphical representations provide comprehensive data on the particle size distribution of a powder, there is a need to reduce this data to only a few number of parameters for analysis and modeling purposes. For this, a mathematical representation of the PSD is utilized.

2.1.1.2. Rosin-Rammler Representation of PSD

Several algebraic functions that have been developed to describe size distributions of powders can be applied to cement. The use of a mathematical function allows instant graphical representation of the PSD and offers numerous opportunities for interpolation, extrapolation, and comparison of the data among different powder systems.

Typically, the functions representing cumulative PSD increase monotonically from 0 to 1 and have a number of parameters (two or three) that can be adjusted to achieve the best fit with the measured data.

Delagrammatikas and Tsimas (2004) as well as other authors summarized a list of two-parameter functions that are most commonly used to describe PSD of a fine powder resulting from a grinding process. These functions are shown in Table 2.2.

Table 2.2. Two-Parameter Particle Size Distribution Functions.

Commonly Used Function Name	**Cumulative Fraction Passing Formula, *Q(x)***	**Significance of Size Factor, d_0**	**Significance of Spread Factor, *n***
Logarithmic-Normal	$erf\left[\frac{\ln(x/d_0)}{n}\right]$	Median particle size	Standard deviation
Rosin-Rammler, or Weibull (in statistics)	$1-\exp\left[-\left(\frac{x}{d_0}\right)^n\right]$	Size for $Q(x)$ = 0.632	Slope of straight line*
Gates-Gaudin-Schumann	$\left[\frac{x}{d_0}\right]^n$	Max. particle size	Slope of straight line*
Gaudin-Meloy	$1-\left[1-\frac{x}{d_0}\right]^n$	Max. particle size	Slope of straight line*

* When plotted in log-log coordinates

The two parameters in use are:

- Size factor, d_0, and
- Spread factor, n

The size factor, d_0, is a characteristic particle size of the distribution. In the presented functions, it's either a measure of an average or maximum particle size in the PSD. The size factor indicates how fine the powder is, so the lower d_0 value corresponds to a finer material. On the other hand, the spread factor, n, is a measure of the width of the size distribution. When it appears as an exponent in the equation, the higher n value means a narrower PSD. Generally, the size and spread factors are used in parametric analysis of the PSD data (Djamarani and Clark, 1997).

The three-parameter PSD functions also include a factor accounting for the skewness of the size distribution, although, this introduces additional complexity to the function that can be rarely justified (Kelly and Spottiswood, 1982).

Bhatty et al. (2004) reported the Rosin-Rammler (RR) distribution function as being the most widely applied in the cement industry. Delagrammatikas and Tsimas (2001) explained this by analyzing the four functions shown in Table 2.2 and concluding that RR distribution provides the best results for two reasons. It delivers a good approximation of the ground clinker data as well as achieves the best representation of the skewness of the cement PSD without a need for an extra skewness parameter.

The Rosin-Rammler distribution describes the PSD in exponential form:

$$Q(x) = 1 - \exp\left[-\left(\frac{x}{d_0}\right)^n\right], \tag{2.7}$$

where,

x – Measured particle sizes, μm;

$Q(x)$ – Cumulative fraction passing function.

In order to apply the RR distribution and obtain the parameters d_0 and n, the RR function should be transformed in the following manner. By taking the natural logarithm of both sides twice, Equation (2.7) can be rewritten as:

$$\ln\ln\left(\frac{1}{1-Q(x)}\right) = n\ln(x) - n\ln(d_0) \tag{2.8}$$

A plot of Equation (2.8) should now yield a straight line:

$$y_2 = \alpha\, y_1 + \beta, \tag{2.9}$$

where,

α and β – Coefficients of a linear regression.

By comparing Equations (2.8) and (2.9), it can be easily seen that:

$$n = \alpha \tag{2.10}$$

And by solving Equations (2.8) and (2.9) for d_0 for a case, where $y_2 = 0$, we have:

$$d_0 = \exp\left(-\frac{\beta}{\alpha}\right), \tag{2.11}$$

and:

$$\ln\ln\left(\frac{1}{1-Q(x)}\right) = 0, \quad \text{or} \quad \frac{1}{1-Q(x)} = e. \tag{2.12}$$

Solving Equation (2.12), $Q(x) = 0.632$ or 63.2%. This means that the size factor, d_0, is the particle size that corresponds to a 63.2% cumulative passing value on the measured distribution curve.

Figure 2.3 illustrates construction of the Rosin-Rammler distribution for the same PSD data that was introduced earlier in Figure 2.2. The estimation of the RR parameters is shown in Figure 2.3(a). Here, the measured PSD data was first plotted in the RR coordinates to satisfy the mathematical form provided by Equation (2.8), and then the straight line was fitted to the data points using the least squares method to obtain the coefficients of Equation (2.9). Figure 2.3(b) displays the RR curve in comparison with the measured PSD cumulative data in the conventional coordinates with the logarithmic scale along the *x*-axis and liner *y*-axis.

It should be noted that the measured PSD data points transformed into the Rosin-Rammler coordinates do not follow the straight line in the range of sizes corresponding to the very fine particles: the PSD data curve for the particle diameters just below 1 μm departs from the fitted line – see Figure 2.3(a). This is caused by both the asymptotic behavior of the RR function constructed in the logarithmic coordinates and the fact that the measured PSD has a finite particle size value, for which the distribution intercepts the *x*-axis, i.e., $Q(x) = 0$. To obtain the best correlation between the measured and Rosin-Rammler distributions, the regression line shown in Figure 2.3(a) was built only for the particle sizes greater than 1 μm, which resulted in an R^2-value of 0.9912.

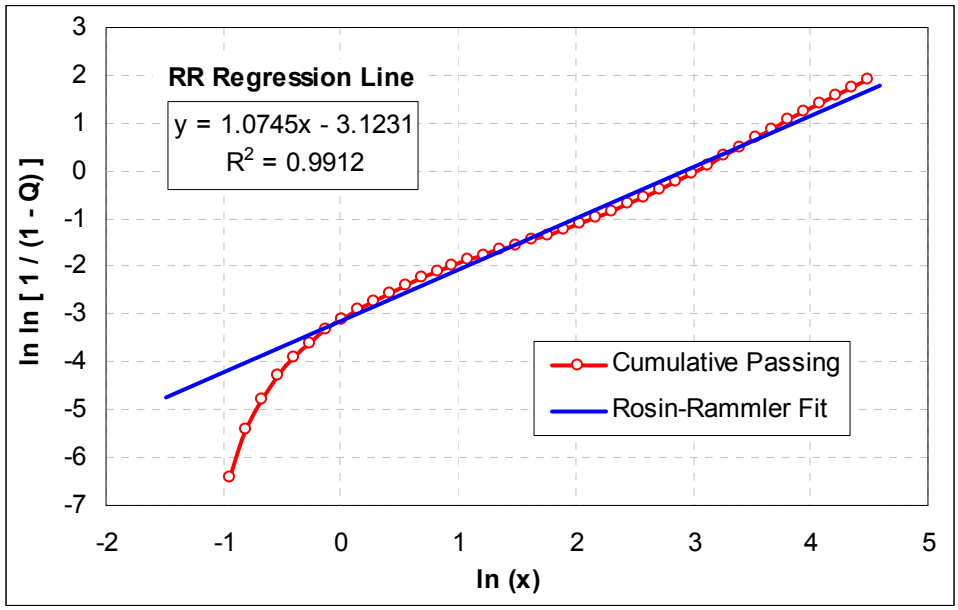

(a)

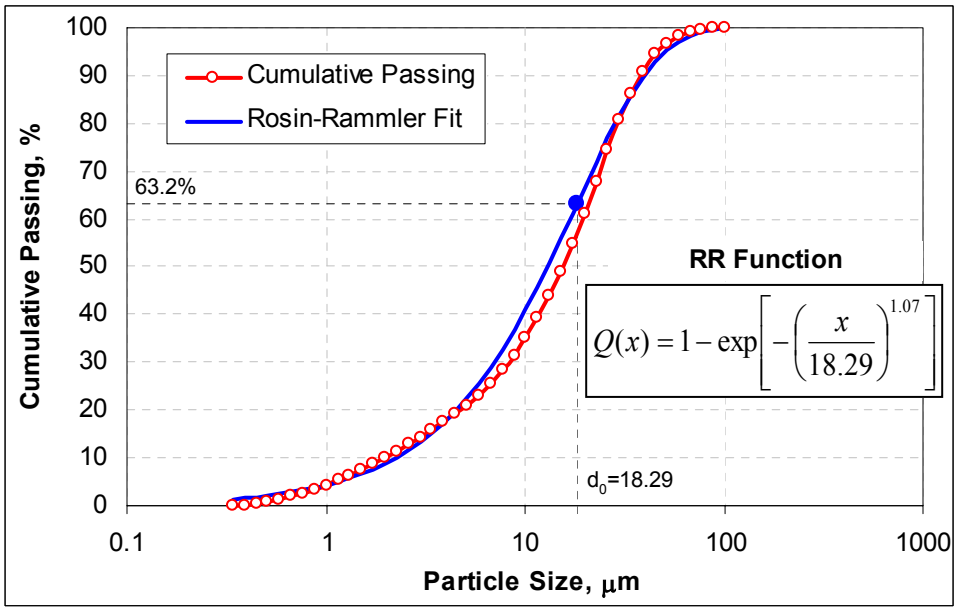

(b)

Figure 2.3. Rosin-Rammler Representation of Cement PSD
(a – RR Parameters Derivation from Regression Line; b – Fitted RR Curve).

As it was shown above, the RR size factor, d_0, represents a measure of the *fineness* of a powder. However, d_0 is mainly used only when the Rosin-Rammler

distribution is being applied to describe the PSD. The more conventional ways to estimate fineness of the cement is to determine:

- Specific surface area of the material, and
- Percent passing value through a target sieve.

These two methods allow for the characterization of cement fineness even if more complex PSD measuring equipment such as laser scattering analyzer is not available. They comprise the two most common fineness control procedures performed every 2-4 hours at most cement plants (Bhatty et al., 2004).

2.1.1.3. Specific Surface Area

Specific surface area is a cumulative measure of the fineness of a powder. In cement practice, it is expressed as square centimeters of total surface area per gram, or square meters of total area per kilogram of the material.

$$Specific\ Surface\ Area = \frac{S}{M}, \tag{2.13}$$

where,

S – Total surface area of all particles in the sample, m^2;

M – Total mass of the sample, kg.

There are two ASTM standardized methods to determine the specific surface area of portland cement:

- Wagner turbidimeter test (ASTM C 115), and
- Blaine air-permeability test (ASTM C 204).

The Wagner turbidimeter test is based on assessing the turbidity of the cement sample suspended in kerosene. The test apparatus consists of a fixed intensity light source and a photoelectric cell that detects the light rays passing through the suspension. The magnitude of a current generated in the cell is a measure of the turbidity of the suspension, which in turn is a measure of the surface area of the suspended particles (ASTM C 115).

The Blaine air-permeability test is based on assessing the airflow rate through a compacted bed of cement. The Blaine test apparatus consists primarily of a device to draw a certain amount of air though a bed of cement compacted to certain porosity. The number and size of pores in the prepared cement bed determines the airflow rate though the bed, which, in turn, defines the size of the cement particles (ASTM C 204).

The Blaine surface area measurement is known to work well for portland cements and is widely utilized in the industry (ASTM C 204). However, according to Bhatty et al. (2004), the method tends to suffer from poor reproducibility. Besides the apparent errors in setting up the device and performing the procedure, there is also a human factor induced by the daily shift changes at a cement plant that contributes to the inconsistent measurements. The authors report possible variations in the Blaine results obtained for two identical samples to be as high as 3.4% if the test is performed by the same person, and up to 6.0% if performed by two different laboratories. As a consequence, repetitive measurements of the Blaine value are always required, while adjustments to the milling process are recommended only if a significant change in the Blaine results is observed.

If the size distribution data of a sample is available, it can be used to estimate the specific surface area via an *exponential approximation method* (Kawatra, 2006). The calculation is based on the assumption that the individual particles of cement are spherical, which is in line with the laser scattering size analysis where the size of the particles is expressed through the diameters of the equivalent spheres (Frias et al., 1991).

According to Equation (2.13), the Blaine value can be calculated by adding the surface area of each individual particle and dividing the sum by the total mass of the sample. The same result will be achieved if the surface areas of individual particles are first added in a single size fraction between some x_{min} and x_{max}, and then added up across all size fractions. The size fraction here is represented by the interval between the points of the size grid generated by the laser scattering analyzer so that x_{min} and x_{max} are the lower and the upper boundaries of the fraction, correspondingly.

$$Blaine = \frac{s_1}{M} + \frac{s_2}{M} + \ldots + \frac{s_n}{M} = \frac{1}{M}\sum_{i=1}^{n} s_i \,, \tag{2.14}$$

where,

s_i – Surface area of particles in a single size fraction, i, of the sample;

M – Total mass of the sample;

n – Total number of size fractions in the sample;

s_1/M, s_2/M, etc. – Specific surface areas of the separate size fractions.

First, the specific surface area (Blaine value) of a separate size fraction should be calculated. For that, the mass of the material retained in the size fraction [x_{min}; x_{max}] should be known. Having the frequency function measured by the PSD analyzer and the total mass of the sample, it can be shown that:

$$m_i = f_i \cdot M \,, \tag{2.15}$$

where,

m_i – Mass of material in fraction i of the sample;

f_i – Portion of the sample (percent by mass), retained in fraction i.

Next, let the particle sizes within [x_{min}; x_{max}] increase linearly from x_{min} to x_{max} and divide that interval into infinitely small sub-fractions of equal widths dx, where each sub-fraction consists of particles of the same diameter and thus, same individual volume and mass, but has a different number of particles (see Figure 2.4).

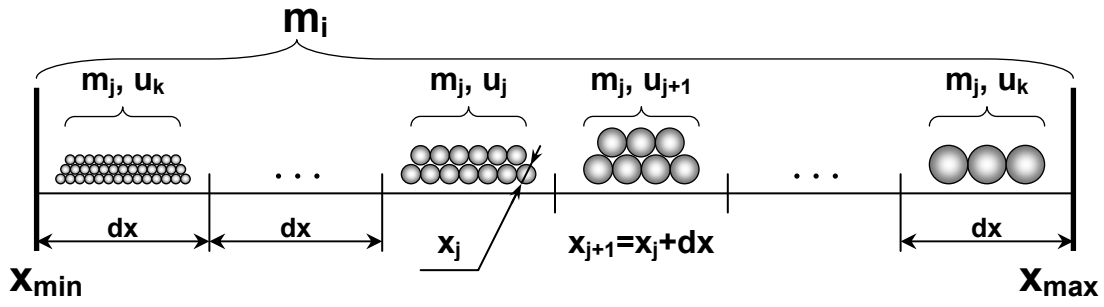

Figure 2.4. Blaine Calculation within the Particle Size Fraction.

The number of sub-fractions, k, within fraction i can then be found as:

$$k = \frac{x_{\max} - x_{\min}}{dx} \tag{2.16}$$

With the assumption that the mass of the whole fraction, m_i, is equally distributed among the sub-fractions, the mass of a single sub-fraction can be calculated as:

$$m_j = \frac{m_i}{k} = \frac{dx}{x_{\max} - x_{\min}} m_i , \tag{2.17}$$

where,

m_j – Mass of a single sub-fraction j comprised of equal-sized particles.

The quantity of the equal-sized particles within a sub-fraction j can be found by dividing the mass of the sub-fraction, m_j, by the mass of an individual spherical particle given by Equation (2.3):

$$u_j = \frac{m_j}{m} = \frac{6m_j}{\rho\pi x_j^3} , \tag{2.18}$$

where,

u_j – Number of particles within sub-fraction j;

m – Mass of an individual spherical particle;

ρ – Density of the cement particle;

x_j – Identical diameter of all particles in sub-fraction j.

Equation (2.1) shows the surface area calculation formula for a single spherical particle. Since all particles within the sub-fraction are of the same size x_j, the surface area of the sub-fraction is defined by the individual particle surface area times the number of particles within the sub-fraction. Using that along with Equations (2.1), (2.15), (2.17), and (2.18), the surface area of particles in the sub-fraction, s_j, is given by:

$$s_j = \frac{6f_i \cdot M}{\rho(x_{\max} - x_{\min})} \cdot \frac{dx}{x_j} \tag{2.19}$$

With $dx \to 0$, the specific surface area of fraction i can be calculated as:

$$Blaine_i = \frac{1}{M}\int_{x_{\min}}^{x_{\max}} s_j = \frac{6 f_i}{\rho\left(x_{\max} - x_{\min}\right)}\int_{x_{\min}}^{x_{\max}} \frac{dx}{x_j} = \frac{6 f_i}{\rho\left(x_{\max} - x_{\min}\right)} \ln\left(\frac{x_{\max}}{x_{\min}}\right), \tag{2.20}$$

where,

$Blaine_i$ – Specific surface area of fraction i.

Equation (2.20) determines the specific surface area of the individual fraction in the size interval of [x_{min}; x_{max}]. As per (2.14) by adding the Blaine values across all size fractions, the total specific surface area of the whole sample can be determined as:

$$Blaine = \sum_{i=1}^{n} \frac{6 f_i}{\rho\left(x_{i+1} - x_i\right)} \ln\left(\frac{x_{i+1}}{x_i}\right), \tag{2.21}$$

where,

x_i – Lower size boundary of fraction i;

x_{i+1} – Upper size boundary of fraction i.

The computation of the specific surface area of the material by means of the PSD data delivers a unique Blaine value result. It is not the case, however, if a reverse assessment of the PSD is attempted based on the measured Blaine value. The total specific surface area is an integral characteristic of the sample fineness, and a single number can not effectively represent the entire cement PSD. In fact, two cements with different ratios of fine and coarse particles and therefore described by different PSD's, can have the same Blaine value (Mizonov et al., 1997).

This ambiguity presents a significant obstacle for the adequate control of the cement quality if the fineness of the product is assessed solely by the Blaine measurement. As it will be shown later, the performance characteristics of cement depend not only on the surface area of the material, but also the proportion of the fine and coarse particles, i.e., the shape of the PSD of cement.

2.1.1.4. No. 325 Sieve Percent Passing

ASTM C 430 prescribes the test method for determination of hydraulic cement fineness by means of the 45-μm (No. 325) sieve. In principal, the described method resembles the conventional sieving technique discussed earlier with the exception that ASTM C 430 employs a wet sieving procedure.

One gram of the cement is first placed on a clean, dry 45-μm (No. 325) sieve and thoroughly wet with a gentle stream of water. Then, the spray nozzle is adjusted to produce a certain pressure, and the sieve containing the sample is washed with the jet of water in a circular motion for 1 minute. After this, the sieve and the residue are dried in an oven or over a hot plate. The residue is then brushed off of the sieve, weighed, and the corrected percent of the material passing the 45-μm (No. 325) sieve is reported as a result.

The amount of the material below 45-μm can also be estimated using the cumulative PSD of the cement sample (see Figure 2.2). However, this estimation may be slightly different from that of the ASTM C 430 test result due to the differences in the principles underlying the two measurement techniques.

2.1.2. ASTM Fineness Requirements

There are several ASTM standards concerning fineness of cement. The following list summarizes the test methods for measuring different aspects of the portland cement fineness: PSD, specific surface area, and percent passing through the standard sieves.

- ASTM C 115 – Fineness of portland cement by the turbidimeter:
  → Specific surface area and PSD;
- ASTM C 204 – Fineness of hydraulic cement by air-permeability apparatus:
  → Specific surface area: Blaine value;
- ASTM C 430 – Fineness of hydraulic cement by the 45-μm (No. 325) sieve:
  → No. 325 sieve % passing by mass;
- ASTM C 786 – Fineness of hydraulic cement and raw materials by the 300-μm (No. 50), 150-μm (No. 100), and 75-μm (No. 200) sieves by wet methods:
  → No. 50, 100, and 200 sieves % passing by mass.

The ASTM methods above merely describe the measuring procedures, i.e., they do not prescribe any particular fineness values as the targets. The only two ASTM specification type publications covering requirements for the cement fineness are:

- ASTM C 150 – Standard specification for portland cement;
- ASTM C 1157 – Standard performance specification for hydraulic cement.

ASTM C 150 describes eight types of portland cement and their uses. It lists test methods for cement characterization and specifies some of the chemical composition and physical properties requirements. The fineness requirements (see Table 2.3), however, are very scarce and prescribe only a single value of a minimum specific surface area for all 8 types of cement. ASTM C 150 does not provide any recommendation for the 45-μm (No. 325) sieve percent passing value.

Table 2.3. ASTM Specification Requirements for Cement Fineness.

Specification Publications	Test Methods		
	ASTM C 115 Turbidimeter	**ASTM C 204 Blaine**	**ASTM C 430 Sieve No. 325**
ASTM C 150 Portland Cement	**Yes*** min 160 m^2/kg	**Yes*** min 280 m^2/kg	**No**
ASTM C 1157 Performance of Hydraulic Cement	**No**	**Yes** No value	**Yes** No value

* Laboratory selects the test method. If the Blaine test requirement fails, the Turbidimeter test should be used.

ASTM C 1157 presents the performance requirements (strength range limits, time of setting, in some cases heat of hydration and sulfate resistance, etc.), but does not place any restrictions on the composition of the cement as well as its constituents to achieve these requirements. It prescribes that the manufacturer reports both the amount retained, when wet sieved on the 45-μm (No. 325) mesh, and the specific surface area (Blaine value) by the air permeability apparatus. However, it does not set any specific targets for the determined fineness characteristics (see Table 2.3).

It is safe to assert that the existing ASTM specifications do not provide sufficient information on the preferred fineness of the cement, and contain absolutely no guidelines for the desirable PSD characteristics along with the effect they have on the portland cement performance.

The notion that the early compressive strength of the cement-based materials is directly related to the cement particles surface area has already been introduced earlier. As a result, fineness of the produced cement is usually mutually established "in-situ" between the manufacturer and the customer (Neville, 1995).

As a matter of fact, not only the compressive strength, but the vast majority of the abovementioned cement performance characteristics depends upon the cement fineness, especially during the early stages of hydration. A better understanding of the cement behavior in response to its fineness should be achieved. The standards governing the cement specifications should be complemented to reflect that understanding and put it in practical use.

2.1.3. Fineness and Its Influence on Performance Properties of Cement

The influence of the portland cement fineness on such performance properties of the cement-based materials as strength, setting time, heat release, water demand, and many more, is known and has been reported by many authors. The literature review presented below covers the most prominent research efforts conducted by several authors in attempt to better understand the relationship between the fineness characteristics of cement – specific surface area and PSD – and the ultimate performance properties of cement-based materials.

2.1.3.1. Frigione and Marra (1976)

These authors studied the relationship between cement size distributions with identical specific surface area and compressive strength. First, they mathematically showed that at a given stage of reaction, the quantity of hydration products formed by the grains of the same diameter is always higher than the quantity formed by the cement

of an identical specific surface area, but with a wider PSD. This inference was made using the following assumptions:

- The cement particles are spherical;
- The hydration proceeds uniformly from the outside of the grain to the inside;
- The depth of the water penetration into the cement particles does not depend upon the particle size, although it is controlled by water diffusion through the gelatinous hydration as per Fick's second law.

An experimental investigation was carried out in order to verify findings of the mathematical simulation. For this, a Type I clinker produced in a dry-process rotary kiln was ground in a laboratory ball mill to the Blaine specific surface area of 320 m^2/kg. It was then subjected to a Walther dust trap to generate four narrowing particle size distributions. The PSD's were analyzed using Baho-Neu particle classifier, and the Rosin-Rammler spread factor, *n*, values were defined as: 1.15, 1.50, 2.14, and 3.31. The authors noted that cements having the same specific surface area but narrower range of the particle size distribution should require less grinding work.

The non-evaporable water test was performed to assess the amount of the hydrated product as a function of the RR spread factor, *n*, during various stages of hydration: after 1, 2, 3, 7, 14, and 28 days. It was shown that quantity of the hydrated product increased quickly to about $n = 2$, but then slowed down considerably and leveled out.

Calculation of the thickness of the hydrated layer revealed that it decreased as the PSD became narrower. The decrease was even more prominent at the later stages of the hydration. This result refuted the initial assumption about the depth of water penetration being independent of the particle size distribution.

The concrete samples were prepared at two water/cement ratios (0.42 and 0.82) and tested for an unconfined compressive strength. The influence of the RR factor *n* on the development of strength was shown to be sensible at $n < 2$ for the lower w/c ratio, while for the higher w/c, the parameter *n* appeared to have influence at the higher values as well.

The results of Frigione and Marra (1976) confirmed a significant influence of the PSD width on the strength development characteristics of the cement-based materials. Moreover, the results suggested that for a given water/cement ratio, there is a certain magnitude of RR size factor, *n*, after which both the rate of hydration and the compressive strength development tend to level out.

2.1.3.2. Skvara et al. (1981)

The authors studied the relationship between the PSD of a special type of high early strength cement and its strength development characteristics. The special cement used in the investigation was a gypsum free material prepared by grinding clinker with a lignin based aid and addition of alkali carbonate as a hydration retardant.

The same clinker was ground in a laboratory ball mill to different levels of specific surface area to produce cements having Blaine values ranging between 420 and 1000 m^2/kg. A cement sample with the Blaine value of 750 m^2/kg was processed in the Alpine Multiplex classifier in order to separate three size fractions: fine – below 5 μm, medium – between 5 and 25 μm, and coarse – between 25 and 50 μm. The fractions were then mixed in various proportions to achieve several PSD's. The size distributions were detected by Sedigraph via sedimentation analysis in a water-free environment.

The mortar samples were prepared at w/c = 0.33 for the strength analysis. It was confirmed that, as a general trend, the strength gain after one day of curing appeared to be a direct function of the specific surface area of the cement. However, some samples with lower Blaine values but different PSD make-up, exhibited higher one day strengths than those having higher specific surface areas. This phenomenon was attributed to the varying content of the fine cement fraction (below 5 μm), where cements having higher contents of the fine fraction attained higher strengths.

Thus, it was shown that producing cement with a certain specific surface area is not a sufficient condition for reaching high short-term strengths. The Blaine test method was presented only as an integral fineness measurement, which does not say much about the inner particle size composition of the material.

It was further observed, however, that the contents of the particle fraction smaller than 5 μm could not be increased above a certain level (reportedly, 85-95%). Curing of the cement paste samples containing 85% of the particles below 5 μm showed a decline in strength development after 7 days. The strength reduction was ascribed to the absence of the coarser particles (of cement or sand), which would otherwise add to the structural integrity of the paste. In case of mortars, the strength decrease was not observed.

The authors also engineered several cement samples with discontinuous PSD's by combining two or more narrow particle size fractions. The best cement sample prepared with 25% of particles below 5 μm and 75% between 25 and 50 μm exhibited a 78% increase of the 1-day strength and a 37% increase of the 28-day strength compared to the sample having a continuous PSD of the same Blaine value of 750 m^2/kg. A better workability of the engineered sample was noted too.

The research results presented by Skvara et al. (1981) showed that engineering of the cement PSD may lead to significantly improved strength characteristics of the cement-based materials. However, the alterations should be done in a competent way as adverse effects, such as uncontrollable setting and undesirable volume changes, are also possible.

2.1.3.3. Neville (1995)

Neville (1995) reviewed the common practice for production of rapid-hardening cements. He showed that the increased rate of strength gain is usually achieved by a higher alite content (C_3S higher than 55%, sometimes up to 70%) and by a finer grinding of the cement clinker. On average, high early strength cements (so called Type III as per ASTM C 150) have specific surface area of 450 to 600 m^2/kg, compared with 300 to 400 m^2/kg for the normal type of cement (Type I as per ASTM C 150).

The higher fineness (Blaine value) significantly increases the strength at 10 to 24 hours, with the increase persisting up to about 28 days. The author revealed that the strengths equalize at the age of about 2 to 3 months. Later on, the strengths of the cements with a lower Blaine value surpass that of the higher fineness cement.

The author warned however, that the cements with a *very* high fineness should be given a special consideration. The extremely high specific surface area of the cement

increases the water demand of the mix. As a result, for a given cement content and workability, the water/cement ratio would increase, which would offset the benefits of the higher fineness with respect to early strength. For these conditions, higher water content would produce lower strength of the paste.

It is also noted that the higher fineness of the cement will produce higher levels of heat of hydration. This may turn out to be beneficial for construction in colder climates, but may as well obstruct the use of rapid-hardening cements in mass or large scale structural projects.

The author continued with the introduction of an *ultra high* early strength cement, which was produced at the Blaine values of 700 to 900 m^2/kg. This kind of cement was generated by separating fines using a cyclone air elutriator. Such high fineness led to an extremely rapid hydration, early strength gain, and a high rate of heat release. For example, the 3-day strength was reached in 16 hours, and the 7-day strength in 24 hours.

The effect of fineness on the strength development in the cements produced from similar clinkers is shown in Figure 2.5.

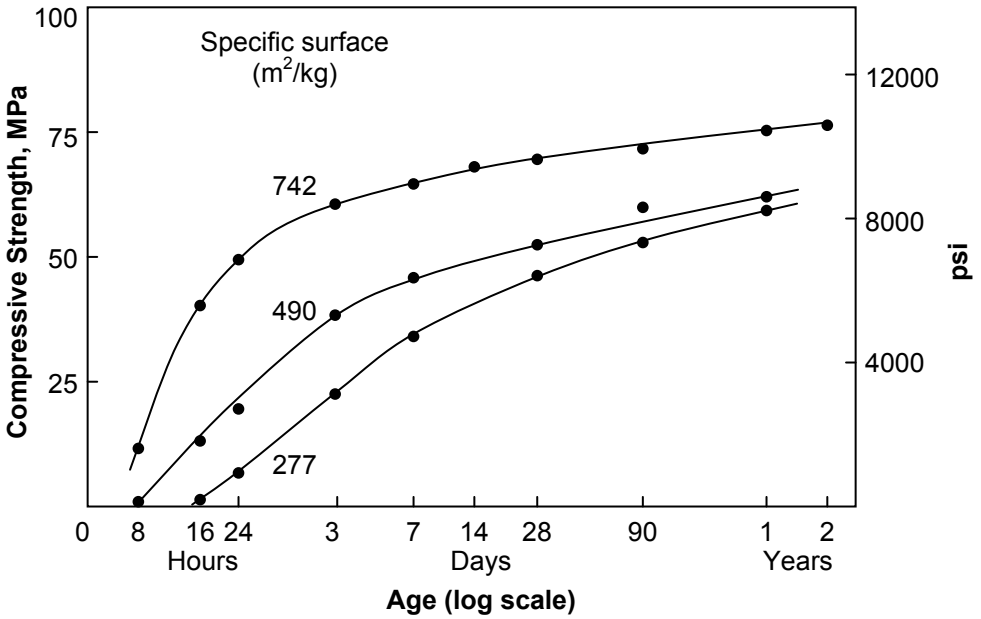

Figure 2.5. Effect of Blaine Fineness on Concrete Strength (after Neville, 1995).

Neville (1995) summarized rapid-hardening types of cements characterized by increasingly high levels of the specific surface area. The strength gain versus fineness relationship was clearly demonstrated. Yet, he referred only to a single aspect of the cement fineness, that is – the specific surface area or Blaine value. No consideration was made to the possible variations in the cement PSD along with its effect on the performance characteristics of cements.

2.1.3.4. Zhang and Napier-Munn (1995)

These authors proposed regression models that included the size distribution and the chemical composition as factors for predicting the strength of cement. In their work, they first established the relationship between the cement PSD and the specific surface value. The authors analyzed 144 sets of data that included measured PSD's and specific surface area values, and derived a linear regression model tying the observed Blaine test results with the surface area estimated from the PSD curves. The PSD estimates were based on the premise that all particles within a measured size fraction have an identical diameter.

Here, the utilized approach had an apparent lack of precision compared to the Blaine calculation method offered in section 2.1.1.3 of this dissertation, where the particle sizes were assumed to increase linearly from the lower boundary of the measured fraction to the upper one. Fortunately, the authors were able to overcome the unintended error by virtue of applying linear regression analysis. The derived regression coefficients simply incorporated the acquired error. The established correlation achieved an R^2-value of 0.942.

The authors conducted a vast experimental investigation, studying the two major factors influencing the strength development of the cement-based materials:

- Mineralogical composition of cement, and
- Fineness of cement expressed as both PSD and specific surface area.

Employing the known effect of the individual cement mineralogical phases on the strength development (see section 1.2.2), the following mineralogical characteristic factor of cement was proposed:

$$CMF = C_3S + C_2S + C_3A - C_4AF, \quad (2.22)$$

where,

CMF – Cement Mineralogy Factor;

C_3S, C_2S, C_3A, and C_4AF – Content of the mineralogical phases, percent.

The set of the CMF data was then subjected to linear regression analysis, and a correlation with the 28-day compressive strength data providing an R^2-value of 0.652 was obtained in the following form:

$$28D = X\,CMF - Y, \quad (2.23)$$

where,

$28D$ – Compressive strength after 28 days of cure, MPa or psi;

X, Y – Coefficients of the regression line.

The next step was to incorporate the cement PSD characteristics into the proposed regression model. Several trials included using parameters of the Rosin-Rammler distribution and percentages of material within a given size fraction. The best results achieved R^2-values between 0.814 and 0.835 and employed cumulative percent passing values through certain "sieve" sizes.

$$3D = X_3\,CMF + Y_3\,S8 - Z_3 \quad (2.24)$$

$$7D = X_7\,CMF + Y_7\,S8 - Z_7$$

$$28D = X_{28}\,CMF + Y_{28}\,S32 - Z_{28},$$

where,

$S8$ – Amount of the cement material below 8 μm;

$S32$ – Amount of the cement material below 32 μm;

X, Y, Z – Coefficients of the regression line;

$3D$, $7D$, $28D$ – Strengths after 3, 7, and 28 days, respectively, MPa or psi.

It was found that a better relationship could be attained if the early strength (after 3 and 7 days) was correlated with the fine fraction for sizes below 8 μm; whereas the 28-day strength was found to be strongly related to the size fraction below 32 μm.

A similar approach was applied to include the specific surface area in the regression analysis as an alternative to the size fractions. It was found that an increase in the Blaine value increased the strength at both early days (3 and 7 days) and later days (28 days). The regression lines identical to those defined in (2.24) were derived, with the exception that the values of cumulative percent passing were substituted for the specific surface area values in all three expressions. The R^2-values reached 0.798-0.833. A regression model tying the cement compressive strength results determined by the concrete mix and mortar test methods was also established in this study.

Zhang and Napier-Munn (1995) showed that different size fractions of the PSD account for cement strength development during different curing ages. The specific surface area appeared to impact the strength gain during the observed period of 28 days. The empirical correlations were proposed to describe the following relationships:

- Measured Blaine value and specific surface area estimated from the cement PSD;
- Strength gain and mineralogical composition along with the amount of cement particles in certain size fractions;
- Strength gain and mineralogical composition along with the specific surface area.

2.1.3.5. Navi and Pignat (1999)

These authors studied the effect of the cement PSD on the capillary pore structure of cement paste. They used a three-dimensional simulation to calculate the degree of hydration, the hydraulic radius, and the capillary pore distribution at various degrees of hydration. The proposed mathematical model was based on hydration of the major cement phase: alite (C_3S) prepared at a water-to-cement ratio of 0.4. The C_3S particles were considered spherical.

The authors evaluated four different cement size distributions: one real and three engineered. The real distribution spanned between 0.5 and 40 μm and had a Blaine surface value of 358 m^2/kg. The manufactured PSD's had a progressively increasing lower boundary of the size span, while the upper boundary stayed the same for all four cements. Thus, four gradually narrowing distributions were subjected to the study. The

three manufactured cements were characterized by declining Blaine specific surface area values of 198, 160, and 106 m^2/kg.

The simulation results showed that during early curing stages, the finer cement particles achieved higher degrees of hydration. For the same w/c ratio, the cements with the finer particles made more contact surfaces and had smaller hydraulic radius (defined as the ratio of the total pore volume – the capillary water and the void space – to the total free surfaces of all grains) than the cements with the coarser grains. The coarse cements also produced larger pores at any given curing stage. Navi and Pignat (1999) concluded that the evolution of the microstructure of hardened cement paste strongly depended on the cement particle size distribution.

2.1.3.6. Bentz et al. (1999)

This group of authors performed an extensive model-based investigation of the PSD effect on the performance characteristics of the cement materials. Namely, the authors picked for their study two cements with significantly different specific surface areas: 640 and 210 m^2/kg. The values of the Rosin-Rammler size factor, d_0, defining the average particle sizes of the two cements, were calculated at 5 and 30 μm, respectively.

It should be noted that the term "particle size distribution" was used throughout the paper as a distinguishing factor between the two cements. However, it would seem to be more appropriate to refer to the difference in their fineness levels only: the Blaine value or average particle size. The shapes of the two demonstrated PSD's appear to be very similar, as if produced by a parallel shift of one of the distributions. So the study really covered the effect of the average particle size (or specific surface area) on the performance characteristics of the cement and not the spread property of the PSD.

The majority of the investigations were conducted using a three-dimensional National Institute of Standard and Technology (NIST) microstructural model. Only a few experimental tests were carried out in order to back up the results derived from the simulation analysis. The authors examined the impact of fineness on such cement performance properties as: setting time, heat release, capillary porosity percolation,

diffusivity, chemical and autogenous shrinkage, internal humidity evolution, and interfacial zone microstructure.

The modeling was done for the two described cement samples, prepared at three water-to-cement ratios: 0.5, 0.3, and 0.246, and cured under simulated water-saturated conditions. The cements were derived from the same clinker, and the fraction of alite (C_3S) that had reacted at ages of 1, 2, 3, 4, 7, 14, 28, and 56 days was determined using quantitative X-ray diffraction in order to calibrate the NIST model.

All hydrations were executed for 5,000 cycles of the model, which corresponded to 25,000 hours (about 3 years) of real time at 20°C. The degree of C_3S hydration tests performed for the two cement samples at w/c = 0.5 using both model simulation and laboratory experiment showed an adequate correlation and provided additional data for model calibration. The finer cement exhibited an increased rate of hydration compared to the coarser cement at all curing ages.

The setting time analysis showed that even though the finer cement requires less time to achieve set due to the increased hydration rate, it also requires a higher degree of accomplished hydration, since more particle-to-particle bridges need to be built to form a network of pathways composed of C-S-H gel or ettringite (by definition of *setting* used in the model). The coarser cement requires more time to achieve set, and its strength development lags significantly behind that of the finer cement. The heat release analysis revealed that coarser cements result in a lower initial heat release rate, which can be useful when thermal cracking is of a concern.

The capillary porosity percolation study demonstrated that the coarser cements having a larger average interparticle spacing require more hydration for the capillary porosity to depercolate (to seal), implying a possibly enhanced curability.

Since the finer cement hydrates much faster for a given w/c, its relative diffusivity was seen to be much lower at early curing times (less than 300 hours). Eventually, for the lower w/c, hydration of the coarser cement catches up with that of the finer one, and the two relative diffusivities are nearly identical.

As cement hydrates, the volume occupied by the hydration products is less than that of the reactants. Therefore, unless water is supplied from an external source, this chemical shrinkage results in the formation of empty pores within the cement paste microstructure. Evaluation of the chemical shrinkage showed that under proper and carefully controlled curing conditions, lower porosity should be achieved in the systems with the coarser cements.

As for the internal relative humidity, its reduction was anticipated to be less for the coarser cements; however, they still may contain more water-filled pores. The coarser cements were also expected to produce less autogenous shrinkage.

The investigation of the interfacial zone microstructure showed that for the conventional water-to-cement ratios, the coarser cement results in a microstructure characterized by a higher porosity and larger pores. At low w/c (below 0.3), this effect becomes less significant.

In their work, Bentz et al. (1999) suggested that the development of the coarser cements may have certain benefits: energy savings due to reduction in grinding time while delivering long-term performance potentially equivalent to finer cements when prepared at a lower w/c. However, if adequate curing of the coarser cement can not be guaranteed, the finer cements are still preferable due to both their increased early hydration rate and earlier depercolation of the capillary porosity. The authors argued that while a single cement particle size distribution can not be ideally suitable for all purposes, the cement PSD can be optimized for each particular application.

2.1.3.7. Modifications of the Cement PSD

The foregoing summary of the literature indicated that, when speaking of fineness, the cement performance does not solely depend on the specific surface area of the material. The shape of the particle size distribution curve has a significant impact on the cement properties as well.

Development of comprehensive targets for the cement fineness characteristics including both full-range PSD and specific surface area is possible only by means of a thorough understanding of the principles underlying the relationship between the cement

fineness and its performance. The particular nature of the cement hydration reaction, upon which the cement fineness has a significant influence, is characterized by complex three-dimensional microstructural transformations and is still not fully established.

It is obvious, however, that a competent design of the fineness characteristics of the cement can produce sound performance benefits. Several authors cited above tried to modify these characteristics and their attempts included:

- Increasing the total specific surface area (Blaine value) of the cement;
- Decreasing the mean size of the cement PSD;
- Narrowing the cement PSD;
- Producing the discontinued (multimodal) PSD;
- Controlling portions of certain fractions of the cement PSD;
- Using coarser cements prepared at lower water/cement ratio.

The listed modifications are relatively easy to achieve in the laboratory. On the industrial scale, however, the task becomes non-trivial. In order to understand how grinding equipment generates a particular PSD of the cement, a thorough examination of the current state of the industrial finish milling has to be made.

2.2. CEMENT GRINDING TECHNOLOGY

There is a lot of technical literature available on the modern means of reducing rocks and minerals in size. This section describes the most common clinker grinding solutions applied in the cement industry.

2.2.1. Grinding

Clinker grinding fulfills two major tasks, which ultimately determine the choice of milling equipment. A cement mill should be able to:

- Create sufficient surface area for the cement hydration reaction to occur, and
- Reduce the particle sizes to ensure that all of them are consumed in the reaction.

There are several types of mills that can be employed to pulverize clinker and thus produce cement. The most common finish mills used in the cement industry are listed in Table 2.4 (Kawatra, 2006).

Table 2.4. Most Common Mills Employed in the Cement Industry.

Grinding Equipment	Grinding Force	Energy Use* (kWh/t cement)	Grinding Efficiency**
Tube Mill	Impact / Friction	35-38	5-8%
Roller Press	Compaction / Friction	22-26	12-20%
Vertical Roller Mill	Compaction / Friction	27-30	7-15%
Horizontal Roller Mill	Compaction / Friction	24-27	10-18%

* To produce Blaine surface area of 350 m^2/kg (Ruth et al., 2000)
** Breakage energy with respect to consumed electrical energy (Fuerstenau and Han, 2003)

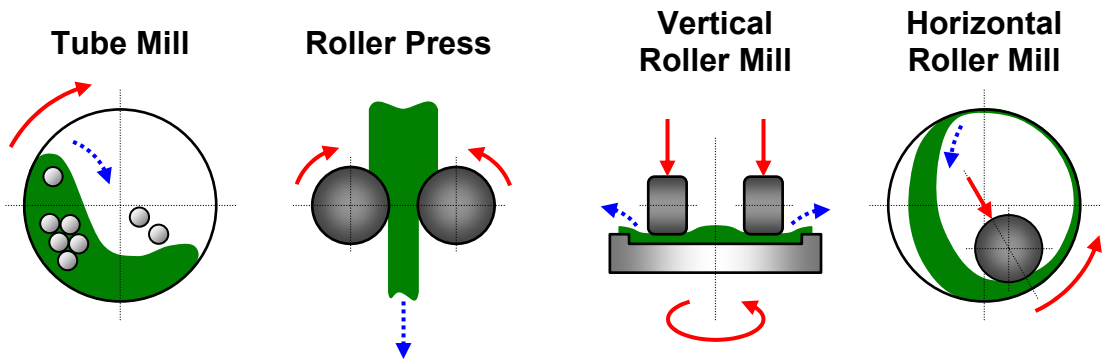

Figure 2.6. Schematics of the Most Common Cement Mills.

The schematics illustrating working principles of the mills listed above are shown in Figure 2.6. The solid green color in this figure represents the material subjected to pulverization; the dotted blue arrows indicate the path or trajectory of the material flow, whereas the solid red ones show the direction of the equipment movement or action.

The comminution forces acting upon the material may be divided into four groups:

- Impact forces
- Compression forces
- Inter-particle contact forces
- Friction-shear forces

A grinding process is usually characterized by application of a combination of the comminution forces. For example, a vertical roller mill combines compression and friction-shear forces, while a ball mill combines impact and friction forces.

Remarkably, the efficiency of most cement grinding methods is well under 20%, with some of the equipment dropping below 10% (see Table 2.4). The majority of the supplied electrical energy is released in the form of heat generated by the impact and friction of the grinding media (Wills, 1992; Fuerstenau and Han, 2003).

The roller press (see Figure 2.6) has been extensively used as a pregrinder as well as a stand-alone cement mill. It compresses the material in a gap between two counter-rotating grinding rolls. The output product is a compacted cake that contains fine and coarse particles with a large number of cracks and weak points that significantly reduce the energy requirement during the further stage of pulverization (Kawatra, 2006).

The vertical roller mill has been a popular choice for raw and coal grinding due to its high drying capacity, low energy consumption, and compactness. Relatively recently, with improved metallurgy for wear parts and modified roller configuration, this type of milling equipment was successfully introduced to finish grinding and reportedly reduced the system power consumption by 30% compared to the conventional tube ball mill (Alsop, 2001).

In a vertical roller mill, the comminution takes place in a gap between the rotating table and the grinding rolls. The clinker is loaded in the center of the table and is moved, because of the centrifugal forces and friction, towards the table's edge. On its way, it passes under three or more conical rollers installed at the outside rim of the table. The rollers are attached to hydraulic cylinders and provide compressive grinding force. The pulverized material leaves the table with an upward air stream that carries the particles to the separator usually incorporated into the casing of the mill above the rollers and the table. Taken by the air flow, the fine product escapes to the mill discharge, while the coarse particles are rejected by the separator and fall back to the center of the table for an additional cycle of grinding (Kawatra, 2006).

The horizontal roller mill consists of a rotating horizontal cylinder and a grinding roller that is hydraulically pressed against the inside surface of the cylinder. The clinker passes into the mill at one end and, because of the centrifugal effect caused by the rotating cylinder, is carried through as a uniformly distributed layer of material on the inner surface of the mill. The hydraulic pressure on the roller and the internal fittings can be adjusted in order to regulate the grinding effort. Kawatra (2006) reports the potential energy savings of 35% to 40%, when employing the horizontal roller mill instead of the usual tube mill.

The tube (ball) mill is the most widely installed grinding equipment in the cement industry (Bhatty et al., 2004; Kawatra, 2006; and others). It consists of a rotating cylinder filled with steel balls that tumble inside the mill applying impact and friction forces to the clinker particles. For better grinding efficiency, the tube mill may be operated with one, two, or three internal compartments separated by diaphragms that prevent the transfer of the balls between the compartments, while allowing the flow of the ground material through the mill.

Despite increasing popularity of the roller-based grinding equipment, the tube ball mill persists as the most common solution for clinker pulverization and represents one of the focal points of this dissertation. The field data used in this work was collected at a pilot cement plant that utilizes tube mills for their finish grinding.

2.2.1.1. Tube Mill Configuration

The typical industrial ball mills are shown in Figure 2.7 and the internal structure of a two-compartment mill is given in Figure 2.8. The hardware-based characteristics of a common tube ball mill include:

- Length-to-diameter ratio
- Mill internal dimensions: useful length and internal diameter
- Discharge point of material
- Number of compartments
- Protective liner profile in each compartment
- Diaphragm design

- Filling degree with grinding media and material
- Grinding media size characteristics
- Mill rotational speed

Figure 2.7. Tube Ball Mills Used for Cement Finish Grinding.

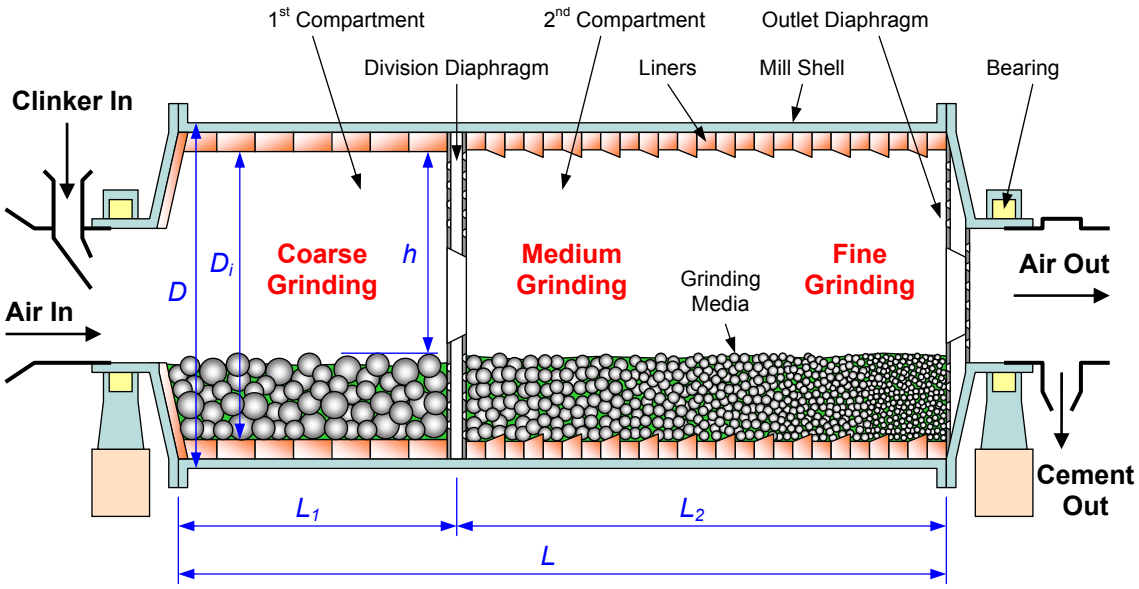

Figure 2.8. Arrangement of a Two-Compartment Tube Ball Mill (after http://en.wikipedia.org/wiki/cement_mill).

The geometric characteristics of the tube mill have great impact on grinding performance. On one hand, the hourly throughput depends on the mill diameter: the larger the opening, the more material can pass through. On the other hand, the fineness of the mill product depends largely on the time the material remains inside the mill (also called retention time). The mill length is the main factor that influences the retention time. Because of all this, the length-to-diameter (L/D) ratio is an important factor for an optimum design of the tube mill (Kawatra, 2006). Depending on a particular application of the mill either in an open circuit, or closed one, or circuits with pregrinding units, etc., the mill L/D ratio may vary between 2.8 and 6.0 (Kelly and Spottiswood, 1982).

The tube ball mills differ in a way the material leaves the mill. The ground clinker may be discharged at the end (see Figure 2.8) or in the middle of the mill body. It also can be either dropped mechanically out of the mill (Figure 2.8) or carried out by an airflow stream (pneumatic discharge).

Because the clinker particles should be reduced in size by a factor of between 1,000 and 10,000, it proves to be more efficient to apply different grinding forces to different size ranges of the material (Bhatty et al., 2004). This is done by utilizing several grinding compartments within the mill body. For example, in case of the two-compartment mill shown in Figure 2.8, the first compartment is designed to perform breakage of the clinker particles by impact forces alone, whereas in the second compartment, grinding is done mostly by friction-shear forces. To facilitate this, the compartment lengths, the division diaphragm, the liners along the compartment walls, and the size characteristics of the ball charge are designed accordingly.

The mill shell is protected by wear-resistant liners, which also provide lift to the ball charge. The first compartment is usually equipped with the liners that provide a cataract trajectory of the balls movement (see Figure 2.9). This guarantees the impact (crushing) nature of the interaction between the clinker particles and the steel balls. The three common types of the first compartment liners are shown in Figure 2.10(a) and include step, activator, and double wave liners.

The second compartment performs fine grinding of the material, which requires a cascade type of motion of the steel balls. This subjects the partially ground clinker particles to the friction-shear forces. The liners commonly installed in the second compartment are shown in Figure 2.10(b). They are primarily used to generate the classification of the ball sizes, bouncing the bigger balls towards the division diaphragm and the smaller ones – to the outlet of the mill.

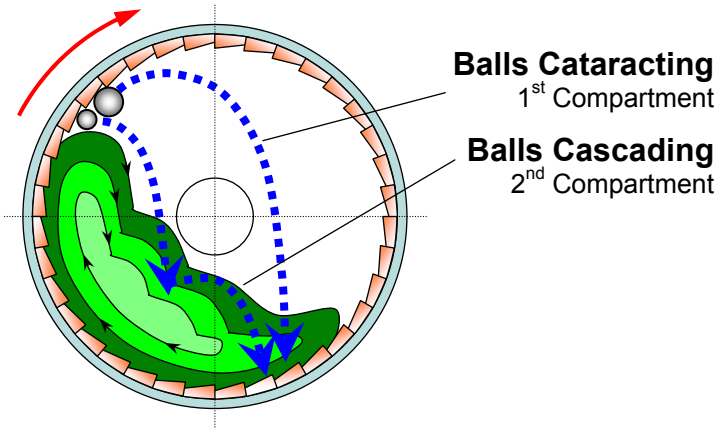

Figure 2.9. Internal Dynamics of the Grinding Media.

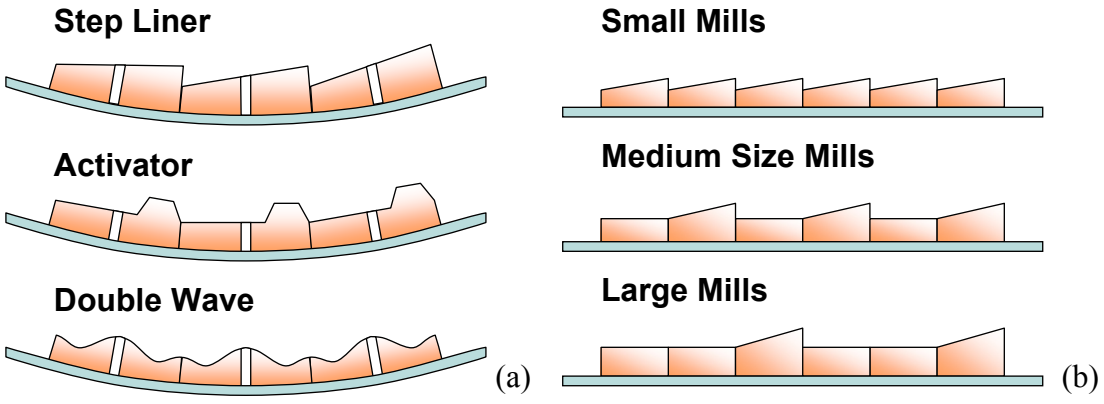

Figure 2.10. Liner Design of the Tube Ball Mill
(a – Lifting Liners in First Compartment; b – Classifying Liners in Second Compartment).

The diaphragm divides the tube mill into compartments. Typically, it has a double plate design with the perforated slots comprising approximately 5-10% of the total area of the diaphragm to allow the flow of the material. The slots usually have conical shape with wider openings on the side of the compartment receiving the material (see Figure 2.8). Some diaphragm designs permit adjusting the material flow from one compartment to another, which allows regulation of the material retention time in each compartment. Because of the direct influence on the retention time, the diaphragm design eventually influences the fineness of the mill product (Kawatra, 2006).

Filling degree is defined as the volume of the grinding media charge expressed as a percentage of the total useful mill volume. It can be determined by measuring the free height above the grinding charge in static (see Figure 2.8). For a given length of the compartment, an elegant geometrical solution for a ratio of the circle segment area to the full circle area provides a formula for determining the grinding media filling degree:

$$Filling\ Degree = \frac{\alpha - \sin\alpha}{2\pi}, \tag{2.25}$$

where,

$\alpha = 2 \cdot \arccos\left(\frac{2h}{D_i} - 1\right)$ – Central angle of the segment in radians,

h – Free height between the mill ceiling apex and the level of balls,

D_i – Internal diameter of the mill compartment.

Studies have proven that there is a maximum grinding efficiency at a filling degree of 26% to 28%. A higher filling degree results in a lower grinding efficiency. Nevertheless, in some countries with low electrical energy cost and high market demand, filling degrees of 40% to 45% are used to maximize mill production (Fuerstenau and Han, 2003). A special consideration for the nominal strength of the mill shell should be made if higher than normal filling degrees are employed. The filling degrees in different compartments may vary to achieve the best performance.

There are certain guidelines for the level of clinker in each compartment as well. It is suggested that in the first compartment, the material covers half the size of the balls

in the top layer, when inspected in static conditions. In the second compartment, the material should almost fully cover the grinding balls. Too much material in either compartment will cause a decrease in the grinding efficiency, whereas too little material will cause an excessive ball wear and heat built-up (Kelly and Spottiswood, 1982).

Grinding balls are used in the tube mill in various sizes ranging from 10 to 100 mm. The various sizes are employed to adjust the density of the charge and to regulate the material flow through the mill as well as to deal with varying hardness of the ground material (Bhatty et al., 2004). The first compartment is usually loaded with mixture of steel balls ranging from 50 mm to 90 mm. Clinker passing into the second compartment is typically less than 2-3 mm, so the second compartment balls range from 15 to 50 mm. The ball charge distribution by size and weight should be carefully designed to achieve the best grinding efficiency (Alsop, 2001). Wear-resistant high-chrome alloys are now most commonly used for the balls and liners. Due to inevitable wear, the grinding balls require regular inspection and replenishment.

The mill rotational speed is one of the important design criteria of the tube ball mill. Many authors report the operational speed of the mill at about 75% of its critical speed (Alsop, 2001; Fuerstenau and Han, 2003; Bhatty et al., 2004; others). By definition, the critical speed is the slowest speed at which all particles on the mill liner start centrifuging, i.e., the speed necessary to prevent the particles from collapsing away from the mill shell. No grinding work is done at critical speed and above.

The critical speed formula is derived from the mechanics of angular movement for the case, when the centrifugal force acting upon the particle balances out the gravity force at the apex of the circular trajectory:

$$n_c = \frac{30}{\pi}\sqrt{\frac{2g}{D_i}} = \frac{42.3}{\sqrt{D_i}}, \tag{2.26}$$

where,

n_c – Critical speed, rpm

D_i – Internal diameter, m

g – Acceleration of gravity (9.8 m/c^2).

The common speed of the ball mill then is defined by:

$$n = 0.75 \cdot n_c , \tag{2.27}$$

where,

n – Turning speed (frequency) of the mill, rpm.

All hardware-based characteristics are important criteria for physical design of the ball mill and largely influence the fineness of the ground product. However, the mill can not be viewed as a free-standing piece of equipment. It never works alone and needs a feeding system, fans, cyclones, etc. The process parameters such as the feed rate to the mill, the air flow through the mill, and others, characterize operation of the mill in conjunction with the auxiliary equipment, i.e., within a circuit. The process parameters have an immediate effect on grinding efficiency of the mill with respect to both quality of the output product and process power consumption. The operation of the tube ball mill in a circuit will be discussed in greater detail later.

2.2.1.2. Longitudinal Sieve Analysis of the Tube Mill

As it has been emphasized on several occasions, the function of the cement mill is to reduce clinker particles in size. Consequently, the larger clinker particles are supplied to the mill inlet and much finer particles are collected at its exit. The difference in the size distribution of the material at the front and the end of the mill becomes a salient characteristic of the milling process.

Moreover, during periodical mill audits, the entire length of the mill is sampled at a certain interval (e.g., one meter) to perform a longitudinal PSD analysis. The samples from the second compartment are usually also subjected to the Blaine value test.

This procedure allows assessment of the grinding process throughout the full length of the tube and reveals whether the material undergoes a decrease in the mean particle size gradually, or not. By analyzing the sieve residual data close to the division and outlet diaphragms, it is also possible to see if the compartments over-grind or under-grind the clinker material.

2.2.2. Classification

Classification is a distinct process employed in grinding systems that allows separating ground material into several products differing in properties. It is performed by so called separators, or classifiers.

The separator's function in a cement grinding system, its common designs, and the techniques to evaluate its performance are provided below. The in-situ application of the separators in the finish milling circuits will be described later.

In the cement industry, the classification of the ground material is based on the size of the particles. The objective of the process is to separate the larger particles from the smaller ones so that the larger particles can be further ground to achieve required fineness without over-grinding the finer particles.

In order to divide material into the desired size fractions, a separating force of some sort should be applied (see Figure 2.11). A screen (sieve) is the simplest form of the size separator and can be employed to do the job. However, it is not well suited for handling the large quantities of the continuous material flow typical for the cement industry. The most common means of achieving continuous classification is an air separator, in which particles are suspended and dispersed in air while being divided into fractions (Bhatty et al., 2004).

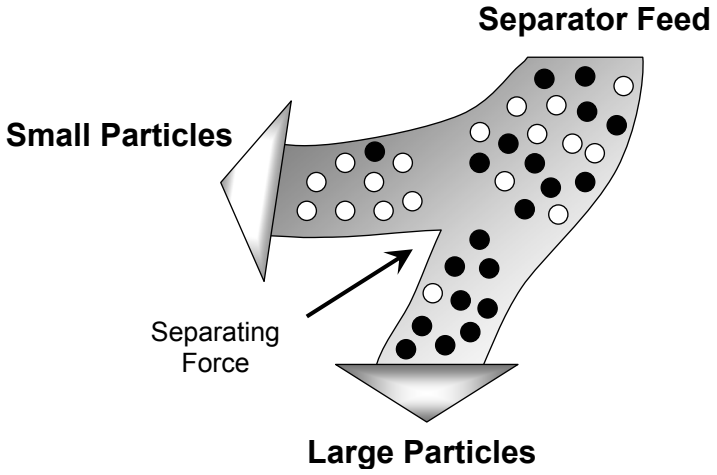

Figure 2.11. Action of the Separating Force (after Drzymala, 2003).

The physical forces that can be employed in the process of air classification include (Fuerstenau and Han, 2003):

- Gravity force
- Aerodynamic drag
- Centrifugal force
- Collision force

The movement of a particle in the separation zone, where alternative physical forces act upon the particle, is the basis for the air classification. Different forces depend on the size of the particle in different ways. The separators never use only a single classifying force, but rather employ a combination of forces, which allows them to create a bias towards the particles of a certain size and thus, to achieve classification.

In general, the separators can be divided into two groups: static and dynamic. The dynamic separators have a moving part, whereas the static units do not. The most common separators utilized in the cement industry are listed in Table 2.5.

Table 2.5. Most Common Air Separators Employed in the Cement Industry.

Classifying Equipment	Type	Classifying Forces
Cyclone	Static	Drag / Gravity
Static Separator	Static	Drag / Gravity / Centrifugal
V-Separator	Static	Drag / Gravity / Collision
Rotor Separator	Dynamic	Drag / Gravity / Centrifugal / Collision

Regardless of the type of separator being used, classification comprises several main steps. First, the feed material is transported to the separation zone either via a feeder chute (air-slide) or by means of a carrier gas. Because the separation takes place when the material particles are in a suspended state, the air is transported to the separation zone as well, either by internal or external fan. Then, the classification in the separation zone occurs as a consequence of the acting forces listed above. Finally, the

separated fractions should be removed from the separator. The fine particles usually leave with the air flow, whereas the coarse particles are transported mostly by gravity.

It is important to recognize that air classification does not create any new surface area of the material, i.e., it does not perform additional grinding. It only divides the existing material stream into two fractions: low and high in surface area.

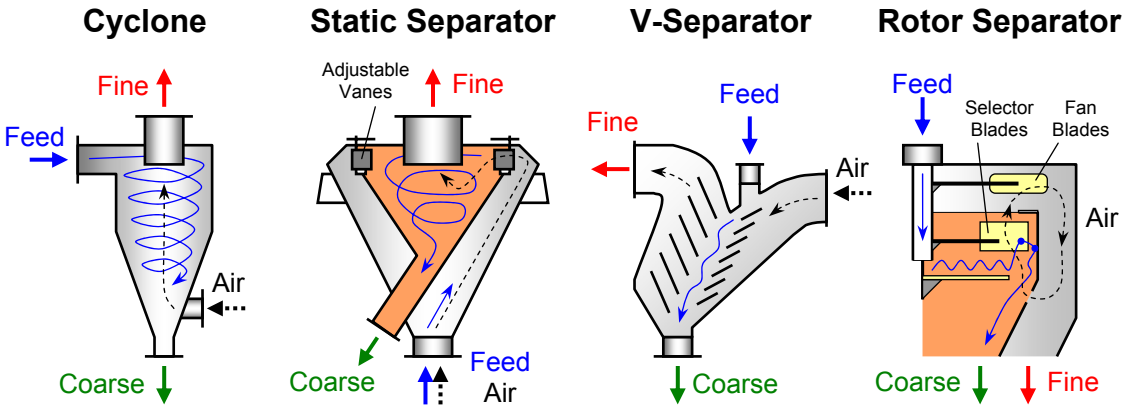

Figure 2.12. Schematics of the Most Common Air Separators.

The most basic type of the separator is a cyclone (see Figure 2.12). The material is fed into a conical cylinder, where an uprising stream of gas (air) is maintained. Two forces act upon the particles in opposite directions: aerodynamic drag (upward) and gravity (downward). As the particle size gets smaller, the gravity force, being proportional to the particle mass (i.e., cube of the mean diameter), will decrease faster than the drag force, which is proportional to the cross-sectional area of the particle (i.e., square of the mean diameter). If the particle is small (and light) enough, it will be carried away with the air stream as a final product, whereas the coarser (and therefore, heavier) particles will fall down.

Theoretically, if the acting forces balance each other out, the particle will be indefinitely suspended inside the cyclone. The particle size, for which the balance between gravity and drag forces is achieved, is called *cut size*. The particles of this size have an equal chance of becoming a fine product and being rejected as the coarse

particles. The geometrical characteristics of the cylinder and the speed of the air flow determine the fineness of the final product and are designed for a certain cut size.

The cyclone is the simplest separator and does not provide sufficient means for controlling the product fineness: only air flow rate alterations are available for that. The static separator has an improved design and employs adjustable guide vanes for controlling fineness (see Figure 2.12).

The feed material is carried into the static separator by the air stream via a vertical duct. The stream then enters the inner cone through a series of adjustable vanes that impart a swirling motion to the particles. Depending on the angle of the vanes, a greater or lesser centrifugal force is induced, causing a certain range of particles to fall by gravity into the inner cone. The remaining fine particles are swept out of the unit through a central tube and become the final product (Bhatty et al., 2004).

The cut size of the static separator is controlled by the angle of the guide vanes and the air velocity. If the angle of the adjustable vanes is increased from radial (in the range of 0-60 degrees), the induced tangential velocities increase, and more particles end up falling down into the inner cone, i.e., the final product carried out by the air stream becomes finer. This also increases the pressure drop across the static separator. The adjustment of vanes is normally done manually during the separator audit period. The vane positions stay fixed during the operation. Lengthening the central tube will provide a finer final product (Bhatty et al., 2004).

The V-separator (see Figure 2.12) was developed specifically for operation with the roller presses (Bhatty et al., 2004). The feed is introduced to the V-separator near the top and drops down through a series of inclined plates. The air is forced into the separator and sweeps the fines from the cascading material. The separation zone is the area between the plates and the series of baffles. Here, the finer particles are carried away by the aerodynamic drag of the air stream and the coarser ones are thrown by gravity off the baffles to the reject stream.

The fineness control of the V-separator is performed only by means of the air velocity. This type of separators can provide only a crude material classification and is normally followed by an additional separator.

The rotor type separators have recently become a standard for the new plant installations (Fuerstenau and Han, 2003). The latest developments of the rotor separators employ all four classifying forces. This allows for a very refined tuning of the interaction between the forces, which guarantees a lower possible cut size (finer product) and an enhanced overall efficiency of the classification process. The gravity and aerodynamic forces act in the dynamic separators as before, whereas the centrifugal force is generated by the spinning rotor, which also causes collision with the coarser particles. One of the main advantages of the rotor classifiers is that the separating action can be controlled during the operation.

The rotor separators went through several stages of development. The very first ones that became conventional in the cement industry involved a fan and a selector rotor attached to the same shaft on top of each other (see Figure 2.12). In these separators, the fan blades create an internal uplifting swirl of air that raises and carries the small particles away, while the larger particles are thrown against the inner wall by the centrifugal action of the selector blades sitting below the fan.

The main drawback of this particular separator is the difficulty to regulate the centrifugal action of the selector blades independently of the air flow generated by the fan, since they are attached to the same shaft. Several modifications of this arrangement have been adapted including moving the fan downstream from the area, where the classification takes place.

2.2.2.1. High Efficiency Separator Configuration and Operation

Today, the state of the art in rotor classifiers is represented by a High Efficiency Separator (HES). The HES is installed at the pilot plant, where the field data for this work was collected, and will be the main focus of the discussion from now on.

The HES is normally equipped with a cylindrical cage rotor that is powered by an independent drive and has many radial blades spaced evenly around the rotor's edge

(see Figure 2.13). Surrounding the rotor, there are stationary guide vanes angled to produce a swirl of air around the rotor. The separating zone is located between the rotor blades and the guide vanes.

The air intake is provided by an external fan (see Figure 2.13). The air enters the separator housing through one or more inlets and is spun by the guide vanes in the same direction as the revolving rotor. A uniform distribution of the incoming air is assured by the careful design of the air inlets and guide vanes. The rotor amplifies the air velocity, since the peripheral speed of the rotor cage is much higher than the tangential velocity of the air leaving the guide vanes. The air travels through the separating zone, picks up the fines, and exits from the center of the rotor. The exit duct takes out the air and the fines either at the top or the bottom of the separator, depending on the design.

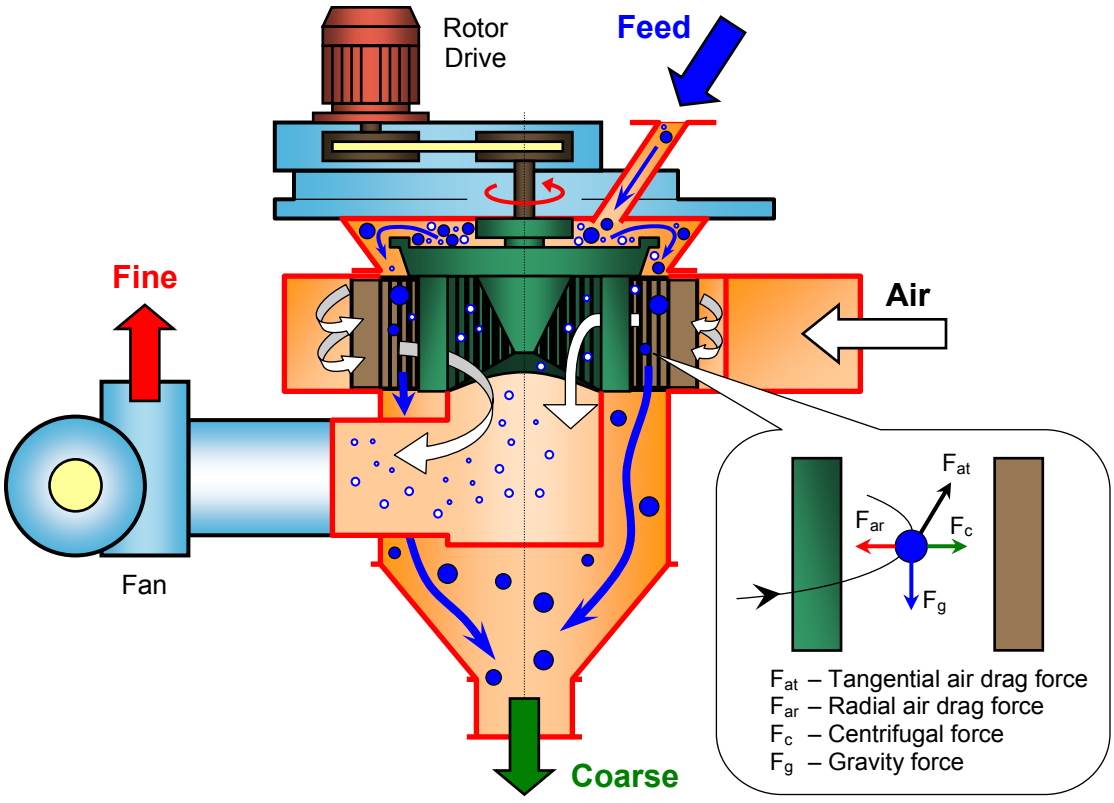

Figure 2.13. Internal Arrangement of the High Efficiency Separator.

The material flow inside the HES is illustrated in Figure 2.13 and follows several steps. First, the separator feed is directed onto a rotating dispersion plate, located on top of the cage rotor. As it falls down, the material starts a spiral movement caused by the initial spin of the rotor's dispersion plate and the high velocity swirl of the air leaving the guide vanes. The material is then evenly distributed by the centrifugal force into the annular gap between the rotor and the guide vanes and forms a thin cylindrical curtain in the classifying zone.

Here, the individual particles are subjected to four forces:

1. The air carries the material around at about the rotational speed of the rotor;
2. The radial air drag force is trying to pull the material inside the rotor;
3. The centrifugal force is trying to push the material towards the guide vanes;
4. The gravity force is pulling the material down.

Since the material in the classifying zone is always at about the same radius of rotation, the centrifugal force remains constant in all areas. Also, since the air and material are distributed evenly throughout the classifying zone, the radial air velocity and drag force are fairly constant in all parts of the zone. Because of all this, the cut size conditions (or, the force balance conditions) are uniform around the rotor, no matter where the particle is within the classifying zone (Bhatty et al., 2004). This significantly increases the efficiency of the classification process.

The fine particles are carried by the air flow into the center of the rotor and exit with the air exhaust. The coarse particles are pushed towards the guide vanes and continuously rinsed with the fresh incoming air. This helps to strip off any fine material that has agglomerated to the coarse particles and drastically improves the recovery of fines (Bhatty et al., 2004). Continuing the induced spiral movement, the coarser particles eventually reach the bottom of the classifying zone, fall down, and are discharged from the bottom of the vessel. The course particles form a *reject* flow (also called returns, regrinds, or tailings) and are normally intended for further grinding in the mill.

Leaving the separator, the finer material is still suspended and should be recovered from the air stream. A settling chamber, a cyclone, a filter (bag) house, or a combination of those can perform the recovery action (Bhatty et al., 2004).

Since the rotor is powered by an individual drive and the air flow is created by an external fan, the HES allows an independent adjustment of the centrifugal force, responsible for throwing the coarse particles away, and the aerodynamic drag force, carrying the fine particles inside the rotor. Moreover, the direction of the aerodynamic drag force is no longer aligned with the gravity force. In fact, both drag and centrifugal forces act in the plane perpendicular to the direction of the gravity force (see Figure 2.13). Therefore, both separating forces acting upon both size fractions can be controlled independently, as opposed to using the gravity force that was previously employed to sort out the coarse particles and can not be quite controlled. This explains how the principle employed in the HES is benefiting the overall improved efficiency of the separators of this type.

After seeing how the HES works, let's review the adjustments that can be made in order to influence the fineness of the product. These two parameters can be changed:

- The rotor speed, and
- The air flow

If the rotor speed is increased, the centrifugal force is increased too. Only very fine particles will be carried inside the rotor by the air stream. The fineness of the final product will be increased. If the air flow is increased, the aerodynamic drag force is increased as well. The air stream will be able to carry larger particles through the separation zone than before, and the fineness of the final product will decrease. The rotor speed and the air flow impact the fineness in opposite ways, since the centrifugal and drag forces act in the opposite directions as well.

Although the above statements are true in general, from cement plant experience it is known that the two parameters have some bias towards different aspects of the fineness characterization: namely, the Blaine surface area value and the percent material retained on No. 325 sieve. If the deviation from the fineness target is not significant, but

the separator adjustment is still desired, it is advised to change the rotor speed in response to the Blaine value change, and the air flow – in response to the value of No. 325 sieve percent retained.

This too can be explained by looking at the nature of the separating forces. The rotor speed affects the centrifugal force, which is responsible for sorting out the coarser particles and proportional to the cube of the particle diameter. Increasing the rotor speed has a substantial impact on the larger particles ($\sim x^3$), so that only ultra fine particles with high surface area (Blaine value) will end up in the final product. On the other hand, the air flow defines the drag force, which is responsible for carrying the finer particles inside the rotor cage and proportional to the square of the particle diameter. Increasing the air flow rate does not affect the large particles as greatly ($\sim x^2$), so that the collected surface area may not be impacted much, although the influence will be sufficient to be seen through the increased percent of the material retained on No. 325 (45 μm) sieve, i.e., the final product becomes coarser.

Despite the enhanced recovery of fines in the HES, some of the fine material is still rejected with the larger material due to particle interaction and agglomeration, which is typical for the fine grinding. These effects reduce the effectiveness of the size separation and account for so called *bypass* of the material – one of the characteristics of the separator.

2.2.2.2. Tromp Curve Characteristics of the HES

The three material streams surrounding the separator are (see Figure 2.14):

1. Separator feed,
2. Rejected coarse material, and
3. Carried through fine material.

The classifier splits up the feed material into two separate streams: rejects and fines. All three material streams are characterized by their individual mass flow rate, B, and particle size distribution, $f(x)$. The typical PSD data describing the three material streams surrounding the HES are shown in Figure 2.15.

In order to evaluate efficiency of the separation process, the Tromp curve of the separator is calculated and widely used throughout the cement industry (Bhatty et al., 2004). The Tromp curve shows percent of the material in each individual size fraction that is recovered into the coarse stream. The opposite of the Tromp curve is the grade efficiency curve (GEC), which defines percent of the material in each fraction recovered into the fine stream (Mizonov et al., 1997).

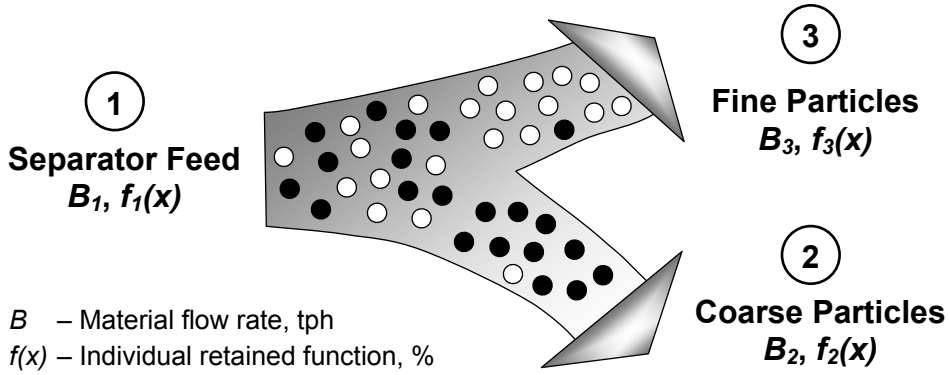

Figure 2.14. Material Streams Surrounding Separator.

The Tromp curve can be derived from the basic principle of mass balance: the amount of material supplied to the separator is equal to the amount of material leaving it. In a steady-state operation, the mass flow of the fresh feed is equal to the sum of mass flows of fine and coarse streams:

$$B_1 = B_2 + B_3, \tag{2.28}$$

where,

B_1 – Mass flow of the feed stream, mass per time unit;

B_2 – Mass flow of the coarse stream, mass per time unit;

B_3 – Mass flow of the fine stream, mass per time unit.

For the same time period, B_1, B_2, and B_3 are identical to the mass values.

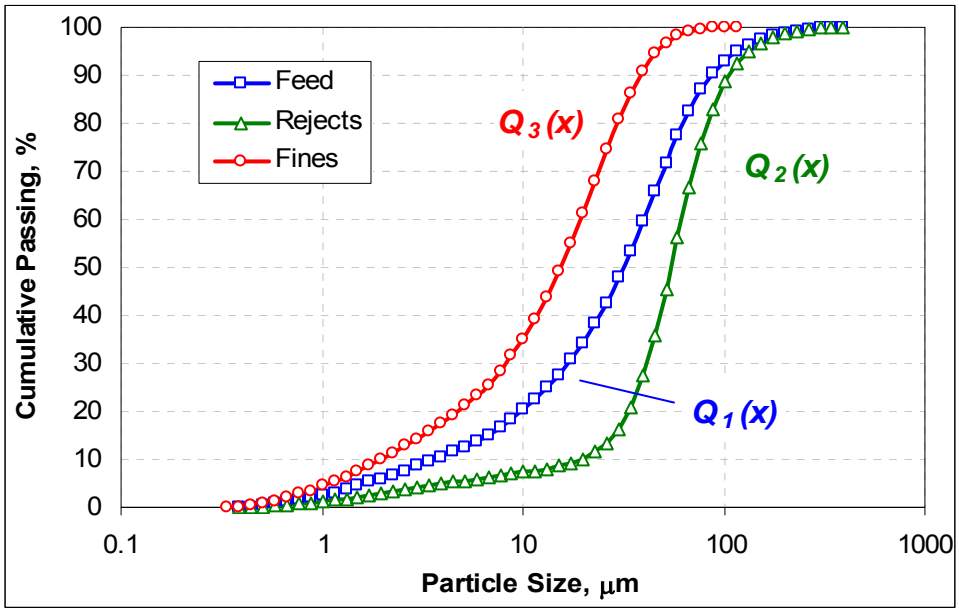

(a)

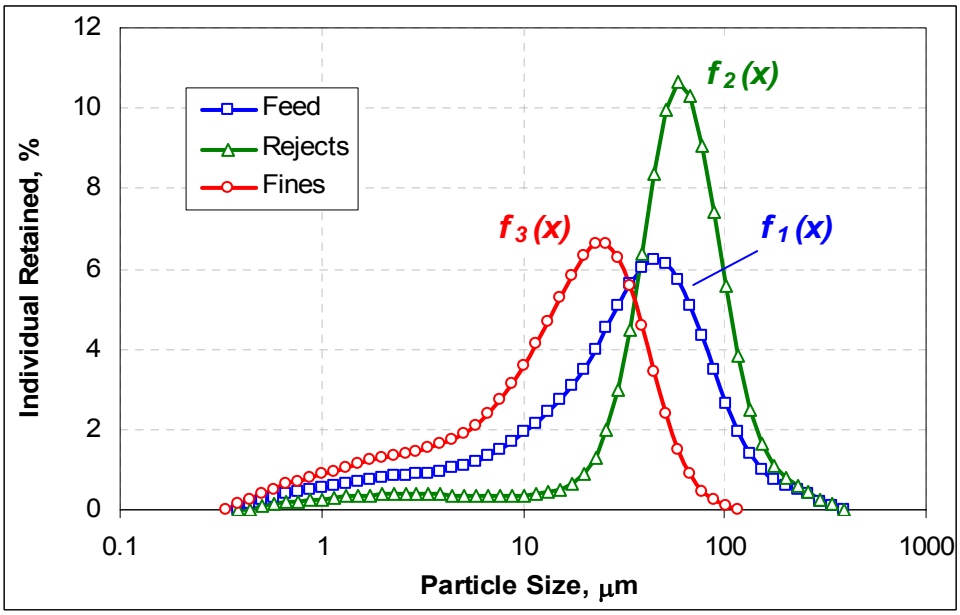

(b)

Figure 2.15. PSD of the Material Streams Surrounding Separator
(a – Cumulative Passing PSD; b – Individual Retained PSD).

As long as no comminution takes place in the separator, the amounts of material within a single size fraction entering and leaving the separator are equal:

$$B_1 \cdot f_{1i} = B_2 \cdot f_{2i} + B_3 \cdot f_{3i}, \tag{2.29}$$

where,

f_{1i} – Portion of the material in the *i*-th fraction of the feed stream;

f_{2i} – Portion of the material in the *i*-th fraction of the coarse stream;

f_{3i} – Portion of the material in the *i*-th fraction of the fine stream.

The Tromp value for the *i*-th fraction is defined by the probability of the feed particles to occur in the coarse stream and equals the ratio of the coarse fraction mass to the feed fraction mass (Bhatty et al., 2004):

$$Tromp_i = \frac{B_2 \cdot f_{2i}}{B_1 \cdot f_{1i}}. \tag{2.30}$$

Formulas (2.28) through (2.30) form a system of equations allowing calculation of the Tromp curve over full range of the particle sizes using only the PSD data of the three material streams. After multiplying Equation (2.28) by f_{3i} and subtracting the result from (2.29), we arrive at:

$$\frac{B_2}{B_1} = \frac{f_{1i} - f_{3i}}{f_{2i} - f_{3i}}. \tag{2.31}$$

Substituting Equation (2.31) into (2.30), the Tromp curve is defined as:

$$Tromp\ Curve = \frac{f_{2i}}{f_{1i}} \cdot \frac{f_{1i} - f_{3i}}{f_{2i} - f_{3i}}. \tag{2.32}$$

Similarly, it can be shown that:

$$\frac{B_3}{B_1} = \frac{f_{1i} - f_{2i}}{f_{3i} - f_{2i}}, \tag{2.33}$$

and the grade efficiency curve is then defined by:

$$GEC = \frac{f_{3i}}{f_{1i}} \cdot \frac{f_{1i} - f_{2i}}{f_{3i} - f_{2i}}. \tag{2.34}$$

The Tromp curve constructed using the particle distribution data presented in Figure 2.15 is shown in Figure 2.16.

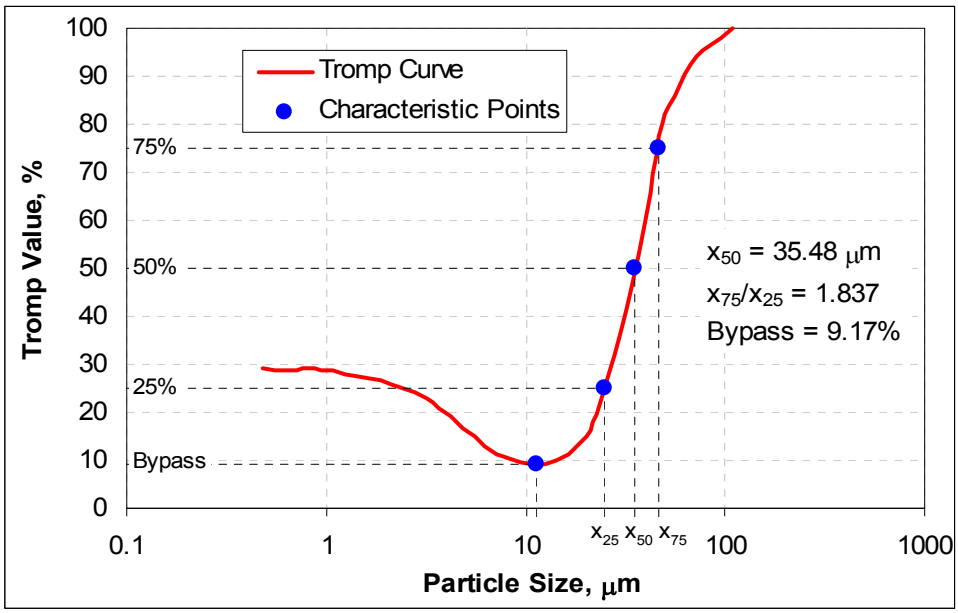

Figure 2.16. Tromp Curve of the High Efficiency Separator.

The Tromp curve has several features important for evaluating the separation process. Some of them have been mentioned earlier in the qualitative description of the separation process. The Tromp curve assigns them numerical values.

- Cut size value
- Sharpness of separation
- Bypass value

The cut size corresponds to the size of particles, which have an equal chance of passing into either the coarse or fine material stream. This particle size has a Tromp value (i.e., the probability of being rejected into the coarse stream) of 50% and is designated x_{50} (see Figure 2.16). The cut size of the Tromp curve is similar in meaning to the size factor of the Rosin-Rammler distribution. The smaller the cut size value, the finer the final product.

The sharpness of separation, k, characterizes selectivity of the classification process in the mid-size range. The higher sharpness of separation value corresponds to a narrower size range of particles that have somewhat comparable chances of passing into either material stream and thus provides for a more precise separation.

$$k = \frac{x_{75}}{x_{25}}, \tag{2.35}$$

where,

x_{25} and x_{75} – Particle sizes with Tromp values of 25% and 75%.

The bypass value defines the portion of the material that bypasses the classifying action. In other words, some part of the feed reports to the coarse stream independently of its particle size due to agglomeration of the fine particles, etc. The lower the bypass, the more efficient the separation.

The high-raised "tail" to the left of the minimum of the Tromp curve shown in Figure 2.16 is another consequence of agglomeration of the fine particles and called the "fish-hook" effect (Benzer et al., 2001). Due to the frictional nature of grinding in the second compartment of the mill, the electrostatic charges are imposed upon the particles leaving the mill. The smaller (lighter) particles are more susceptible to the electrostatic forces and tend to coat larger particles and/or stick together, forming agglomerates. The agglomerates are treated by the separator as particles of larger size and have a higher probability of passing into the coarse stream. Grinding aids help to reduce agglomeration by relieving some of the electrostatic charges imposed upon the particles and thus improve recovery of the fine particles into the product stream (Strohman, 2000; Bhatty et al., 2004).

The efficiency of the classification process can be assessed by comparing the real-life separator (Figure 2.16) to that of an ideal one. The ideal separator would have a Tromp curve completely vertical at the cut size, i.e., characterized by the sharpness of separation $k = 1$ and bypass = 0. All particles larger than the cut size would be sent to rejects (Tromp = 100%), whereas all particles smaller than the cut size would be recovered into the final product (Tromp = 0%) – see Figure 2.17. The ratio of the areas under the Tromp curves of the real and ideal separators defines the separation efficiency (Mizonov et al., 1997).

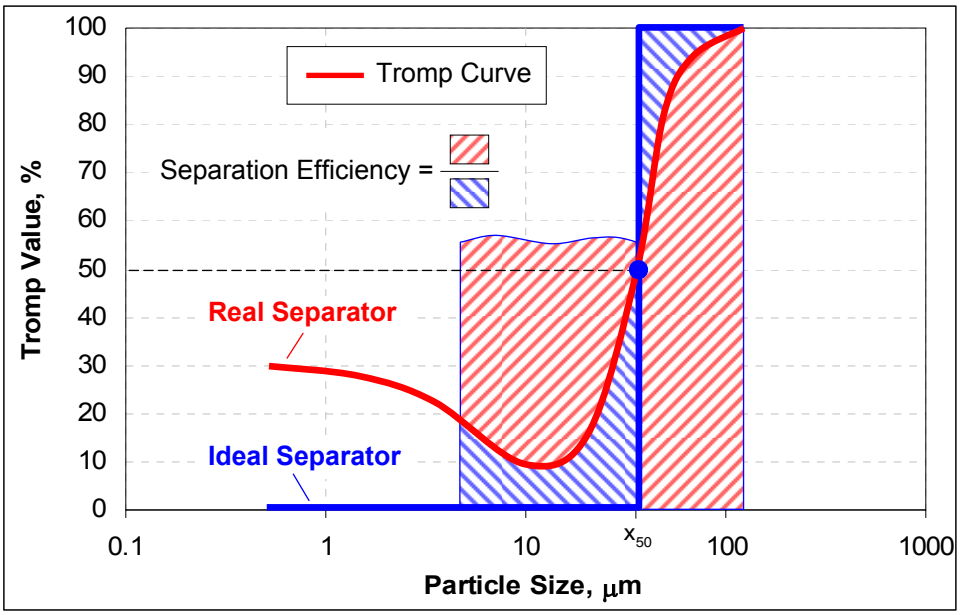

Figure 2.17. Efficiency of the Separator Using Ideal Tromp Curve.

There are certain errors associated with the Tromp curve sample collection and calculation that should be acknowledged and, where possible, eliminated. To minimize the impact of the process fluctuations on the Tromp curve determination, the three material streams surrounding the separator should be sampled simultaneously every 1 to 2 minutes for a duration of about 10 minutes. The averaged PSD results should then be used in calculation of the Tromp curve. It also should be noted that the laser particle size analyzer measures the diameter of an equivalent sphere and does not account for the actual shape of each individual particle. In addition, the PSD data is reported in discrete intervals defined by the size grid of the analyzer and may cause computational discontinuities in the rapidly rising part (right side) of the Tromp curve. Different weighted averaging techniques help in reducing this type of error (Bhatty et al., 2004).

At the cement plant, the separator and the mill are interconnected and operate in a *circuit*. The types of the finish grinding circuits are discussed next.

2.2.3. Finish Grinding Circuits

The idea that the cement mill never works alone, but always in a circuit, has been already introduced earlier. Even the simplest form of the circuit, an *open circuit*, requires a feeding system, material transport system, fans, bag house filters, etc. to complement the operation of the mill (Mizonov et al., 2002).

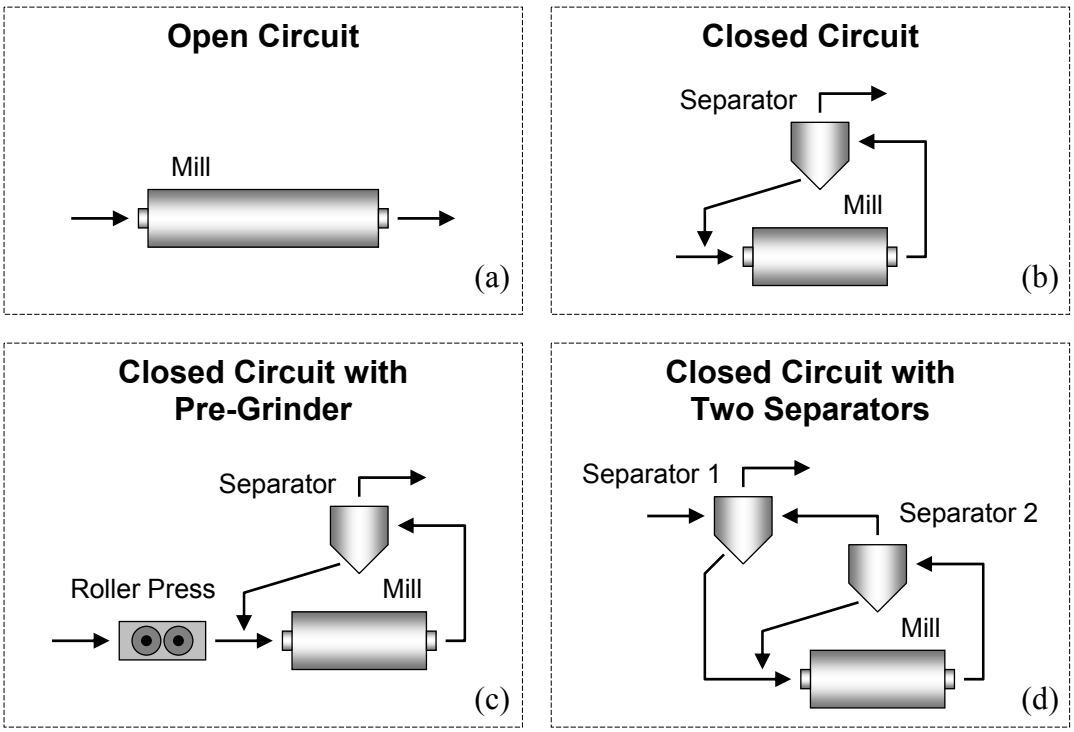

Figure 2.18. Different Types of Cement Grinding Circuits.

In the open grinding circuit shown in Figure 2.18(a), clinker is fed into the mill, and the discharged material directly becomes the final product. Since all the clinker material should be reduced in size in just one pass, longer tube mills prevail in the open circuit installations and have a length-to-diameter ratio between 3.0 and 6.0. The open circuit has a tendency for over-grinding and allows for virtually no fineness control, as its only adjustable process parameters are the feed rate and the air flow through the mill (Kelly and Spottiswood, 1982).

A much higher efficiency and better process control are achieved when grinding in a *closed circuit* (Alsop, 2001). The main principal behind the closed circuit operation is to apply the grinding forces only to the coarse particles and to discharge the fine ones as soon as they have been reduced to the required size. For this, the closed circuits utilize separators and require shorter mills (L/D of 2.8-3.5).

In the most common closed circuit shown in Figure 2.18(b), clinker along with additives first enters the ball mill, after which the ground material is divided by the separator into two fractions. The coarser fraction is sent back to the mill for an additional cycle of grinding, whereas the finer fraction becomes the final product.

More advanced types of closed circuits may include pre-grinders and multiple separators as shown in Figure 2.18(c) and (d). The latter configuration with two separators is used when the feed material already consists of a lot of fines, which should be removed before introducing the feed to the mill (Mizonov et al., 1997).

The rest of the discussion will be devoted to the closed finish milling circuit shown in Figure 2.18(b). Being the most common circuit applied in the cement industry (Bhatty et al., 2004), it is implemented at the pilot cement plant and has generated the field data used in this dissertation.

2.2.3.1. Operation of the Closed Finish Grinding Circuit

The closed grinding circuit is comprised of four basic pieces of equipment: feeder, mill, elevator, and separator (Bhatty et al., 2004). A detailed schematic of the milling system revealing its components is shown in Figure 2.19. The material flow through the circuit has been described earlier.

While the mill is performing the grinding work, the separator removes the finer particles from the mill discharge and prevents them from being over-ground, thereby, saving energy. By extracting part of the material from the grinding process, the separator creates vacant space inside the mill allowing for more fresh clinker to enter the mill, and thus increases the production rate. The operation of the circuit is characterized by several parameters that are closely monitored at the plant. They are summarized in Table 2.6.

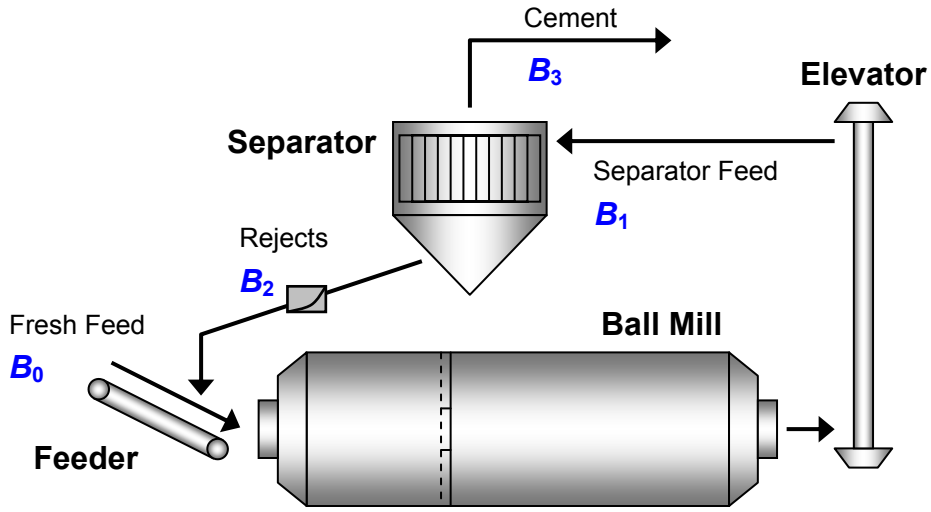

Figure 2.19. Closed Finish Milling Circuit.

Table 2.6. Process Parameters of the Closed Finish Grinding Circuit.

Process Component	Process Parameter	Unit	Affected / Indicated Characteristic
Feeder	Feed rate, B_0	tph	Production rate, mill load
Tube Mill	Motor power Mill sound Mill temperature	kW dB °C	Mill load, process efficiency Mill / compartment load Setting characteristics of cement
Elevator	Motor power	kW	Mill load
Separator	Rotor speed Fan damper position Rejects rate, B_2	rpm % tph	Cement fineness, rejects amount Air flow, cement fineness, rejects amount Recirculation load
Final Product	Blaine value Sieve No. 325	m^2/kg %	Cement quality Cement quality

Fresh feed rate, B_0, is a measure of the production rate and equals the cement flow rate, B_3. By sheer mass balance, the two values must be equal since neither accumulation nor generation of a new material takes place inside the circuit. During a steady-state operation, the feed rate also determines the filling degree of the mill, which, as it was discussed earlier in section 2.2.1.1, influences the grinding efficiency of the

tube ball mill. The weight feeders should be regularly calibrated to maintain reliable and accurate feed rate signals for clinker and its additives.

Power consumption of the mill motor is an excellent measure of the mill's load. The more material is entering the mill, the harder for the motor to turn the mill and the higher the power consumption. Being the most power demanding unit of the cement plant, in general, and the grinding circuit, in particular, the mill power usage per ton of produced cement is an ultimate indicator of grinding process efficiency as well.

In order to evaluate the filling state of the mill's compartments during operation, the microphones are installed close to each compartment. Despite the overall noise accompanying the grinding process, these sensitive microphones are able to pick up the changes in the sound of the mill. An emptier mill will produce a louder sound, whereas the increased amounts of clinker will dampen the clanking noise caused by the grinding media and result in lower decibel values.

About 2% of gypsum ($CaSO_4 \cdot 2H_2O$) is added to the fresh feed mix entering the finish mill. This is done to retard hydration of the aluminate phase (C_3A) of the clinker, which otherwise would react with water immediately (Mehta, 1986). Heat generated in the grinding process forces gypsum to lose water and form hemihydrate ($CaSO_4 \cdot \frac{1}{2}H_2O$) and anhydrite ($CaSO_4$). At high temperatures, excessive amounts of hemihydrate and anhydrite form and, upon addition of water, re-hydrate into gypsum causing a "false set" – a sudden stiffening of the cement mix, which can be reversed by remixing. At low temperatures, insufficient amounts of $CaSO_4 \cdot \frac{1}{2}H_2O$ and $CaSO_4$ will form and the aluminate phase will cause a "flash set" – an irreversible, rapid hardening of the mix (Neville, 1995). Therefore, the mill exit temperature should be kept between 90 and 115°C to ensure proper setting characteristics of the produced cement (Alsop, 2001). Sufficient air ventilation will prevent over-heating of the mill. In addition, water sprinklers are installed at both ends of the mill to control the mill temperature; however, ventilation cooling is always preferable to water spraying.

The elevator motor power is another indicator of the mill load. The elevator is carrying the entire material flow, *throughput*, of the mill, B_3, which consists of the

combined weight of both the fresh feed (B_0) and separator rejects (B_2) streams. When adjusting the circuit operation in an attempt to increase the production rate, the elevator motor capacity should be closely watched for possible overload. Insufficient capacity of the installed motor may prevent increasing the throughput of the mill.

Rotor speed of the separator is an important parameter in controlling the cement fineness characteristics. As described in section 2.2.2.1, increasing the rotor speed will elevate the final product fineness and increase the rejects flow rate, B_2, since more particles will be returned back to the mill. The rotor drive system has its own capacity, which determines the maximum possible speed of the rotor.

The air passing through the separator is usually supplied by an individual fan and adjusted by a remotely controlled damper. Sufficient amount of air in the classification zone is crucial for adequate separation since the classification process takes place, when the material particles are thoroughly suspended in air. The higher air flow inside the separator will carry more particles of larger size into the fine stream. This will decrease the product fineness and decrease the rejects flow rate, B_2.

The rejects flow rate, B_2, is an important process parameter of the closed grinding circuit and is usually measured by an impact flow meter (Bhatty et al., 2004). At a constant fresh feed rate, B_0, any variations in the rejects flow rate, B_2, will alter the throughput of the mill, B_3. This will change the ratio of the throughput to the fresh feed rate defined as the *recirculation load* and will be addressed later. Finally, the fineness of the ground product substantially affects the cement performance characteristics as it was described in section 2.1.3.

At a modern cement plant, all of the listed process parameters are registered in-situ in the form of electronic signals (Alsop, 2001), which are then delivered to the plant's control room and stored in a large process database called Process Data Historian (PDH). The PDH system can be queried both in tabular and graphical forms to obtain the process values during a specified time period. This tremendously facilitates retroactive analysis of the grinding process. The graphical representation of the PDH system implemented at the pilot plant is shown in Figure 2.20.

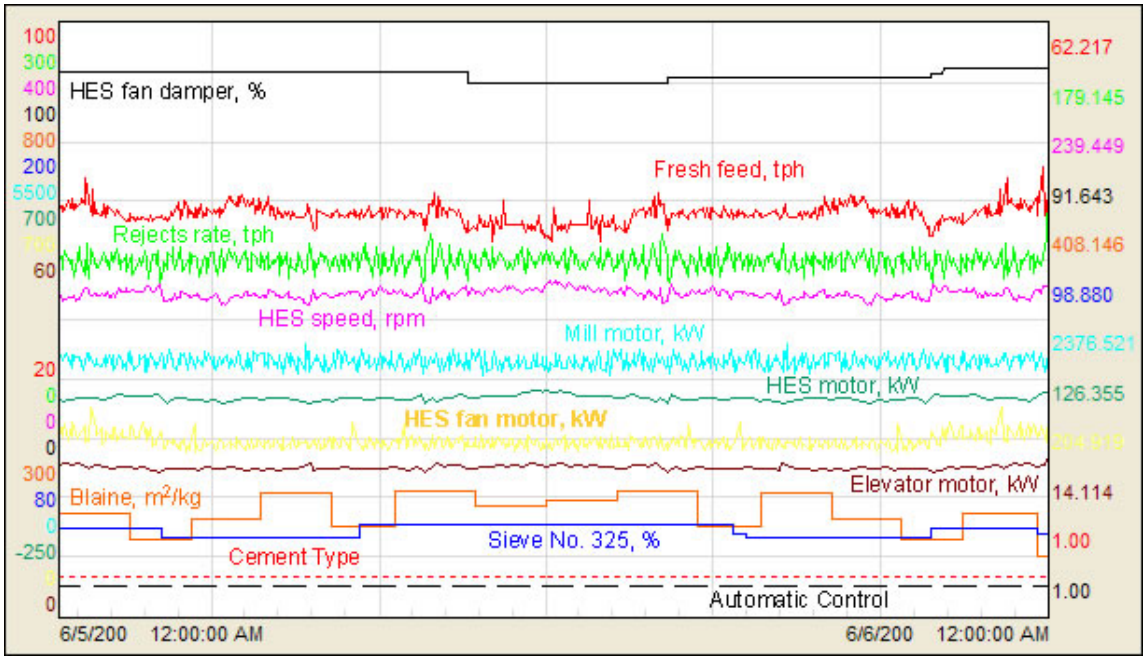

Figure 2.20. Graphical Representation of the Process Data Historian.

2.2.3.2. Characteristics of the Closed Finish Grinding Circuit

One of the characteristics of the closed milling system is the particle size distribution of the material in each stream of the circuit. The three material streams (see B_1, B_2, and B_3 in Figure 2.19) surrounding the separator have been described previously. The PSD of the material entering the mill is comprised of the size distributions of the fresh feed, B_0, and the separator rejects, B_2.

To evaluate the recirculation of the coarse particles in the circuit, two correlated parameters are calculated:

- Circulating load, and
- Circulating factor.

The circulation load is the average number of times that the material circulates through the circuit before becoming the product. A harder clinker will yield a higher circulation load. It is defined by the ratio of the mill's throughput, B_1, to the product flow

rate, B_3. The circulating factor is the quantity of the separator rejects, B_2, compared to the quantity of the final product, B_3. With this, the following expressions hold.

$$\text{C.L.} = \frac{B_1}{B_3} = \frac{B_0 + B_2}{B_0}; \tag{2.36}$$

$$\text{C.F.} = \frac{B_2}{B_3} = \frac{B_2}{B_0}; \tag{2.37}$$

$$\text{C.L.} = \text{C.F.} + 1, \tag{2.38}$$

where,

C.L. – Circulation load of the closed milling circuit;

C.F. – Circulation factor of the closed milling circuit.

The Equations (2.36) and (2.37) are also expressed in terms of B_0 and B_2 material flows, since these two material flows are actually measured. From the circuit mass balance, the product flow, B_3, is equal to the fresh feed flow, B_0, and the throughput, B_1, is calculated using Equation (2.28).

It also should be noted that the circulation load can be calculated for each individual fraction determined by the laser particle size analyzer using separator material PSD data, expressed in the form of the individual retained functions, *f(x)*. Indeed, the Equation (2.33) is the inverse of the circulation load as defined in (2.36).

$$\text{C.L.}_i = \frac{B_1}{B_3} = \frac{f_{3i} - f_{2i}}{f_{1i} - f_{2i}}, \tag{2.39}$$

where,

C.L.$_i$ – Circulation load of the i-th fraction.

Theoretically, the weighted average over all individual circulation load values, C.L.$_i$, should be equal to the overall C.L. value as defined in Equation (2.36). In reality, it is rarely the case due to computational errors associated with the collection and measurement of the PSD data (see discussion on errors in the calculation of the Tromp curve in section 2.2.2.2).

2.3. CLINKER GRINDABILITY

The ball mill provides the *means* for grinding clinker and its additives; the process parameters of the circuit tell us *how well* the grinding is done. But it is also necessary to understand the essence of *what* the ball mill is grinding. In this section, the clinker grindability properties will be reviewed.

The finish grinding does not process solely clinker. It is also used to blend different additives into the final product (Bhatty et al., 2004). For instance, gypsum is added to the clinker to control the setting behavior of the cement mix (Neville, 1995); inclusion of limestone allows for improvement of some of the cement performance characteristics as well as reduction of the manufacturing costs of the product (Hawkins et al., 2003). In case of blended and masonry cements, clinker may be mixed with large quantities of natural pozzolans, fly ash, silica fume, granulated blast furnace slag, metakaolin, and other materials (Bhatty et al., 2004). Grinding aids are added to the finish mill to facilitate comminution and prevent agglomeration of the material by relieving the electrovalent charges along the fracture lines of the ground particles (Strohman, 2000). Water spraying may be used to control the temperature inside the mill, which also improves the flow of the clinker material.

All of the mentioned additives impact grindability of the clinker mix. Some of them enhance grindability (gypsum, limestone, water) and other decrease it (granulated blast furnace slag): Tsivilis et al. (1999), Fortsch (2005).

The grindability of clinker should be reviewed as it is the main constituent of the fresh feed mix entering the finish mill. But it is important to remember that the additives have a strong effect on the ease of grinding. Methods evaluating grindability of the feed mix as a whole provide a better representation of the mill operation and are more applicable in the industrial set-up.

It should be noted that the term "grindability" is used here in a positive connotation, i.e., an increase in grindability results in a decrease of both the resistance to grinding and the energy required to reduce clinker to a desired fineness.

2.3.1. Chemistry and Microstructure of Clinker and Its Grindability

The grindability of clinker depends on its chemical composition and the contents of the phase minerals. The chemistry and mineralogy of clinker are primarily based on its raw mix design, however, the macro and microstructural characteristics of the clinker are also influenced by such factors as the burning and cooling conditions, fineness of the raw mix, type of the clinkering process (wet or dry), origin of the kiln fuel, and others (Juhasz and Opoczky, 1990).

The main mineralogical constituents of the cement clinker can be calculated using the Bogue equations. Although not strictly accurate, these formulas provide close estimations for the quantities of the phases based on the oxide contents of the raw mix (Bhatty et al., 2004; ASTM C150).

If $Al_2O_3 / Fe_2O_3 \geq 0.64$ (2.40)

$$C_3S = 4.07\ CaO - (7.60\ SiO_2 + 6.72\ Al_2O_3 + 1.43\ Fe_2O_3 + 2.85\ SO_3)$$
$$C_2S = 2.87\ SiO_2 - 0.75\ C_3S$$
$$C_3A = 2.65\ Al_2O_3 - 1.69\ Fe_2O_3$$
$$C_4AF = 3.04\ Fe_2O_3$$

If $Al_2O_3 / Fe_2O_3 < 0.64$ (2.41)

$$C_3S = 4.07\ CaO - (7.60\ SiO_2 + 4.48\ Al_2O_3 + 2.86\ Fe_2O_3 + 2.85\ SO_3)$$
$$C_2S = 2.87\ SiO_2 - 0.75\ C_3S$$
$$\text{Solid Solution } (C_4AF + C_2F) = 2.10\ Al_2O_3 + 1.70\ Fe_2O_3$$
$$C_3A = 0$$

Hills (1995) prepared an extensive overview of the literature studying the relationship between the mineralogy, microstructure, and grindability of clinker. The author summarized effects of several parameters on grindability of each clinker phase and presented the following conclusions.

Generally, a cement clinker containing higher quantities of alite (C_3S) and lower quantities of belite (C_2S) has a better grindability and lower specific weight. The "intermediate" phases (C_3A and C_4AF) are among the hardest, but their effect on overall

grindability is not clearly determined (also Juhasz and Opoczky, 1990). Conclusions regarding the optimal cooling rates for different phases vary significantly depending on the mineral composition of the clinker. Smaller crystals and a poorly defined structure with no sharp edges are shown to enhance grindability of both alite and belite phases. Agglomeration during grinding impairs grindability and is more prominent in the belite phase than alite.

Factors not related to the four dominant mineralogical phases also have an effect on the clinker grindability. Hills (1995) suggested that MgO (periclase) in excess of 2% may negatively affect grindability, whereas free lime (CaO) improves it (also Velez et al., 2001). Large clinker nodules and fine dust are more difficult to grind, but decreased temperature of the fresh feed (50-60°C) reduces resistance to grinding.

In order to subject the grindability of clinker to a meaningful analysis, it has to be associated with some numerical value. It can be a direct measurement of toughness or hardness of the clinker nodules, but it appears to be more suitable to measure grindability in terms of the energy required to produce a certain level of fineness (Juhasz and Opoczky, 1990). Hills (1995) reported an extensive list of investigations in this area of research. For example, Theisen (1993) established a correlation between the specific power consumption of the ball mill, pulverizing clinker to three Blaine surface values (250, 300, and 350 m^2/kg), and a set of parameters characterizing the material: Bogue-calculated belite content (C_2S), microscopy measurements of alite grain size, porosity, and pore intersection. Some of the early foundational work on the laboratory testing is described below.

2.3.2. Laboratory Techniques of Measuring Clinker Grindability

All of the laboratory techniques have the same common principle. The material sample of a certain weight is placed into a miniature mill of known dimensions and subjected to a number of grinding cycles, after which the energy consumption of the mill is recorded and the resulting sample fineness is measured.

One of the grindability tests, Hardgrove's method, was developed for determining relative grindability of coal and is standardized in ASTM D 409. This method is based

on the premise that the energy expended for grinding is proportional to the area of the new surface created. For this, a prepared and sized sample receives a definite amount of grinding energy in a laboratory grinding bowl. The pulverized sample is then sieved and the portion of the material passing through the No. 200 (75 μm) sieve is converted to a Hardgrove's grindability index using a regression formula. The Hardgrove's method is only suitable for fracture and coarse grinding when compared to a standard sample (Juhasz and Opoczky, 1990).

$$HGI = 10.63 + 6.75 \cdot Q_{200}\,, \tag{2.42}$$

where,

HGI – Hardgrove's grindability index as per ASTM D 409;

Q_{200} – Portion of a 50 g sample passing through sieve No. 200 (75 μm).

The Zeisel's method is a variation of the Hardgrove's test and applied in the cement industry (Mishulovich, 2004). The clinker sample is ground to a preset fineness (e.g., Blaine value of 300 m^2/kg) by gradually increasing the grinding time. The energy consumption is determined by momentum measurements. The specific grindability is calculated from the supplied grinding energy as (Juhasz and Opoczky, 1990):

$$W = \frac{0.275 \cdot W_{gr}}{m}\,, \tag{2.43}$$

where,

W – Specific energy (grindability);

W_{gr} – Consumed grinding energy;

m – Mass of the sample.

The results of the Zeisel's test are usually presented as the specific energy consumption per weight of the ground material plotted against the achieved specific surface area (Gill, 1999). An example of such a plot is shown in Figure 2.21.

Bond's method simulates grinding in a closed circuit using a miniature ball mill. After each cycle of grinding, the product is discharged from the mill and screened on a test sieve. The fresh feed is added to the oversized material to bring the total weight of

the sample back to that of the first grinding cycle. The new charge is fed into the mill and the number of the subsequent mill revolutions is calculated to produce a 250% circulation load of the circuit. The procedure is repeated until the weight of the under-size fraction becomes constant for the last three grinding cycles (Magdalinovic, 1989).

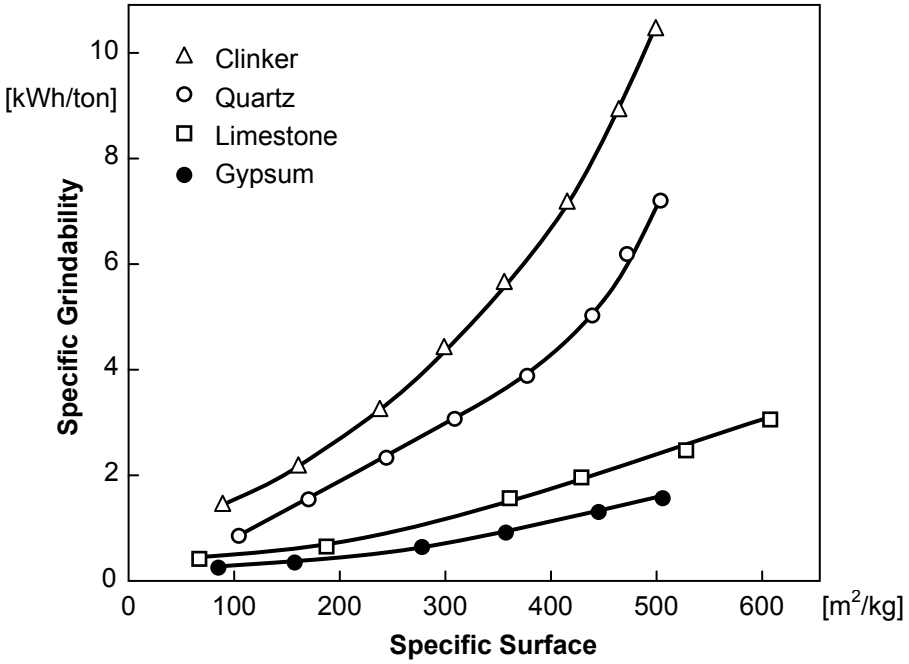

Figure 2.21. Grindability vs. Blaine Value by Zeisel Method
(After Juhasz and Opoczky, 1990).

The advantage of the Bond's method is in representation of the entire grinding process during both pulverization and classification stages and not just the process inside the ball mill alone. The specific grinding energy, W, according to Bond is calculated as:

$$W = \frac{16}{G^{0.82}} \sqrt{\frac{r}{100}}, \tag{2.44}$$

where,

r – Test sieve mesh opening, μm;

G – Mass of the under-size material per one mill revolution, g/min.

Having vast capacities, many large cement producers develop their own clinker grindability tests. These include establishing relationships between the consumed energy and parameters of the Rosin-Rammler distribution of the product's PSD, elaborating microstructural analysis methods, such as Ono technique, developing company-specific laboratory ball mill procedures, and other methods (Laurent, 1997; Hills, 1999).

2.3.3. Laws of Grinding

Ultimately, all research efforts in the clinker grindability area are targeted at deriving the relationship between the fineness of the ground product and consumed grinding energy. The most widely accepted inferences on this relationship were made by Rittinger, Kick, and Bond (Mizonov et al., 1997). These researchers related the average particle sizes of the sample before and after the grinding procedure to the specific energy input, required to produce the corresponding size transformation.

The three "laws" of grinding are defined by the following equations.

$$W = C_1\left(\frac{1}{x_2} - \frac{1}{x_1}\right) \qquad \text{– Rittinger's law;} \tag{2.45}$$

$$W = C_2\left(\frac{1}{\sqrt{x_2}} - \frac{1}{\sqrt{x_1}}\right) \qquad \text{– Bond's law;} \tag{2.46}$$

$$W = C_3 \ln\frac{x_1}{x_2} \qquad \text{– Kick's law,} \tag{2.47}$$

where,

W – Specific grinding energy;

x_1, x_2 – The starting and final particle sizes;

C_i – Grinding constant, corresponding to each law (i = 1, 2, and 3).

All three equations above can be described by a general differential equation, relating comminution energy and particle size (Mishulovich, 2004).

$$\frac{dW}{dx} = -C_i \cdot x^{-p}, \tag{2.48}$$

where,

x – Size of the particle, subjected to grinding;

p – Comminution parameter defining the appropriate grinding law.

In the case of Rittinger's law, the comminution parameter in Equation (2.48) has a value of $p = 2$; for Bond's law, $p = 1.5$; and, for Kick's law, $p = 1$.

Rittinger's law suggests that the energy consumption of grinding is proportional to the new surface produced by the process. The law is based on the effective work required to overcome cohesion and does not take into account the much greater energy absorbed by elastic deformation. However, it correctly reflects the increase of energy with progressive comminution. Bond's law suggests that the grinding energy is proportional to the new crack length developed by the comminution process (Juhasz and Opoczky, 1990). Finally, Kick's law suggests the equivalence of the fracture energy and the energy associated with elastic stretching and the proportionality of these energies to the volume of the ground body. It assumes that the energy demand is independent of the achieved particle size, which is not true in fine grinding (Mishulovich, 2004).

All three theories treat the ground material as consisting of only single-sized particles and lack acknowledgement of the full particle size distribution of the feed and the product streams. They do not address particle interactions and overlook the energy consumed by plastic deformation. The amendment to the laws proposed by Holmes takes into account the PSD of the material in the beginning and end of the grinding process (Juhasz and Opoczky, 1990):

$$W = C_4\left(\frac{1}{x_2^{n_2}} - \frac{1}{x_1^{n_1}}\right), \tag{2.49}$$

where,

x_1, x_2 – The average particle sizes of the feed and the product;

n_1, n_2 – Uniformity factors of the particle size distributions.

Other modifications of the grinding laws included consideration of the grinding media effect and the energy spent for plastic deformation and particle interaction.

However, these modifications demonstrate a highly empirical nature in their mathematical formulation and are somewhat difficult for application (Juhasz and Opoczky, 1990).

Being in compliance with the second law of thermodynamics, the presented comminution laws are fundamental in principal. Many mill models, including the Markov chain model, incorporate these laws in order to describe the comminution processes (Mizonov et al., 2002).

2.3.4. Specific Energy Consumption of the Ball Mill

When applied to the cement finish milling on an industrial scale, the presented grinding laws may deliver only limited accuracy (Juhasz and Opoczky, 1990). The cement production is characterized by a multifold particle size reduction, which is hard to describe using the comminution laws in their pure form. In addition, the laws do not take into account crushing processes that occur in the first compartment of the ball mill and are different in mechanism from the grinding processes.

It happens so that the industrial ball mill itself can act as a clinker grindability gage. The process data historian registers all the necessary process parameters: the mill motor power, the material flow rates, and the product Blaine surface. Moreover, since all of the modern cement plants are equipped with quality control labs, the mineralogical composition and, in some places, microscopy characteristics of the produced clinkers are also determined. In essence, the cement plant is continuously running the clinker grindability test. This test provides the most representative milling data and accounts for all outside factors that influence the grindability of the clinker mix: inclusion of mineral additives and grinding aids, temperature conditions, different nature of the comminution forces in the compartments of the ball mill, etc.

The PDH data from the pilot cement plant was used to produce the graph shown in Figure 2.22, where the specific energy consumption of the tube ball mill per ton of the final product is plotted against the fresh feed (production) rate. The data used in this figure was sorted and filtered to isolate the time periods, when the circuit operation was stable exhibiting only minor changes of the process parameters, the mill was producing cement of the same type, and the Blaine area of the product averaged at 380 m^2/kg.

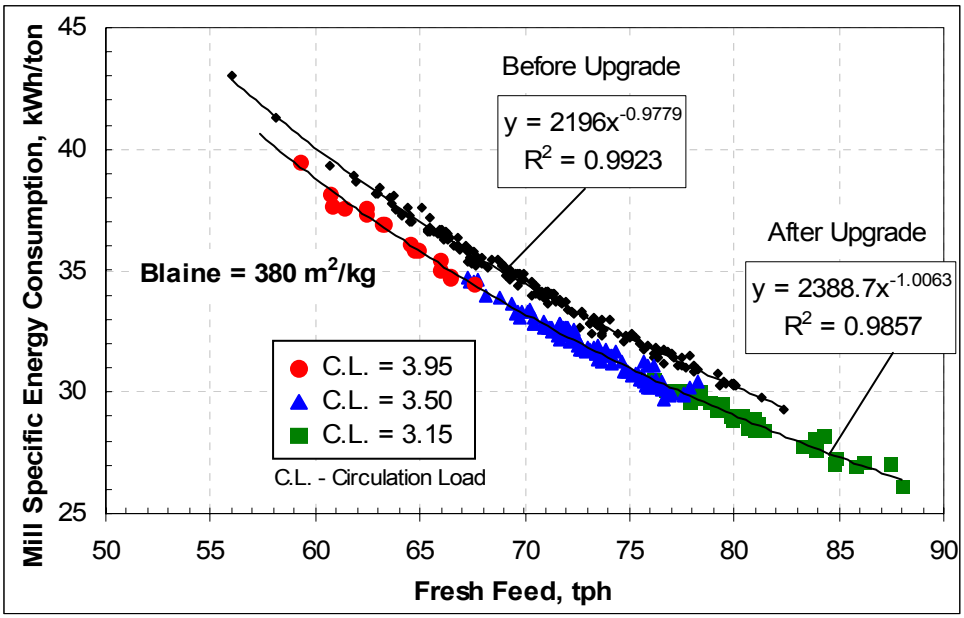

Figure 2.22. Specific Energy Consumption of the Tube Ball Mill.

Even if the chemical composition of the raw mix is constant, the grindability of clinker (i.e., its "softness") may fluctuate depending on its burning, cooling, and storing conditions. At the same time, the mill upgrades, including the ball charge and shell liners maintenance, impact the robustness of the ball-clinker interaction and the lifting/sorting action of the liners. The periodical maintenance procedures improve the mill's ability to grind and compensate for a heavy wear of the grinding media. Also, the ball mill may not be run consistently from one work shift to another. The manner, in which the ball mill is operated, significantly influences its performance. For example, the material level inside the mill may be too high and impair the optimal ball-clinker interaction, reducing the grinding efficiency.

Thereby, the *grindability* of the clinker mix should be distinguished from the *grinding ability* of the ball mill. The former is due to the properties of the clinker mix, the latter is due to the installed hardware and the way it is operated. The common "denominator" of the two grindability aspects, however, is the consumed electrical energy required to produce a desired level of cement fineness.

The two curves in Figure 2.22 reveal both aspects of the grindability: material-based and equipment-based. The ball mill underwent a maintenance procedure and showed an improved specific energy consumption immediately following the upgrade. The lower curve corresponds to the operation after the upgrade and demonstrates a relative efficiency improvement of about 3.8% for the fresh feed rate of 75 tph.

The lower curve is also displaying the effect of the clinker grindability on the energy consumption of the mill. Harder clinkers require more passages through the mill and yield higher values of the material circulation load (C.L.). Softer clinkers, on the other hand, bear lower circulation loads, leave the mill after fewer passages, and thus create a vacated space in the mill, which can be taken up by the fresh feed: the lower circulation loads correspond to the higher fresh feed rates (see Figure 2.22).

Analysis of the grindability graph uncovers that the equipment alteration causes a parallel shift of the curve, whereas the change in the clinker hardness induces a slide of the specific energy value along the grindability curve.

The general trend of the curves reveals that the lower specific power consumption is achieved for the higher fresh feed rates (the curve has a decreasing pattern). This can be explained by the fact that most of the ball mill weight is caused by the weight of the grinding media, whereas the clinker material constitutes only a small portion of the total weight. If the production rate goes up, the ball mill total weight increases only marginally, but the ratio of the consumed electrical energy to the production rate drops quite noticeably.

The described phenomenon suggests that in order to reduce the specific power of the cement finish milling process, the production rate should be maximized. The amount of the consumed electrical energy per ton of produced cement then will be at its lowest.

The above recommendation is in line with the manufacturer's attempt to satisfy the continuously increasing cement demand. This conclusion also provides basis for one of the essential principles used in formulation of the finish mill control objective for the proposed Markov chain model.

2.4. SIMULATION AND CONTROL OF CLINKER GRINDING

Industrial simulation, control, and optimization are all interrelated and driven by the same basic aspiration of improving the efficiency of a particular process. The main goal of *simulation* is to obtain an inexpensive tool that can be used to maximize the *efficiency* of the industrial equipment via physical *upgrade* of the corresponding equipment or refinement of the process *control* strategy (see top of Figure 2.23).

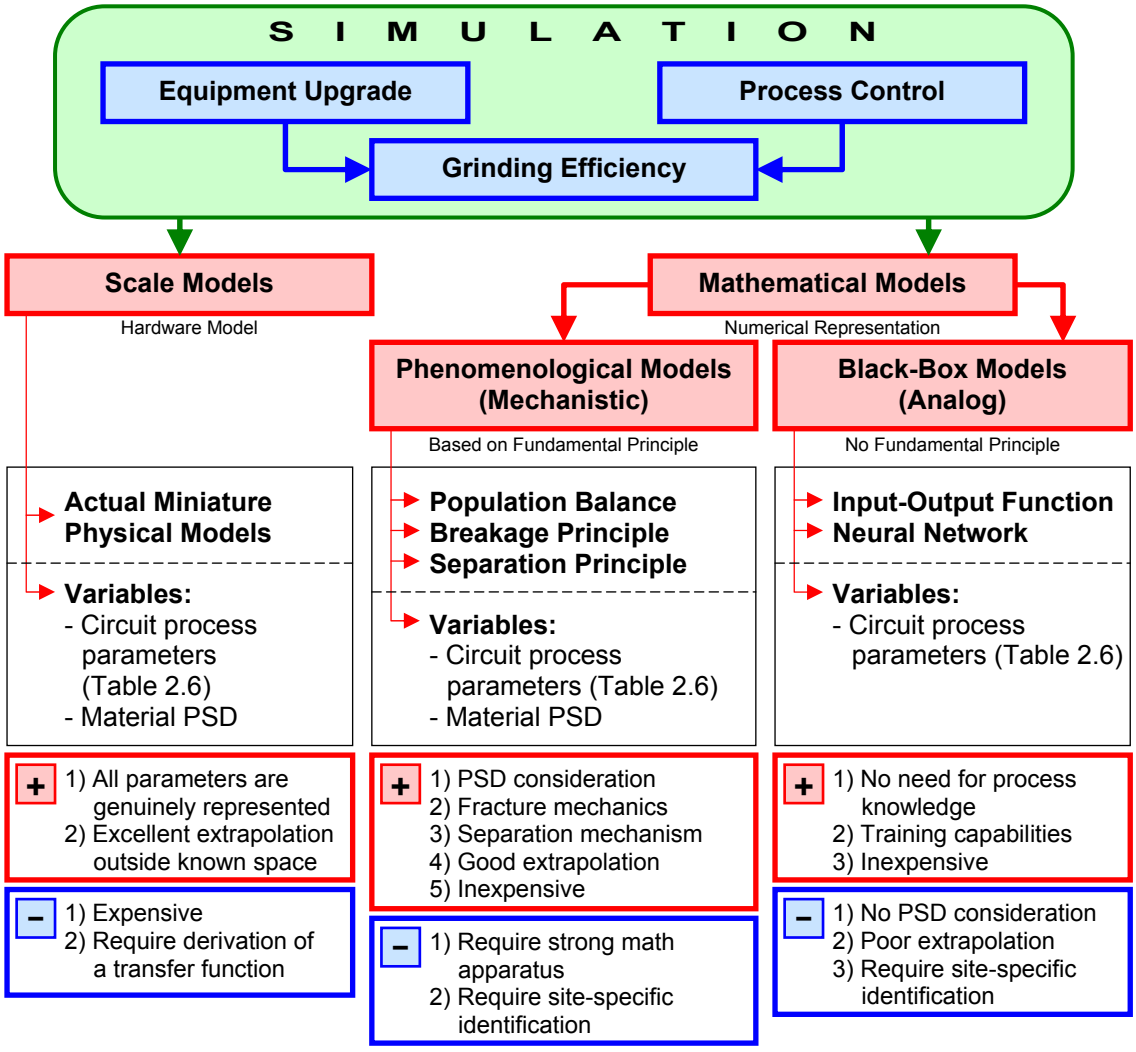

Figure 2.23. Comparison of Different Types of Grinding Simulation Methods.

The physical upgrade of the grinding and associate equipment involves selection of the characteristics of the grinding system that provide maximum energy efficiency of the process while achieving the targeted cement fineness. The modern state of the cement industry is such that practically all first order technological improvements have been already identified and applied to the finish milling equipment. Further advancement is possible through a detailed analysis and understanding of the process relationships, which entails deciding how to manipulate the grinding equipment in order to reach the desired energy and fineness targets. This task requires costly experimental investigations, which, however, can be substituted by the numerical simulations.

In analysis, the grinding equipment and underlying physical phenomena can be replaced by models adequately representing either the entire milling process or just its particular trend. This provides a relatively inexpensive tool for plant and process design, performance evaluation and assessment, and equipment and process tuning.

2.4.1. Simulation of Grinding Process

Simulation of grinding circuits is a widely applied practice that permits exploring and evaluating the complex interactions between different unit operations within the circuit at a low cost (King, 2001). The simulation techniques can be divided into two major categories (see Figure 2.23):

- Scale models, and
- Mathematical models

The scale model is based on a *physical* representation of the grinding circuit at a reduced size and assumes an empirical type of investigation. The results of scale modeling can be applied to the circuits of the original size by means of transfer functions.

The benefit of the scale simulation is in the fact that these models consist of the actual operating units of the corresponding grinding equipment. The physical processes of grinding and separation (if in closed circuits) are genuinely represented here, only at a smaller scale. The laboratory ball mill is one of the examples of a scale model that proved to be an essential aid in the analysis of the industrial milling equipment. The disadvantages of the scale approach include a necessity to fabricate the model itself,

which requires a certain level of available resources, and a difficulty in transferring the modeling results to the original scale.

A vast test program using both laboratory and semi-industrial ball mills was carried out by Schnatz (2004). The author investigated the influence of the length-to-diameter ratio, ball charge filling ratio, ball size gradation, and feed residence time on the specific energy consumption of the ball mill operating in a closed circuit. The feed materials of two different finenesses were included in the test program. The results showed the existence of definite optimal values for L/D ratio, ball charge filling ratio, and retention time, at which the specific energy consumption was minimal. The coarser feed material required a higher optimal L/D ratio of about 2.7 compared to the finer feed with an optimal L/D ratio of about 2.3. A multi-sized ball gradation proved to be slightly more efficient than the mono-sized gradation with the same average ball diameter.

Touil et al. (2006) studied the clinker breakage rate and grinding energy requirements in a laboratory ball mill. The influence of two admixtures (gypsum and pozzolanic tuff) on the clinker grindability was evaluated. It was shown that these materials decrease the specific energy consumption of the mill for a given Blaine fineness. The authors also concluded that the energy efficiency of cement finish grinding can be increased by reducing the initial rate of particle breakage.

Findings of the scale based research similar to that performed by Schnatz (2004) and Touil et al. (2006) provide straightforward recommendations for a physical upgrade of the milling equipment that ensure its improved energy performance.

The mathematical modeling is based on a *numerical* representation of the milling equipment and requires a certain conceptual foundation for simulating the circuit's behavior. Due to the complexity of the physical processes taking place inside the grinding circuits, almost all comminution models are strongly nonlinear (King, 2001).

The mathematical models can be divided into two groups:

- Phenomenological (or mechanistic) models, and
- Black-box (or analog) models

The phenomenological (mechanistic) approach models the physical phenomenon that is inherent to the grinding process (King, 2001). The black-box (analog) approach, on the other hand, estimates the functional relationship among the circuit variables and the numerical parameters in those functions without prior knowledge about the physical nature of the system being modeled.

2.4.1.1. Black-Box Simulation

The goal of the black-box simulation is to tie together the input and output variables of the system without modeling the physical processes inherent to grinding and classification (see Figure 2.23). Examples of the black-box approaches include polynomial regression and neural network. The former uses curve fitting and the latter employs so called *training* in order to derive the sought functional relationships.

Breusegem et al. (1994) proposed a multivariable black-box model of a closed circuit, which was applied to formulate a liner-quadratic control strategy of the milling process. In this strategy, two output variables (rejects and product flow rates) were regulated by means of two adjustable input variables (fresh feed rate and separator speed). The core of the model was provided by a system of four first-order differential equations describing operation of the circuit around a certain nominal point and tying together the four abovementioned variables. The fineness control was not included in the model and was performed by a traditional manual change of the separator speed. Improved circuit stability was reported as a result of the industrial application of the proposed model.

The neural network variation of the black-box models started gaining popularity in the recent years (Martin and McGarel, 2001; Topalov and Kaynak, 2004). The development of a neural network model is split into two parts: model training and model verification. During the training period, either the on-line or backed-up process data is used to establish the model functions and their parameters. Then, during the verification period, the performance of the model is assessed for the data set different from that of the training period.

Due to strong non-linear characteristics of the milling process, extrapolation of the circuit's operation beyond the training data range is a serious challenge for the neural

network models despite their high adaptive capability. The lack of knowledge about the comminution principles decreases the functionality of the empirical models like neural network outside the normal range of operation (King, 2001).

A more detailed discussion on the neural network approach is beyond the scope of this dissertation. Examples of the research work implementing neural network models are provided below.

Martin and McGarel (2001) developed a neural network model for calculating non-linear changes (gains) of the milling process parameters and used the calculated changes in a model predictive control of the circuit. The model consisted of 2 input parameters: fresh feed rate and separator speed; and 4 monitored output parameters: Blaine value, rejects rate, mill sound, and mill motor power. The results section of the paper does not provide any tangible numerical data and is limited only to general statements that the production rate increase was comparable to that of other mill control systems and the cement consistency and quality were improved.

Topalov and Kaynak (2004) presented a neural predictive model based on the sliding mode control theory capable of estimating the one-step-ahead errors in control signals. The model consisted of 2 input parameters: fresh feed rate and separator speed; and 2 monitored output parameters: final product flow rate and mill load. Observing both fresh feed and product flow rates enabled the authors to develop a strategy that ensured a plug-free operation of the circuit (e.g., plugging of the division screen between the compartments of the tube ball mill). No fineness control was implemented in the proposed model. The authors reported shorter transition times of the circuit with undershoots and overshoots of smaller magnitudes compared to a referenced neural network model.

It should be noted that none of the research efforts described above considered the full span of the cement particle sizes and utilized only bulk process parameters such as Blaine value, fresh feed rate, returns rate, and separator speed (see Table 2.6). In order to influence the performance characteristics of the cement and be able to produce desired particle size distribution, it is necessary to employ a simulation method that would have sufficient knowledge of the physical processes occurring in the milling circuit.

2.4.1.2. Phenomenological Simulation

The main advantage of the phenomenological approach is due to its knowledge of the fundamental principle underlying the process. If the mechanistic principle of a particular process is adequately formulated and incorporated into simulation, the phenomenological model does not require modifications in order to respond to the new process data. Both interpolation between the known data points and extrapolation of the operation outside the initial calibration space are handled in a stable manner (King, 2001).

The population balance method and the breakage and classification functions are the most widely used approaches in the phenomenological modeling (see Figure 2.23). The population balance entails dividing the particles into classes, accounting for the behavior of each individual class, and describing the statistical properties of the particle populations. The breakage and classification functions model the corresponding processes inside the grinding and separating equipment and will be described later.

In a multi-stage industrial process like cement grinding where different types of forces act upon the particles in each stage, the population balance models are particularly advantageous. They permit a more precise accounting for different fracture mechanisms, such as crushing and attrition, and attributing the results of both grinding actions to a single piece of equipment. The population balance approach provides basis for the application of the breakage and separation functions in each particle class and is ideal in simulation of processes, where product of one operating unit becomes the feed material for another (King, 2001).

Mizonov et al. (1997) utilized a population balance approach and proposed a method for modeling the comminution processes by employing the breakage functions, the laws of grinding, and the second law of thermodynamics (see section 2.3.3). The authors formulated a unique strategy for combining the separate units of the grinding circuit into a single matrix-based model, connecting different stages of the process and simulating the material flow through the circuit.

King (2001) summarized approaches in modeling various types of industrial mills, determining their characteristics, and estimating their breakage functions.

Benzer et al. (2001) analyzed 26 clinker grinding circuits including the tube mills, air separators, and high pressure grinding rolls. They showed that the tube mills can be modeled as several mills in series, and the internal partition inside the tube mills can be modeled as a screen, which should retain coarse particles in the first compartment, but not obstruct the air flow. The authors determined the fracture properties of the clinker particles in different size fractions and applied them to the breakage functions describing the mills. The air separators were modeled using the efficiency (Tromp) curves. The results of the simulation revealed that the data obtained from one cement circuit could be used to predict performance of another circuit working at different conditions. The predicted particle size distributions of the material at different points of the grinding circuit closely matched those observed. The model was reported to be capable of determining the optimal top ball sizes, slot openings of the division screen between the compartments in the tube mill, ball load, and other equipment based modifications.

Delagrammatikas and Tsimas (2004) applied the Rosin-Rammler representation of the particle size distribution of cement to simulation of grinding in a tube ball mill. The authors proposed a time-dependent function describing evolution of the parameters of the Rosin-Rammler distribution and characterizing passage of the clinker material through the mill. A close similarity of the calculated and observed PSD was achieved in the last stages of the grinding process (towards the outlet of the mill).

The examples of the phenomenological modeling show that simulation methods accounting for the PSD of the material at different points of the grinding circuit do exist. However, none of the reviewed approaches possesses the functionality and flexibility of the method based on the Markov chain theory. In fact, the Markov chain approach can be viewed as a synthesis of all mechanistic models developed for the grinding technology (see Figure 2.23). While capable of accounting for the breakage and separation functions, circuit process parameters, physical movement of particles within the circuit, and material's PSD, its functionality is greatly boosted by a flexible mathematical apparatus based on matrix algebra. Because of this, the Markov chain theory is the approach of choice for the proposed dissertation and is overviewed next.

2.4.2. Basic Concepts of the Markov Chains

The theory of Markov chains was developed by a Russian mathematician Andrey Markov in 1907, but the concept was not applied to engineering problems until half a century later (Kemeny and Snell, 1960). The very first elaborations of the theory were devoted to presentation of the processes with distributed property parameters and continuous time. Only with emerging computer technology, which allowed discrete representation of the Markov chains, the practical uses of the theory found their application (Mizonov et al., 2004).

Today, the Markov chain approach is used in modeling physical, engineering, biological, and social systems such as population dynamics, manufacturing systems, and queuing networks. Special applications of the theory have also been seen in the areas of wireless communications, internet traffic design, and financial engineering (Yin and Zhang, 2005). With regard to comminution systems, the theory provides an effective mathematical tool allowing an efficient computational analysis of the processes of grinding and classification and has been successfully applied by several authors: Tamir (1998), Berthiaux et al. (2000, 2005), Mizonov et al. (2002, 2004).

The Markov chain employs probabilistic techniques in representing the process being modeled. If X is a variable taking random values y_1, y_2, … y_m, then the formal definition of a Markov chain is given by the following (Berger, 1993):

$$\mathrm{P}\left(X_{m+1} = y_{m+1} \mid X_1 = y_1, \ldots, X_m = y_m\right) = \mathrm{P}\left(X_{m+1} = y_{m+1} \mid X_m = y_m\right) \tag{2.50}$$

Expression (2.50) states that given all preceding values y_i of variable X, where index $i = 1, 2, \ldots, m$ with m designating the present value, prediction of the future value y_{m+1} is defined only by the last known (i.e., present) value of variable X, y_m. Rogers and Williams (2000) described the Markov chain as modeling the process in a "memoryless" way: the variable "remembers" only its immediate preceding value and "forgets" the values far back in the past.

2.4.2.1. Discrete Markov Chains

The discrete Markov chain approach divides the property under observation into discrete intervals of a finite number n. The intervals are called states of the system. All possible states, f_i, form the state space of the problem, and the set of their probabilities form the state vector, F, of the size $n \times 1$.

$$F = \begin{bmatrix} f_1 \\ f_2 \\ \cdots \\ f_n \end{bmatrix} \tag{2.51}$$

When applied to simulation of the comminution processes, the Markov chain models the variations of the properties of the ground particles. If the amount of particles is large, f_i can be interpreted as the relative part (mass) of particles belonging to the i-th state (fraction). Therefore, the probabilities of the states f_i can be represented by the density probability function $f(x)$, or frequency PSD (Berthiaux et al., 2005).

The period of the process observation can also be divided into finite intervals of time, Δt, and the current time can be presented as a sequence of discrete values. The continuous flow of time is replaced with a sequence of positive integers, k, and thus, the variables of the Markov chain model (material PSD and time) become discrete.

$$t_k = \Delta t \cdot k\,, \tag{2.52}$$

where,

t_k – Discrete representation of time;

Δt – Duration of the transition;

k – Sequence of positive integer numbers (1, 2, 3, etc.).

Besides discretization of the continuous physical parameters, the described approach allows selection of the size of the "elementary volume" of the model, which determines accuracy of the simulation as well as the calculation time. The elementary volume can be derived from the experimental field data (Berthiaux, 2000).

2.4.2.2. Matrix of Transition Probabilities

During the k-th transition, between times t_k and t_{k+1}, the state vector F_k transforms into F_{k+1}. This means that the property of the particles transits from one interval to another and every transition has its own probability to occur. The correlation between F_k and F_{k+1} can be described by the matrix formula (Berthiaux et al., 2005):

$$F_{k+1} = PF_k \,, \tag{2.53}$$

where,

P – Matrix of transition probabilities.

Matrix P is the main operator of the Markov chain model. It contains transitional probabilities that determine the possibility of one individual state to transit into another.

$$P = \begin{bmatrix} P_{11} & P_{12} & \cdots & P_{1j} & \cdots & P_{1n} \\ P_{21} & P_{22} & \cdots & P_{2j} & \cdots & P_{2n} \\ \cdots & \cdots & \cdots & \cdots & \cdots & \cdots \\ P_{i1} & P_{i2} & \cdots & P_{ij} & \cdots & P_{in} \\ \cdots & \cdots & \cdots & \cdots & \cdots & \cdots \\ P_{n1} & P_{n2} & \cdots & P_{nj} & \cdots & P_{nn} \end{bmatrix} \tag{2.54}$$

The entry value, P_{ij}, of matrix P shows the probability of state j to transit into state i. From the inherent probabilistic nature of the matrix, its entries P_{ij} should satisfy two conditions (Mizonov et al., 2002; Berthiaux et al., 2005):

$$0 \le P_{ij} \le 1 \quad and \quad \sum_{i=1}^{n} P_{ij} = 1 \quad for \quad \forall j \tag{2.55}$$

If the transition matrix P is time independent and constant for all transitions, the successive use of Equation (2.53) will describe the process evolution starting from the initial state vector F_0 (Ching and Ng, 2006). This is the case of a linear Markov process that has a direct application in the simulation of grinding and can be presented as:

$$F_k = P^k F_0 \tag{2.56}$$

2.4.3. Control of Grinding Process

Process control is an essential part of the cement milling system. All new cement plants built today have a digital control system that provides all basic control operations through a computer interface. In most cases, new plants also acquire advanced control applications that enable automatic process control and analysis of the plant's operation in real time (Fuerstenau and Han, 2003).

Development of an effective control strategy requires a good knowledge of the dynamics of the milling circuit. The common approach in analysis tends to isolate different stages of the grinding process so that cause and effect can be clearly defined. However, the reality of cement production is that it involves a complex multivariable environment, where all the elements are interconnected (Kawatra, 2006). That is why a well formulated mathematical model is an essential tool in understanding the operation of the grinding circuit as a system.

The advantages attributed to automation include higher production rates and more efficient use of energy. In addition, the automated systems typically govern the manufacturing process with less variability than human operators, which results in tighter control and consistency of the final product quality (Bhatty et al., 2004).

An effective process control system consists of:

- Instrumentation
- Hardware peripherals
- Control strategy

The field instrumentation measures the process value, the strategy compares this value with the target value and orders the hardware peripherals to open or close the "valve" that affects the observed process signal. The field instrumentation and hardware peripherals components of the process control system are beyond the scope of this work. The following is a brief description of the types of the process control strategies.

The heart of any control strategy is the mathematical representation of the grinding circuit. In general, any of the mathematical models reviewed earlier can fulfill this task. The purpose of the control strategy is to determine what control variable to

change, in what direction (decrease or increase), and how much. The control strategies can be divided into three categories:

- Regulatory
- Supervisory
- Optimizing

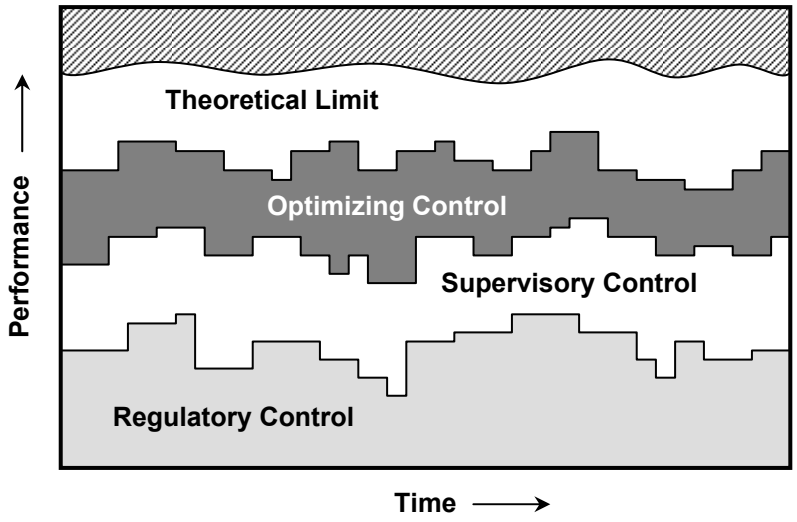

Figure 2.24. Types of Process Control (after Fuerstenau and Han, 2003).

Figure 2.24 illustrates hierarchy among the control strategies. The regulatory control strategies are most commonly aimed at stabilizing process inputs such as fresh feed rate. They rely on the feedback loops and proportional-integral-differential controllers measuring the process values in the field. The supervisory control strategies calculate set-points (targets) for the regulatory strategies in search of some process objective, for example, maintaining the specific surface area of the final product. The supervisory control strategy is the one that requires the mathematical model to calculate the size and direction of the adjustments to the set-points. The optimizing control strategies calculate process objectives for the supervisory strategies based on a combination of the economic and quality objective functions (see Fuerstenau and Han, 2003 for more details).

The early implementations of the supervisory strategies were formulated after, so-called, "crisp" rules in determining whether to change the set-point or not. These rules were designed to assess the operational conditions based on the strict, "true or false", Boolean logic (Kawatra, 2006). A more flexible approach was achieved with development of so called "fuzzy" logic. This introduced a notion of "degrees of truth". Fuzzy logic includes various states of truth between the extreme cases of truth. The result of comparison between two variables could now be not just strictly "0" (false) or "1" (true), but "0.27" (somewhat false).

Another supervisory approach was devised with the development of the neural network methodology. Based on the training that the neural network has received, the model calculates an anticipated error between the observed variable and its set-point. The strategy then adjusts the variable to eliminate the error.

While the supervisory strategies are quite common throughout the cement industry these days, the optimizing control strategies are of a rarity. The reason for this is that the relationships among the factors affecting the finish grinding process described in Figure 1.4 are yet to be determined. Knowing the relationships among the cement's performance characteristics, its fineness properties, process parameters of the circuit, and hardness of the clinker nodules, it would become possible to formulate both energy and fineness objectives for the grinding process and control steps towards reaching them.

The Markov chain theory will be employed next to develop a model for the finish grinding process operating in a closed circuit. The values of the model parameters will be identified using the field data collected at a pilot cement plant. Through the numeric simulation and analysis the relationships among the process factors given in Figure 1.4 will be revealed and the regulatory steps towards achieving the energy and quality objectives will be suggested.

3. DEVELOPMENT OF THE MARKOV CHAIN MODEL

Based on the basic concepts of the Markov chain theory described earlier, the matrices of grinding, classification, and closed circuit are derives below.

3.1. MATRIX OF GRINDING

Prior to deriving the grinding matrix, the state vectors, *F*, of all material flows within the circuit should be identified. The typical finish mill circuit and the sampling points of every major material flow are shown in Figure 3.1 (see section 2.2.3.1).

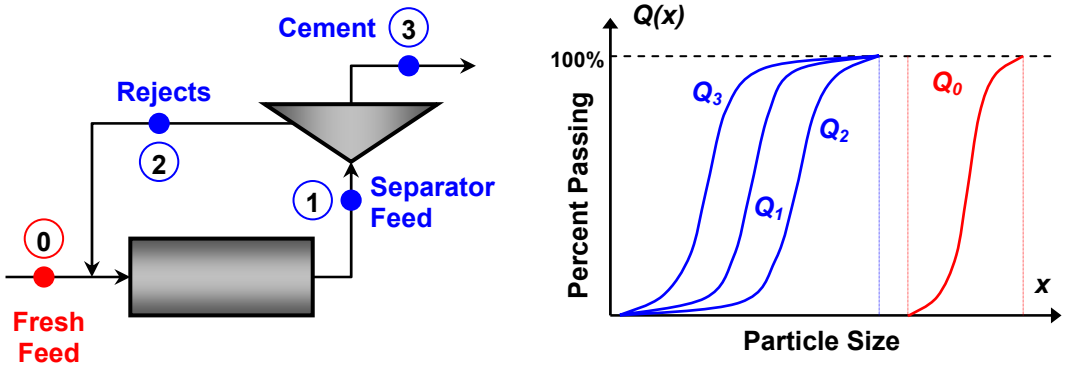

Figure 3.1. Typical Sampling Points of the Closed Milling Circuit.

The PSD of the fresh feed material is much coarser than those of the material flows surrounding the separator. In fact, the PSD of the fresh feed may not overlap with other PSD's in the circuit as schematically shown in Figure 3.1 using cumulative percent passing distributions. In addition, the three separator flows are fine enough to be subjected to the laser particle size analysis, whereas the PSD of the fresh feed material is usually obtained using a set of standard sieves.

The described effect leads to the differences in the sieve sizes used to define the PSD's in the grinding circuit. In order to convert all particle size distribution data to the same set of sieves, the computational sieves need to be introduced.

3.1.1. Set of Computational Sieves

The set of the computational sieves should cover the entire range of the particle sizes from the smallest in the final product to the largest in the fresh feed material. Because the difference between the largest and the smallest sizes may reach as much as 10^6-fold, the computational sieves should be determined using a geometric progression. The following expression fulfils this task well and covers the size range of interest in about 40 sieves:

$$xm_i = xm_{\min} + \gamma \cdot 2^{\frac{i-2}{2}} \quad for \quad i \geq 2, \tag{3.1}$$

where,

xm_i – Computational sieve sizes, µm;

$xm_{\min}$ – First computational sieve size (i = 1), µm;

i – Number of the sieve in the set starting with the smallest size;

γ – Arbitrary coefficient.

The measured particle size distributions should now be converted to the set of computational sieves. A linear interpolation of the cumulative distribution is used to recalculate the measured percentages passing to the new grid of the computational sieves as shown in Figure 3.2 and Equation (3.2).

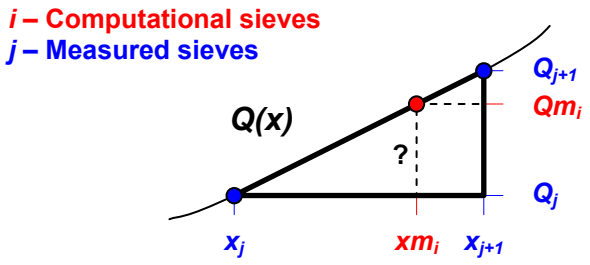

Figure 3.2. Conversion of the Measured PSD to the Set of Computational Sieves.

$$Qm_i = Q_j + \frac{xm_i - x_j}{x_{j+1} - x_j}\left(Q_{j+1} - Q_j\right), \tag{3.2}$$

where,

Qm – Cumulative percent passing in the computational sieves;

Q – Measured value of the cumulative percent passing;

x – Measured sieve sizes, μm.

To introduce the PSD data into the model, the cumulative distribution of the fresh feed, $Qm_0(xm)$, should be transformed into the differential form of the state vector, F_0. The state vector F_0 represents a discrete normalized particle size distribution of the fresh feed material with smaller particles having lower indices (see section 2.1.1.1).

$$F_0^{(i)} = Qm_0^{(i+1)} - Qm_0^{(i)}, \tag{3.3}$$

where,

i – Index within the set of computational sieves;

0 – Designation of the fresh feed flow.

Since only the computational set of sieves will be used in further derivations, the letter "*m*" will be omitted from the current designation of the computational sieves, "*xm*", and will read plainly "*x*".

3.1.2. Selection and Distribution Breakage Functions

The clinker particle may be broken into pieces with a certain probability to be subjected to a grinding force and then be fractured (Zhukov et al., 1993). After the particle was broken, it no longer belongs to the original fraction (source fraction) and its pieces are distributed among the fractions of a smaller size (recipient fractions). The amount of the ground portion and the way in which the ground particles are spread among the smaller size fractions are determined by the selection and distribution functions.

In order to employ the selection and distribution functions, two hypotheses about the grinding procedure in a tube ball mill need to be declared (Mizonov et al., 1997):

1. The breakage of fractions in the mixture occurs independently from one another.
2. The fracture energy is distributed over the feed fractions proportionally to their mass contents.

In the simulation of comminution processes, a selection function is used to describe the *rate* of a particle breakage. This function is the representation of the laws of grinding (see section 2.3.3) and ties together the size of a particle subjected to the grinding forces with the specific fracture energy required to produce the new surface. The selection function has a general formula of (Austin et al., 1981; Zhukov et al., 1993):

$$s(x) = \alpha \cdot \left(\frac{x}{x_{\max}} \right)^{\beta}, \tag{3.4}$$

where,

$s(x)$ – Selection as a function of the particle size, x, under load, 1/s;

$x_{\max}$ – Largest sieve of the computational sieve grid (x_n), μm;

α and β – Grinding constants from the numerical experiment.

Parameter α is proportional to the specific energy input and fracture toughness of the particle. Parameter β is closely related to parameter p in Equation (2.48) and corresponds to the governing grinding law. If the process follows the Rittinger's law of grinding, then $\beta = 1$; in case of the Bond's law, $\beta = 0.5$ (Zhukov and Mizonov, 1995). The selection function describes the rate of the grinding process and has a unit of 1/second. Multiplying the selection function, $s(x)$, by the duration of the observation period, Δt, defines the probability of a clinker particle to break.

It's important to examine how a single fraction, j, containing f_j portion of the total sample, responds to the selection and distribution functions (see Figure 3.3). Upon the action of the comminution forces, one part of fraction f_j is ground: ($s_j \Delta t$), and the other remains within the original fraction: ($1 - s_j \Delta t$). The ground material exits fraction j and enters fractions of smaller sizes with indices i, so that $i < j$. If the particles do not agglomerate, the ground material can not generate particles characterized by a particle size, for which $i > j$.

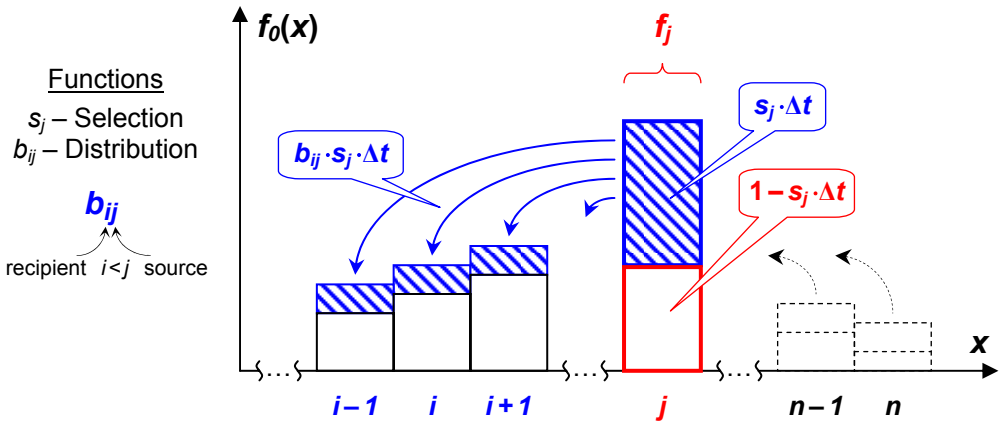

Figure 3.3. Selection and Distribution Breakage Functions.

The ground particles are spread among the smaller size fractions according to a law of distribution, reflected in parameter b_{ij}. Here, the first index, i, indicates the recipient fraction and the second one, j, denotes the source fraction. The portion of the ground material that transfers to the smaller fraction i is equal to ($b_{ij} \cdot s_j \Delta t$). The sum of parameters b_{ij} must be equal to 1, meaning that only exactly the amount of the ground portion of the initial fraction, f_j, may be distributed among the smaller size fractions:

$$\sum_{i=1}^{j-1} b_{ij} = 1 \tag{3.5}$$

In order to formulate the distribution function, the following experimentally supported assumption can be applied. It is expected that the pieces of the ground fraction f_j are distributed uniformly over the fractions of smaller sizes (Mizonov et al., 1997).

$$b_{ij} = \frac{dx_i}{x_j - x_{\min}}, \tag{3.6}$$

where,

dx_i – Width of the recipient fraction i, μm;

x_j – Size of the source fraction j, μm;

$x_{\min}$ – First computational sieve ($i, j = 1$), μm.

When considering simultaneous comminution of all fractions throughout the entire span of the sieve sizes, fraction f_j in addition to being subjected to grinding action also receives distributed material from the larger size fractions, i.e., fractions with $i > j$ all the way up to the largest computational sieve size, n. This is shown in Figure 3.3 by transition of the material from the fractions to the right side from fraction f_j along the dashed arrows.

3.1.3. Composition of Matrix of Grinding

Matrix of grinding, G, is a special case of the transition matrix, P. It is derived from the premise that the grinding procedure occurs by elementary steps representing breakage events (Berthiaux, 2000). One such event corresponds to a single transition of the Markov chain as described by Equation (2.53). A repetitive process of grinding complies with Equation (2.56), representing transitions of the state vector over a period of time. The elements of the matrix of grinding are determined using the selection and distribution breakage functions.

The matrix of grinding is defined by (Mejeoumov et al., 2005a):

$$G = \begin{bmatrix} 1 & b_{12}s_2\Delta t & b_{13}s_3\Delta t & \cdots & b_{1n}s_n\Delta t \\ 0 & 1-s_2\Delta t & b_{23}s_3\Delta t & \cdots & b_{2n}s_n\Delta t \\ 0 & 0 & 1-s_3\Delta t & \cdots & b_{3n}s_n\Delta t \\ \cdots & \cdots & \cdots & \cdots & \cdots \\ 0 & 0 & 0 & \cdots & 1-s_n\Delta t \end{bmatrix} \tag{3.7}$$

Matrix G is an upper triangular matrix. The diagonal entries define the probability values for the particles to remain within their original fractions. The particles in the smallest fraction do not break and their probability to remain within the fraction is 100% ($G_{11} = 1$). The entries in the upper corner of the matrix represent the distribution function and define the probability of particle transition from the source fraction (column of the matrix) into the recipient fraction (row). The entries of the bottom corner of the matrix are zeros assuming there is no agglomeration associated with the grinding process.

Similar to Equation (2.53), a single grinding event is given by:

$$[F_0]_{k+1} = [G][F_0]_k \tag{3.8}$$

Here, the subscript index inside the brackets designates the material flow (fresh feed), and the subscript index outside the brackets, k and k+1, refers to the transition of the state vector, F_0. By substituting (2.51) and (3.7) to Equation (3.8), the amount of the material in fraction i, resulting after a single transition, can be calculated as:

$$f_i^{(k+1)} = f_i^{(k)} - f_i^{(k)} s_i \Delta t + \sum_{j=i+1}^{n} f_j^{(k)} b_{ij} \cdot s_j \Delta t \tag{3.9}$$

In this formula, the first term is the original amount of the material in fraction i, the second term is the amount that left the fraction due to grinding, and the third term is the amount of the material that fraction i received from the larger size fractions due to their respective grinding and distribution of the material over the smaller size fractions.

Similar to Equation (2.56), the state vector defining the PSD of the material exiting the mill can be calculated using (3.8) (Mejeoumov et al., 2005a):

$$[F_1] = [F_0]_k = [G]^k [F_0]_0, \tag{3.10}$$

where,

$[F_1]$ – State vector of the separator feed flow;

$[F_0]_k$ – Fresh feed state vector after k-th transition;

$[G]^k$ – Result of k multiplications (transitions) of matrix of grinding;

$[F_0]_0$ – Initial state vector of the fresh feed.

Being proportional to time, the number of transitions, k, may be interpreted as the residence time in the tube ball mill. Indeed, the longer the material stays within the mill and the higher the number of transitions, the finer the resulting milling product.

3.1.4. Two-Dimensional Matrix of Grinding

In a more elaborate case, the matrix of grinding can also model the motion of the material along the axis of the tube ball mill. The resulting matrix represents two dimensions of the process of grinding: breakage of the particles and their physical movement from one spatial coordinate to another (Mizonov et al., 2004).

As a first approximation, the particle flow through the tube mill can be described as a one-dimensional process with a principal coordinate along the axis of the mill. According to the discrete Markov chain approach, the length of the mill can be presented as *m* spatial sections (cells) with the material in each section containing *n* number of size fractions. In this set-up, an arbitrary clinker particle residing within the mill can belong to one of the spatial sections and to one of the size fractions (see Figure 3.4).

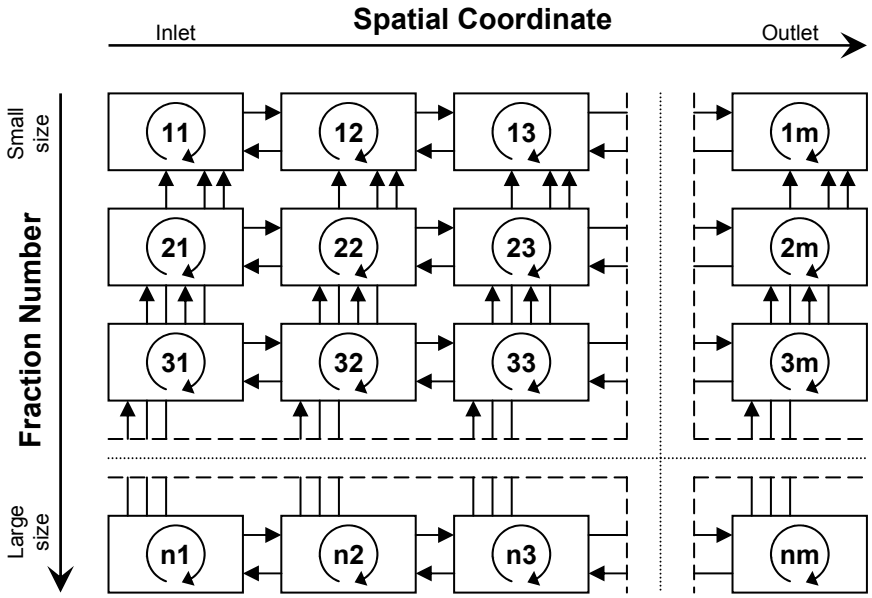

Figure 3.4. Two-Dimensional Cell Model of the Grinding Process (After Mizonov et al., 2004).

The set of cells shown in Figure 3.4 forms the state space of the process. It contains all possible outcomes of the particle transitions between the spatial sections and size fractions within the tube mill. While being ground, the clinker particle can travel between the neighboring cells or either remain in its original fraction or move to the fractions of a smaller size. The particle can occupy any of these states with a certain probability (Mejeoumov et al., 2005b).

Similar to the one-dimensional case, if the number of the particles is large the probability of each state can be defined by the relative mass of the particles occupying it.

The state matrix, *FF*, is based on the cell representation of the mill shown in Figure 3.4 and describes the set of probabilities for the particles to belong to a certain state:

$$FF = \begin{bmatrix} f_{11} & f_{12} & \cdots & f_{1m} \\ f_{21} & f_{22} & \cdots & f_{2m} \\ \cdots & \cdots & \cdots & \cdots \\ f_{n1} & f_{n2} & \cdots & f_{nm} \end{bmatrix} \tag{3.11}$$

Matrix *FF* is a rectangular matrix with $n \times m$ cells, where f_{ij} is the probability that the particle occupies the state in the *i*-th row (fraction) and *j*-th column (spatial section). Individual elements of the state matrix, *FF*, may be identified, for example, using the PSD results of the longitudinal sieve analysis of the tube ball mill. The transition matrix, *GG*, that governs the transformation of the state matrix, *FF*, over an elementary time period, Δt, has the following structure:

$$GG = \begin{bmatrix} G_{11} & T_{12} & 0 & \cdots & 0 \\ T_{21} & G_{22} & T_{23} & \cdots & 0 \\ 0 & T_{32} & G_{33} & \cdots & 0 \\ \cdots & \cdots & \cdots & \cdots & T_{(m-1)m} \\ 0 & 0 & 0 & \cdots & G_{mm} \end{bmatrix} \tag{3.12}$$

Matrix *GG* is a tridiagonal block matrix consisting of $m \times m$ blocks, or matrices. Its principal diagonal contains matrices *G*, defining transition probabilities within the columns of the state space shown in Figure 3.4. These matrices describe transitions of the particles among different size fractions within the same spatial cell of the mill (grinding). They have upper triangle form and are similar to those derived in Equation (3.7).

Matrices *T*, adjacent to the principal diagonal of matrix *GG*, describe forward (lower diagonal) and backward (upper diagonal) travel of the particles within the mill. During a single transition, Δt, the particles are allowed to travel only to the neighboring cell and only within the same size fraction, i.e., the same row of the state space.

Unfolded matrix *GG* has the size of $nm \times nm$ elements. Every column of matrix *GG* contains all probabilities for the permitted transitions of a single state within the

state space. Therefore, according to Equation (2.55), sum of the elements in every column of matrix *GG* should be equal to 1.

To use the state matrix, *FF*, with the matrix of transition probabilities, *GG*, matrix *FF* should be stacked into a state column vector.

$$FF^{S} = \left[f_{11} \ldots f_{n1} \quad f_{12} \ldots f_{n2} \quad \ldots \quad f_{1m} \ldots f_{nm} \right]^{T}, \tag{3.13}$$

where,

FF^S – State column vector of size $nm \times 1$.

Then, similarly to Equations (3.8) and (3.10) defined above, the single and repetitive transitions of the state column vector FF^S can be calculated, respectively, as (Mizonov et al., 2004; Mejeoumov et al., 2005a):

$$\left[FF^{S} \right]_{k+1} = \left[GG \right] \left[FF^{S} \right]_{k} \quad \text{, and} \tag{3.14}$$

$$\left[FF^{S} \right]_{k} = \left[GG \right]^{k} \left[FF^{S} \right]_{0}. \tag{3.15}$$

3.2. MATRIX OF CLASSIFICATION

Following the material flow path inside an actual grinding circuit, the state vector representing the material exiting the mill, F_1, is directed to the matrix of classification, which models division of the material into the fine and coarse fractions.

The dynamic separator of the closed mill circuit is represented by the diagonal matrix of classification, *C*, every element of which, C_i, shows the relative part of the fraction *i* that transits into the objective material flow of the classification (final product). The matrix of classification is a result of the discretization of the grade efficiency curve of the separator. Its size is determined by the number of elements (fractions) of the state vector: $n \times n$. The grade efficiency curve (an inverse of the Tromp curve) can be calculated using the measured PSD data of the separator streams using Equation (2.34). The GEC is then converted to the set of computational sieves using Equation (3.2) and, in a discrete form, term by term, assigned to the elements of the matrix of classification, *C*.

$$C = \begin{bmatrix} C_1 & 0 & \dots & 0 \\ 0 & C_2 & \dots & 0 \\ \dots & \dots & \dots & \dots \\ 0 & 0 & \dots & C_n \end{bmatrix} \tag{3.16}$$

If the particle size data of the separator is not available, an analytical description of the GEC is possible for calculating the matrix of classification. The following expression provides an adequate representation of the grade efficiency curve of the dynamic separator (Andreev et al., 2006; Mejeoumov et al., 2007a):

$$GEC = \frac{1}{1 + \left(\frac{x}{x_{50}} \right)^{\xi}}, \tag{3.17}$$

where,

x – Size of the fraction, μm;

x_{50} – Cut size, μm;

ξ – Calibration parameter.

The cut size, x_{50}, can be defined analytically for different types of separators. Its derivation is based on the physics of the separation process and involves consideration of laws of aerodynamics tying together the geometrical configuration of the separation zone, gas and rotor velocity, density of gas and classifying material, and kinematical viscosity of gas (Mejeoumov et al., 2007a).

Unlike grinding, the separation process is assumed to occur during a single transition of the Markov chain process. There are two material flows that result from the classification procedure. The particle size distributions for both of them, fine product, F_3, and rejected coarse material, F_2, are calculated using matrix C.

$$[F_3] = [C][F_1] \tag{3.18}$$

$$[F_2] = ([I] - [C])[F_1], \tag{3.19}$$

where,

I – Identity matrix, all diagonal elements of which equal 1.

Given Equations (3.10), (3.18) and (3.19), all state vectors of the closed milling circuit, F_1, F_2, and F_3, can be identified for the steady-state operation of the circuit using the state vector, F_0, which represents a continuous constant fresh feed.

3.3. MATRIX MODEL OF THE CLOSED GRINDING CIRCUIT

The matrix-based model for the entire milling circuit integrating the matrices of grinding and classification is presented below. Using the mass balance principle, the transition matrices of the separate pieces of equipment are incorporated in a single block matrix according to their respective functions and the material path within the circuit.

The approach was first derived by Mizonov et al. (1997) and then perfected by the same team of researches in a recent publication: Mizonov et al. (2005). The method can be applied to an arbitrary number of grinding and classification units operating in a circuit and, in fact, is not restricted to modeling only comminution processes.

3.3.1. Construction of the Circuit Matrix

Adding a new element to the closed grinding circuit in Figure 3.1 that absorbs the product particles leaving the separator will help to isolate all PSD's of the circuit, including the PSD of the final product. Also, and only in this section, the subscript indexation of the material flows between the mill and the separator will be slightly changed to facilitate construction of the model. The closed milling circuit with the new notation for the matrix model formulation is shown in Figure 3.5.

As it can be seen from the figure, the elements of the circuit are numbered in the following way: mill – 1, separator – 2, and the product collector – 3. The material flows represented by the state vectors, F, have the subscript indexation of the element of the circuit, to which they are directed. Therefore, the state vector of the material particle size distribution at the inlet of the mill is F_1, separator – F_2, and product collector – F_3. The state vector representing the fresh feed remains F_0.

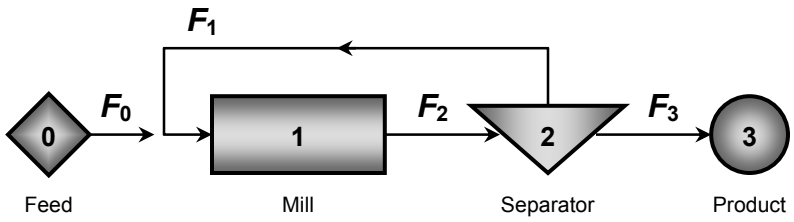

$$\mathbf{M} = \begin{bmatrix} \mathbf{0} & \mathbf{I - C} & \mathbf{0} \\ \mathbf{G} & \mathbf{0} & \mathbf{0} \\ \mathbf{0} & \mathbf{C} & \mathbf{0} \end{bmatrix}$$

Figure 3.5. Matrix Model of the Closed Grinding Circuit.

The circuit matrix, *M*, is constructed using a set of rules derived by Mizonov et al. (1997) for the circuits consisting of an arbitrary number of elements and configuration:

- Every column of the matrix *M* corresponds to an element of the circuit. The matrix of transition probabilities of an element is placed in that column.
- The matrix of transition probabilities of the mill, *G*, is placed in the row with the number of the element where the output of the mill is directed.
- The matrix of transition probabilities of the classifier, *C*, is placed in the row with the number of an element where the fine product of classification is directed, and the matrix (*I* – *C*) is placed in the row with the number of an element where the coarse product of classification is directed.

Similarly to other matrices of transition probabilities defined earlier, matrix *M* describes the particle transition from the source element of the circuit (column number) into the recipient element (row number).

$$M = \begin{bmatrix} 0 & I - C & 0 \\ G & 0 & 0 \\ 0 & C & 0 \end{bmatrix} \tag{3.20}$$

Matrix M is a block matrix with a number of blocks corresponding to the number of elements in the grinding circuit (3×3). The full size of the unfolded matrix M is defined by the number of elements of the circuit times the number of size fractions under consideration, i.e., ($3n \times 3n$) for the circuit shown in Figure 3.5. The last column of the matrix M contains only zero block matrices since the absorbed particles of the final product irrevocably leave the circuit.

3.3.2. Numerical Steady-State Solution

In order to use matrix M in the Markov chain calculations, an inclusive state vector containing all state vectors of all elements in the circuit should be constructed. Such an inclusive vector is achieved by stacking the state vectors of the elements into a column block vector (Mizonov et al., 2005).

$$F^{\mathrm{M}} = \begin{bmatrix} F_1 \\ F_2 \\ F_3 \end{bmatrix}, \tag{3.21}$$

where,

F^{M} – Column block state vector;

F_i – State vector of size $n \times 1$.

The state vector of the fresh feed, $F^{\mathrm{M}}{}_0$, is similar to vector F^{M} and contains mass fractions that are added to the circuit after every transition. However, for the circuit shown in Figure 3.5, it contains only one non-zero block vector out of three, which is given by Equation (3.3) and represents the size distribution vector F_0 of the fresh feed flow (Mizonov et al., 2005).

$$F_0^{\mathrm{M}} = \begin{bmatrix} F_0 \\ 0 \\ 0 \end{bmatrix} \tag{3.22}$$

To simplify the matrix iterations, the elementary transition time, Δt, should be chosen equal to the particle residence time in the mill. Then, the material flow inside the

mill can be presented as a perfect plug flow and all particles will be passing through the mill in one Markov chain transition. Since the residence time of the separator is normally much shorter than that of the mill, the same approach will apply to the particle transition through the separator (Mizonov et al., 2005).

For the selected transition period, Δt, and defined matrices G and C, matrix M can be constructed and used to calculate the successive evolution of the state vector F^{M} as (Mejeoumov et al., 2007b):

$$\left[F^{\mathrm{M}}\right]_{k+1} = \left[M\right]\left(\left[F^{\mathrm{M}}\right]_k + \left[F_0^{\mathrm{M}}\right]_k\right) \tag{3.23}$$

Equation (3.23) can be rewritten to reveal the entries of the matrices and show the inherent mass balance relationships.

$$\begin{bmatrix} F_1 \\ F_2 \\ F_3 \end{bmatrix}_{k+1} = \begin{bmatrix} 0 & I-C & 0 \\ G & 0 & 0 \\ 0 & C & 0 \end{bmatrix} \begin{bmatrix} F_1 + F_0 \\ F_2 \\ F_3 \end{bmatrix}_k = \begin{bmatrix} (I-C)F_2 \\ G\left(F_1 + F_0\right) \\ C \cdot F_2 \end{bmatrix}_k, \tag{3.24}$$

where,

F_0 – Fresh feed;

$F_1 = (I-C)F_2$ – Rejects; (3.25)

$F_2 = G\left(F_1 + F_0\right)$ – Separator feed; (3.26)

$F_3 = C \cdot F_2$ – Final product. (3.27)

Although with a slightly different notation, Equations (3.25)-(3.27) are identical to Equations (3.19), (3.8) and (3.18), respectively.

Successive iteration of Equation (3.24) rounds off the presented matrix model of the grinding circuit. For a continuous constant feed to the circuit, there is an asymptotic solution for the state vector F^{M} that describes particle size distributions in all material flows of the circuit: F_1, F_2, and F_3, for the given fresh feed F_0 (Mizonov et al., 2005).

Using the rate value of the fresh feed, B_0, the flow rate in the material stream entering the j-th element of the circuit can be found as:

$$B_j = B_0 \sum_{i=1}^{n} f_{ij} \ , \tag{3.28}$$

where,

B_j – Flow rate of the material stream into the j-th element;

f_{ij} – Relative mass size of the i-th fraction entering j-th circuit element;

n – Total number of size fractions in the computational set of sieves.

In addition to the numerical approach presented above, an analytical expression for a steady-state (asymptotic) solution of an absorbing Markov chain process is also available (Kemeny and Snell, 1960; Mizonov et al., 2005):

$$\left[F^{\mathrm{M}}\right]_{\infty} = \left(I - M\right)^{-1}\left[F_0^{\mathrm{M}}\right], \tag{3.29}$$

where,

$[F^{\mathrm{M}}]_{\infty}$ – Asymptotic state vector of all PSD's in the circuit.

The developed Markov chain model for a closed grinding circuit allows one to determine the particle size distributions and flow rates in all material streams of the circuit based on the PSD and flow rate of the fresh feed. The matrix notation is compact and relatively easy to implement using software such as MATLAB.

4. FIELD DATA COLLECTION AND ANALYSIS

Sampling and PSD analysis of the material flows within the grinding circuit is an integral part of identification of the Markov chain model for a particular process. Also, the analysis of the separator response to the changes in the rotor speed and air flow rate is important to model the behavior of the separator. The field experiment has been carried out and the material samples from different material flows were obtained for varying regimes of operation of the finish mill circuit.

4.1. FINISH GRINDING CIRCUIT AT THE PILOT PLANT

The finish mill circuit at the pilot plant is equipped with FLS two-compartment tube ball mill and FLS Sepax high efficiency separator. The specification data for the mill and separator and the diagram of the circuit are shown in Table 4.1 and Figure 4.1.

Table 4.1. Design Parameters of the Grinding Equipment at the Pilot Plant.

Tube Ball Mill		**Compartment**		**High Efficiency Separator**		
		1	**2**			
Outside Diameter	[m]	3.8		**Casing Diameter**	[m]	3.35
Outside Length	[m]	12.5		**Rotor Diameter**	[m]	1.69
L/D Ratio	[–]	3.29		**Rotor Height**	[m]	1.64
Internal Diameter	[m]	3.61	3.69	**D/H Ratio**	[–]	1.03
Internal Length	[m]	3.64	8.13	**Separator Motor**	[kW]	224
Filling Degree	[%]	28.4	35.0	**Separator Air Flow**	[m^3/h]	109,000
Charge Weight	[t]	47	142	**Fan Motor Power**	[kW]	296
Mill Motor Power	[kW]	2,611		**Cyclones (No. × Diam.)**	[m]	4 × 2.4
Mill Speed	[rpm]	17.2				
Relative Speed	[%]	79.3				
Mill Air Flow	[m^3/h]	39,700				
Fan Motor Power	[kW]	150				
Production Rate	[tph]	60*		* Design value		

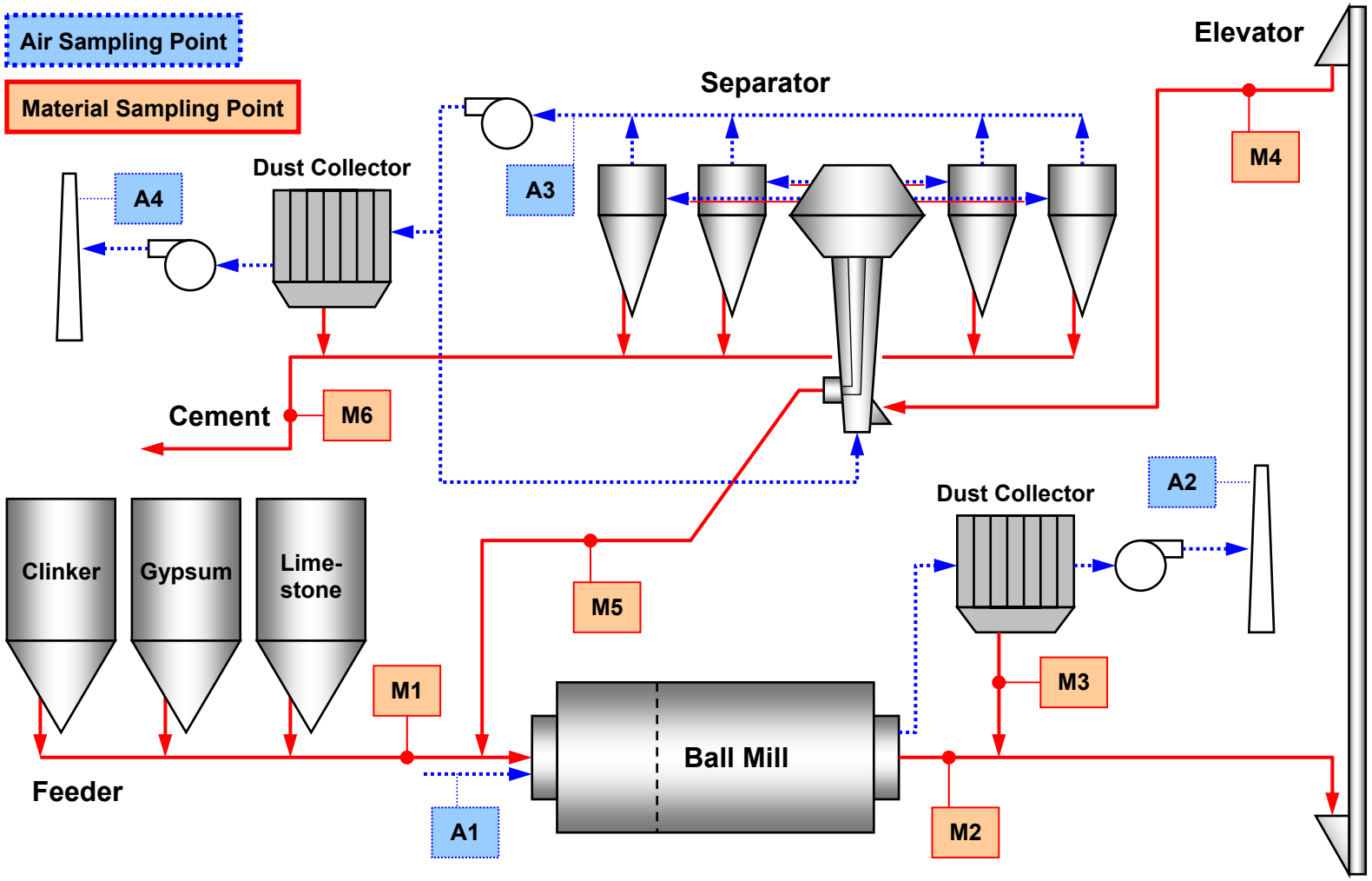

Figure 4.1. Actual Closed Milling Circuit at the Pilot Plant.

The solid red lines in Figure 4.1 represent the material flow, whereas the dotted blue lines show the air flow through the circuit. The material sampling locations M1, M4, M5, and M6 correspond to the fresh feed (F_0), separator feed (F_1), rejects flow (F_2), and final product (F_3) principal sampling points shown in Figure 3.1.

The material flow of an actual grinding circuit slightly differs from the simplified scheme of flow described in section 2.2.3. The air sweep through the equipment picks up some of the fine particles and causes minor branching of the material flow. Because of this, the air flows of the system are cleaned by means of dust collectors and the retrieved particles are returned back to the material streams.

A measured mixture of clinker, gypsum, and limestone (flow M1 in Figure 4.1) is fed into the mill along with the rejects flow from the high efficiency separator. At the mill discharge (M2), most of the ground particles are dropped into an air slide, which takes them to an elevator. However, a portion of very fine particles is picked up by the mill air sweep (A1) and carried out through the ventilation duct. The exhaust air (A2) is cleaned by the dust collector, and the reclaimed particles are delivered to the same bucket elevator via a screw conveyor (M3). The combined mill discharge is fed into the high efficiency separator through an air slide (M4).

The separator feed material is dropped into an upward blowing air stream inside the separator. The fine particles are removed from the separator to four cyclones along with the flow of hot gas. Inside the cyclones, the solid material is separated from the gas and dropped into an air slide, which takes the fine product to a cement cooler and then to the storage silos. After leaving the cyclones, the hot air (A3) is recirculated through a fan back into the system and reused by the separator. A small amount of the heated air is vented off through a dust collector, which cleans the recirculated air flow. The reclaimed material supplements the product stream directed to the cement coolers (M6).

The coarse material leaving the separator (M5) is returned to the mill's inlet for an additional cycle of grinding along with the fresh feed.

4.2. IN-SITU SAMPLING PROCEDURE

The two adjustable parameters of the separator are its rotor speed and air flow rate (see Table 2.6). With this, in order to analyze the performance of the finish mill circuit, the following on-site sampling procedure was carried out at the pilot cement plant.

- The separator material streams were sampled for three different separator speeds: nominal, increased, and decreased, for the constant air flow rate.
- The separator material streams were sampled for three different air flow rates: nominal, increased, and decreased, for the constant separator rotor speed.
- The material sample was obtained from the fresh feed conveyor belt.
- The data characterizing the process parameters of the finish milling circuit during the sampling procedure was registered.
- The process data historian was queried for an extended list of process parameters characterizing the milling circuit over a period of two years.

4.2.1. Experimental Design for Separator Sampling

To test the performance of the separator, three values of the separator rotor speed and three values of the separator air flow had to be defined as:

- Approaching the upper running limit,
- At the nominal running regime, and
- Close to the lower running limit.

For this, the process parameters characterizing the separator speed and air flow and their corresponding operating ranges had to be determined.

At the pilot plant, the separator rotor speed is measured directly and the rotor speed signal is readily available for handling. However, the air flow measurements are not automated and must be performed manually when the flow value is desired. Therefore, an indirect indication of the air flow rate had to be utilized to estimate its process range. In order to increase or decrease the air flow through the separator, the plant operator changes the speed set-point of the separator fan. Depending on the physical conditions of the in-situ air, the fan's motor requires a certain amount of energy

to deliver the required fan speed. The fan power value is stored in the PDH system and available for assessing the working range of the separator fan.

The PDH system was queried for the one-hour average process values for the separator rotor speed and separator fan kilowatts during a month immediately preceding the sampling procedure. The obtained data was filtered to retain only those values that represented a stable operation of the finish mill circuit and thus exhibited low values of standard deviation (STD) for the measured parameters. The filtering criteria included:

- Same type of cement being produced
- Blaine value between 320 and 450 m^2/kg (target: 380 m^2/kg)
- Rejects rate between 50 and 210 tph
- Rejects rate STD < 20.0 tph
- Fresh feed rate STD < 5.0 tph
- Separator rotor speed STD < 3.0 rpm

The scattered data points covering the process range of the separator rotor speed and fan power values are shown in Figure 4.2.

The separator rotor speeds ranged between 196.4 and 229.4 rpm. Such a relatively wide range of the separator speeds was caused by a similar wide range of the filtering conditions with respect to the Blaine values (320-450 m^2/kg). In an attempt to minimize the disruption to the normal operation of the pilot plant and because the Blaine value is so sensitive to the separator speed changes, the high and low testing speeds were moved 15% within the observed operational range as shown in Figure 4.2(a). The testing program was thus aligned to cause the least possible impact on the quality of the produced cement.

The power of the separator fan ranged between 189.6 and 241.5 kW. However, it should be emphasized that the plant operator changes the air flow rate by altering the fan speed. The adjustable fan speed set-point is expressed as a percentage of the maximum allowable fan speed. The high and low fan speed values had to be estimated in order to cover the observed operational range of the separator fan power of 190-245 kW as shown in Figure 4.2(b).

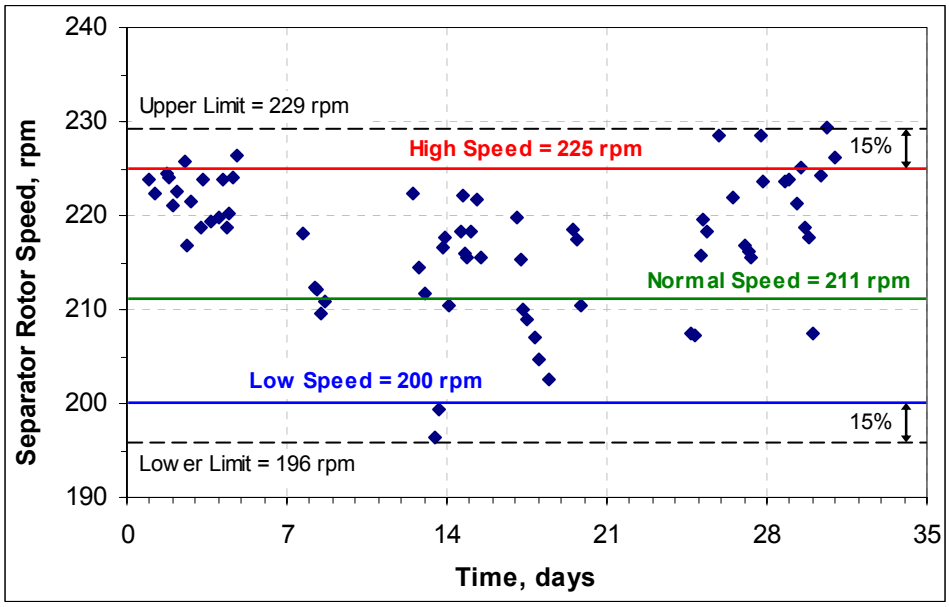

(a)

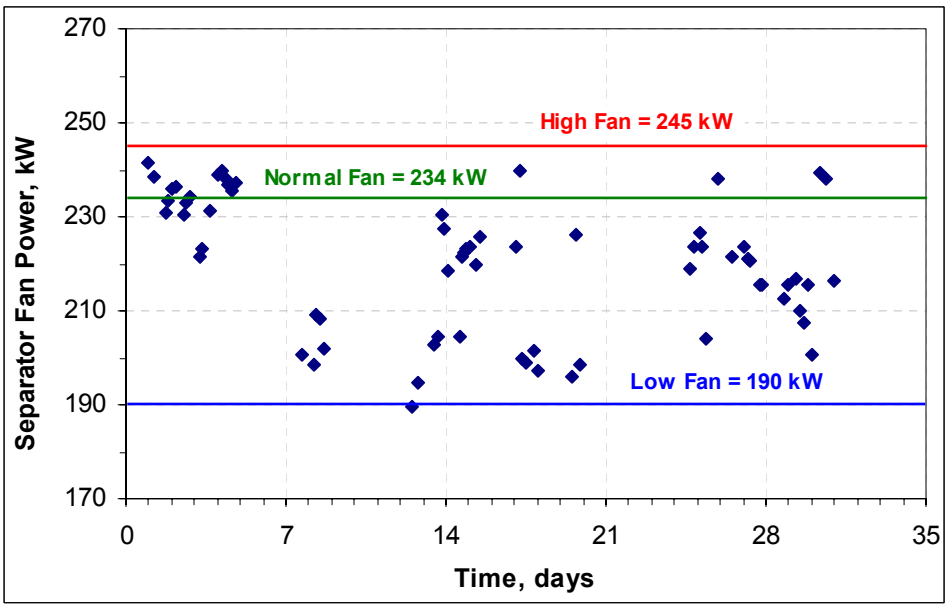

(b)

Figure 4.2. Process Ranges of the Separator Parameters
(a – Rotor Speed; b – Fan Power).

The normal (nominal) separator speed and fan power were accepted at the values that provided the target Blaine fineness (380 m^2/kg) of the produced cement on the day of testing, prior to any changes.

To characterize the separator performance for a given pair of separator rotor speed and air flow rate, the three separator material streams (feed, rejects, and fines) had to be sampled and analyzed. The experimental design establishing the total amount of the required samples and showing the testing values of the separator rotor speed and the fan percent speed is given in Table 4.2. The middle cell of Table 4.2 represents the nominal operation of the separator on both days of testing (6 total samples) before any changes had been applied.

Table 4.2. Experimental Design for the Separator Performance Analysis.

No. of Samples Per Test		Separator Rotor Speed		
		200 rpm	211 rpm	225 rpm
Separator Fan Speed (Fan Power)	88% (190 kW)	–	3	–
	94% (234 kW)	3	3 + 3	3
	96% (245 kW)	–	3	–

The experimental design has a cross-like structure since the separator was tested for the response to a change in only one parameter at a time while the other one was kept at a nominal value. The regimes represented by the corner cells were not tested as they represent the deviation of both separator speed and air flow from their normal regime values. Omitting these regimes lessened the adverse impact on the final product quality due to the disturbance caused by the testing procedure and also reduced the total amount of the required samples.

4.2.2. Sampling Procedure

The testing procedure for the finish mill circuit was accomplished in two days. During the first day, the separator rotor speed was adjusted while the air flow was kept constant. On the second day, the separator rotor speed was kept at the nominal value and the speed of the separator fan was altered. After each adjustment, the finish mill circuit was allowed to stabilize for about 3 hours, following which, the separator material streams were sampled, the required air flow was measured, and the current process data was recorded from the PDH system.

4.2.2.1. Sampling of the Separator Material Streams

The material samples of the three separator streams were collected following ASTM C 183: "Standard Practice for Sampling and the Amount of Testing of Hydraulic Cement". Generally, this method is not intended as a sampling procedure for quality control purposes during manufacturing and was used only as a guideline.

The samples were obtained through the access gates in the air slides containing the corresponding material flows. During the sampling procedure, a metal cup-like scoop with a long handle specifically designed for this purpose was utilized. The scoop was inserted into the material duct in such a way that the sample representative of the entire cross-section of the duct was obtained.

All samples were placed in individual plastic bags and labeled with the inherent information: source of the sample (the original material flow), current separator rotor speed, and separator fan speed. The sample bags containing the final product were sent to the quality control lab at the plant for the air permeability analysis (Blaine test) as per ASTM C 204 "Fineness of Hydraulic Cement by Air Permeability Apparatus". At the end of the testing procedure, all bags, including those sent earlier to the control lab, were mailed to Texas A&M University for the laser PSD analysis.

4.2.2.2. Fresh Feed Conveyor Belt Sampling

At the end of the first day of testing, the finish mill was stopped and the sample of the fresh feed mixture was taken from the conveyor belt leading to the mill's inlet. A

two-foot long strip of material was gathered from the belt, shoveled into the buckets, and sent to the control lab for the sieve analysis. The individual samples of clinker, limestone, and gypsum constituting the fresh feed mixture were obtained and tested for the sieve gradation as well.

4.2.2.3. Air Flow Measurements

For each separator fan speed, an actual air flow rate was calculated using the measurements at the air sampling location A3, which represents the combined air flow passing through the separator (see Figure 4.1). The basic formula for the air flow rate is:

$$Q = 3600 \cdot v \cdot A, \tag{4.1}$$

where,

Q – Air flow rate at actual conditions, m^3/h;

v – Gas velocity in the air duct, m/s;

A – Cross-sectional area of the air duct, m^2.

The cross-sectional area of the round air duct is defined by:

$$A = \frac{\pi \cdot D^2}{4}, \tag{4.2}$$

where,

D – Diameter of the round air duct, m.

The air velocity, v, can be determined from the pressure measurements inside the air duct by means of a Pitot tube (e.g., S-tube). Bernoulli's principle suggests there are three types of the pressures associated with the gas flow (Wang et al., 2004):

$$P_t = P_d + P_s, \tag{4.3}$$

where,

P_t – Total pressure, Pa;

P_d – Dynamic (velocity) pressure, Pa;

P_s – Static pressure, Pa.

Inserting the Pitot tube through the air sampling porthole provided readings of the total, P_t, and static, P_s, pressures inside the air duct (see Figure 4.3). A low dust content of the air flow is required for an accurate reading using the Pitot tube. The measurements should be taken at a straight section of the air duct and relatively far from any possible flow disturbances caused by the cornering or branching of the duct.

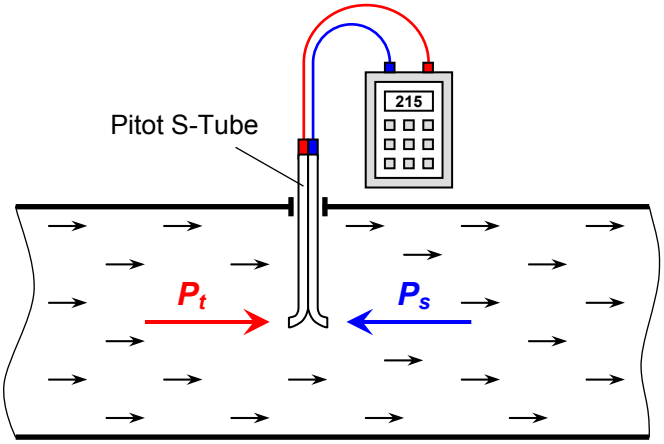

Figure 4.3. Duct Pressure Measurement Using Pitot S-Tube.

The dynamic constituent in Bernoulli's formula, P_d, can be expressed through the measured total and static pressures using Equation (4.3). The dynamic pressure is caused by the particle kinetics and defined as (Wang et al., 2004):

$$P_d = \rho \frac{v^2}{2}, \tag{4.4}$$

where,

ρ – Density of the gas, kg/m^3;

v – Gas velocity, m/s.

From (4.4), the gas velocity measured using the S-type Pitot tube is given by:

$$v = K\sqrt{\frac{2 \cdot P_d}{\rho}}, \tag{4.5}$$

where,

K – Calibration factor of the S-type Pitot tube (0.8-0.85).

The velocity profile of the air flow is seldom uniform throughout the cross-section of the duct. To achieve an accurate flow rate, the cross-section of the duct is divided into a number of equal areas. The dynamic pressure, P_d, is then measured in each area and the average velocity is calculated using the average dynamic pressure.

Figure 4.4 illustrates a round air duct divided into 4 equal areas so that 8 measurements of the dynamic pressure are taken along two orthogonal diameters in the center of each ring segment.

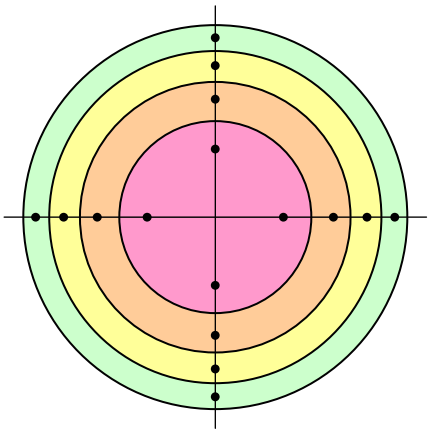

Figure 4.4. Traverse Points for Pressure Measurements in a Round Duct.

The density of air at ambient conditions, ρ, can be calculated using the ideal gas law and the value of the air density at *standard conditions*.

It is essential to explicitly state the standard reference conditions of temperature and pressure, when dealing with the gas properties or volumetric gas flow rate (Wang et al., 2004). Here and later on, the standard (or normal) conditions are defined as:

- Temperature of 273.15 K (0°C)
- Pressure of 101,325 Pa (1 atmosphere of absolute pressure at sea level)

Using the ideal gas law, the air density, ρ, can be found as (McElroy, 2002):

$$\rho = \rho_N \frac{T_0}{T_{gas}} \cdot \frac{P_{gas}}{P_0}, \tag{4.6}$$

where,

ρ_N – Normal air density at standard conditions, kg/Nm^3;

T_0 – Normal temperature of 273.15 K;

P_0 – Normal pressure of 101,325 Pa;

T_{gas} – Actual temperature of gas, K;

P_{gas} – Actual pressure of gas, Pa.

The normal density of air, ρ_N, can be defined using a molar mass approach:

$$\rho_N = \frac{M_{air}}{V_m}, \tag{4.7}$$

where,

M_{air} – Molar mass of the air, kg/k-mole;

V_m – Standard molar volume at normal conditions of 22.414 Nm^3/k-mol.

The molar mass of air, M_{air}, can be found as a weighted molar mass of the gases constituting the air (McElroy, 2002):

$$M_{air} = \sum_i C_i \cdot M_i, \tag{4.8}$$

where,

C_i – Concentration of the individual gas i, fraction or percent;

M_i – Molar mass of an individual constituent gas i, kg/k-mole.

Molar masses of the most common gases constituting the air are:

- M_{O2} = 32 kg/k-mole
- M_{CO2} = 44 kg/k-mole
- M_{N2} = 28 kg/k-mole

The value of the actual air temperature in Equation (4.6), T_{gas}, is obtained from the direct measurement of the temperature in the air duct. The actual pressure of air, P_{gas}, is determined from the following expression (McElroy, 2002):

$$P_{gas} = P_{atm} + P_s \,, \tag{4.9}$$

where,

P_{atm} – Atmospheric pressure at the sampling site, Pa;

P_s – Static pressure defined in Equation (4.3), Pa.

Atmospheric pressure, P_{atm}, is a function of the sampling site elevation above the sea level and can be calculated using the barometric formula (McElroy, 2002):

$$P_{atm} = P_0 \left(\frac{T_{ref} - L \cdot h}{T_{ref}} \right)^{\frac{g \cdot M_{air}}{R \cdot L}} \,, \tag{4.10}$$

where,

P_0 – Normal pressure at sea level of 101,325 Pa;

T_{ref} – Reference temperature for this formula of 288.15 K (15°C);

L – Standard temperature decrease rate of 0.0065 K/m;

h – Elevation of the site above the sea level, but below 11 km, m;

R – Universal gas constant of 8.3145×10^3 N·m/(k-mol·K);

g – Gravitational constant of 9.80665 m/s^2;

M_{air} – Molar mass of air defined in Equation (4.8), kg/k-mol.

With all parameters defined, the air flow rate at actual conditions, Q, is found using Equation (4.1). However, to compare the air flows at different actual conditions, the air flow, Q, should be reduced to standard conditions using the ideal gas law:

$$Q_N = Q \frac{T_0}{T_{gas}} \cdot \frac{P_{gas}}{P_0} \,, \tag{4.11}$$

where,

Q_N – Air flow at standard (normal) conditions, Nm^3/h.

4.2.2.4. Process Data Sampling

For each pair of the separator rotor speed and air flow rate, after the grinding system had stabilized, the exact time of sampling was determined and the process values of the key circuit parameters at that time were recorded from the PDH system. The process data is summarized in Table 4.3 and includes the cement Blaine surface results obtained at the quality control lab of the pilot plant.

Table 4.3. Process Data Pertaining to the Material Sampling Procedure.

Time	Separator Speed		Sep. Fan Speed	Air Flow		Fresh Feed			Rejects	Mill Motor	Sep. Fan Motor	Lab Blaine
						Total	Gyp	LS				
24h	rpm		%	Nm^3/h		tph	%	%	tph	kW	kW	m^2/kg
Day 1 – Variable Separator Rotor Speed												
10:45	224.9	**Hi**	94.4	–	–	77.7	4.8	3.4	185.2	2307	226.6	428
14:20	211.4	**Ok**	94.2	92,760	Ok	84.1	4.8	3.5	192.9	2365	233.3	383
17:45	200.0	**Lo**	94.3	–	–	86.9	4.8	3.5	187.2	2365	235.5	373
Day 2 – Variable Separator Air Flow Rate												
10:30	211.4	Ok	94.4	90,320	**Ok**	85.6	4.7	5.0	191.3	2321	234.0	378
13:30	211.2	Ok	96.1	99,220	**Hi**	85.3	4.7	4.8	196.0	2326	245.7	398*
16:40	210.9	Ok	88.2	88,070	**Lo**	79.7	4.7	4.7	190.2	2376	186.9	426

* Inconsistent with the testing conditions.

The increased and decreased values of the separator rotor speed and air flow in the table above are designated as "Hi" and "Lo", respectively; the nominal values of the separator parameters are denoted "Ok". Air flow is calculated for the standard conditions.

The lab Blaine results of Day 1 experiment are in line with the testing conditions: the measured specific surface of the final product is higher for the higher separator speeds. Day 2, however, unexpectedly presented an inconsistency: the highest rate of the separator air flow did not yield the lowest Blaine value.

The PDH system was also queried for the process data covering the preceding two years of operation of the finish mill circuit.

4.3. LABORATORY TESTING AND DATA ANALYSIS

This section describes analysis of the PSD data of all material flows, response of the separator's Tromp curve to the varying operating regimes, and process data pertaining to the times of material sampling.

4.3.1. Cement Density Test

The cement density value is required for calculating the specific surface value of the cement using the measured PSD data and Equation (2.21). The densities of the material samples, originating from the final product streams during different operating regimes, were determined using ASTM C 188 "Standard test method for density of hydraulic cement". The density value of each cement sample was calculated as the ratio of the displaced volume of kerosene in Le Chatelier flask by a cement sample of known mass: see Equation (2.3) and Figure 4.5.

Figure 4.5. Test Set-Up for the Cement Density Determination.

The density of the tested samples averaged at 3,054.9 kg/m^3 with a standard deviation of 9.2 kg/m^3 and a 95% confidence interval of 3,054.9 ± 9.7 kg/m^3.

4.3.2. Sieve Analysis of the Fresh Feed Mix

The fresh feed mix and its ingredients obtained from the feed conveyor belts were tested for the particle size distribution first. The fresh feed samples were subjected to the sieve analysis procedure described in section 2.1.1.1 since the particle sizes of the feed materials are beyond the measuring range of the laser analyzer. The individual sieve gradations of clinker, gypsum, limestone as well as the total mix are shown in Figure 4.6.

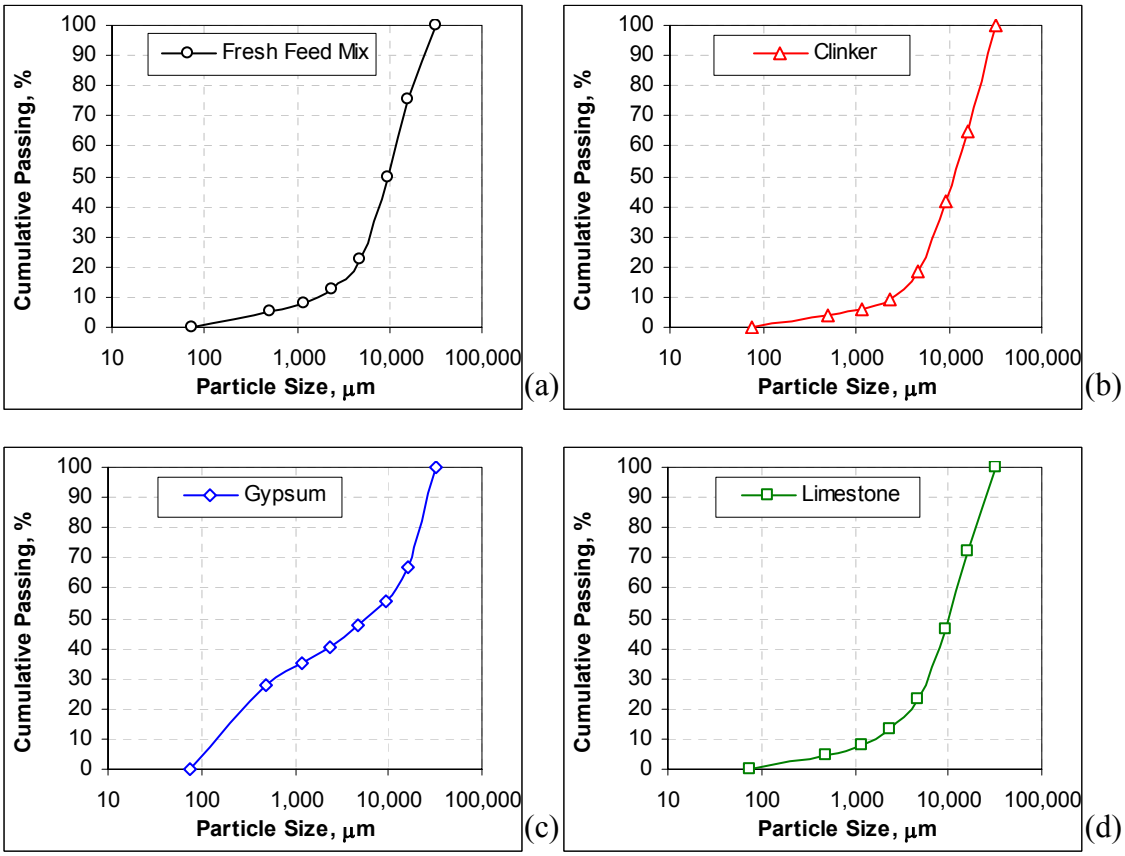

Figure 4.6. Sieve Analysis of the Fresh Feed Materials
(a – Total Mix; b – Clinker; c – Gypsum; d – Limestone).

4.3.3. Sample Preparation for the Laser PSD Analysis

The particle size distribution testing of the separator samples was carried out at Texas A&M University using Horiba Laser Scattering Particle Size Analyzer LA-910 shown in Figure 4.7.

Figure 4.7. Horiba Laser Scattering Particle Size Distribution Analyzer LA-910.

The sample bags were sent from the pilot plant to the Texas A&M University McNew laboratory via a mailing service, which implies that the postal package was subjected to impacts and vibrations of various levels. As a result, the larger and thus heavier particles in each individual bag might have migrated towards the bottom of the bag, whereas the lighter particles might have surfaced at the top of the sample. In order to prepare a representative sample for the PSD analysis, each plastic bag was thoroughly mixed and subjected to a conical quartering procedure so as to reduce the sample to the size required for testing.

Horiba LA-910 analyzer carries out measurements of the particles in a diluted state. A proper selection of the dispersing medium is an essential step towards achieving

the accurate reproducible measurements. It is important that the dispersant properly wets the sample, but does not instigate any agglomeration, dissolving, swelling, or chemical reaction as these processes induce volumetric changes of the sample particles.

The most common dispersing liquid, water, could not be used in this study since cement actively reacts with water. A 95% (190 proof) ethanol solution provides an inert environment for the cement particles and was selected as a dispersion medium.

It is also important to thoroughly disperse the sample particles in the liquid medium. The accuracy of the measurement may be compromised if the dispersion of the sample in the optical cell is uneven or the particles start to agglomerate. To promote the dispersion of the cement particles in the solution, the dispersed sample was continuously agitated in the sample cup, irradiated with ultrasonic vibrations for 3 minutes, and circulated through the optical cell during the entire measurement procedure.

The scattering laser beam of the analyzer may sense some background data during the measurements. These include foreign dust particles that may occur inside the optical cell. To eliminate this error, a background reading of the dispersant liquid alone is taken before a new sample measurement is performed and subtracted from the scattering light data characterizing the liquid bearing the sample.

In order to verify the reproducibility and impartiality of the PSD analysis, three material specimens were tested from each plastic bag and, once dispersed, three PSD measurements were performed on each specimen. An average PSD data of the sample was then used to characterize the source material flow.

4.3.4. Particle Size Distribution and Tromp Curve Results

The illustration of the cement PSD along with its Rosin-Rammler representation was shown earlier in Figure 2.3. The PSD's of the three separator streams were shown in Figure 2.15. In fact, these figures displayed the PSD data of the material samples collected during the first day of testing for the "Normal Speed – Normal Air" regime. The full PSD data of all analyzed samples are provided in Appendix A of the dissertation. The parametric representation of the measured particle size distributions is summarized in Table 4.4 and will be utilized in analysis of all PSD results.

Table 4.4. PSD, Rosin-Rammler, and Tromp Curve Parameters Results.

Testing Regime		PSD Curve			Rosin-Rammler		Tromp Curve			Blaine	
Sep. Speed	Air Flow	Mean	Median	Pass. 45 µm	n	d_0	x_{50}	x_{75}/x_{25}	By-pass	ASTM C 204	PSD
–	–	µm	µm	%	–	µm	µm	–	%	m^2/kg	m^2/kg
Day 1 – Variable Separator Rotor Speed											
Hi	Ok	17.66	14.81	94.89	1.066	17.7	32.01	1.781	6.70	428	393
Ok	Ok	18.30	15.48	94.44	1.075	18.3	32.96	1.775	9.22	383	380
Lo	Ok	19.84	16.31	92.16	1.072	20.2	38.69	1.732	6.32	373	351
Day 2 – Variable Separator Air Flow Rate											
Ok	Hi	17.75*	14.86*	94.88*	1.089	18.0*	30.65	1.698	9.81	398*	377*
Ok	Ok	19.15	16.06	93.25	1.072	19.3	35.54	1.803	7.77	378	365
Ok	Lo	17.37	14.71	95.49	1.080	17.5	34.25	1.754	7.33	426	390

* Inconsistent with the testing conditions.

The calculation of all parameters presented in Table 4.4 was introduced in the earlier sections of the dissertation. The Rosin-Rammler distribution parameters were determined for particle sizes larger than 1 µm to avoid the deflection of the Rosin-Rammler fitting curve from the straight line as shown in Figure 2.3(a).

The graphical representation of the PSD's of the cement products is given in Figure 4.8, (a) and (b). The first figure demonstrates the superposed cement PSD's, which resulted from the first day of testing (variable separator speed), whereas the second figure shows the PSD's for the variable separator air flow testing.

The PSD data of all three separator streams (feed, rejects, and fines) were used to construct the Tromp curves shown in Figure 4.9, (a) and (b). Similarly, the two figures display a response of the separator Tromp curve to the changes in the separator rotor speed and air flow during the two days of testing.

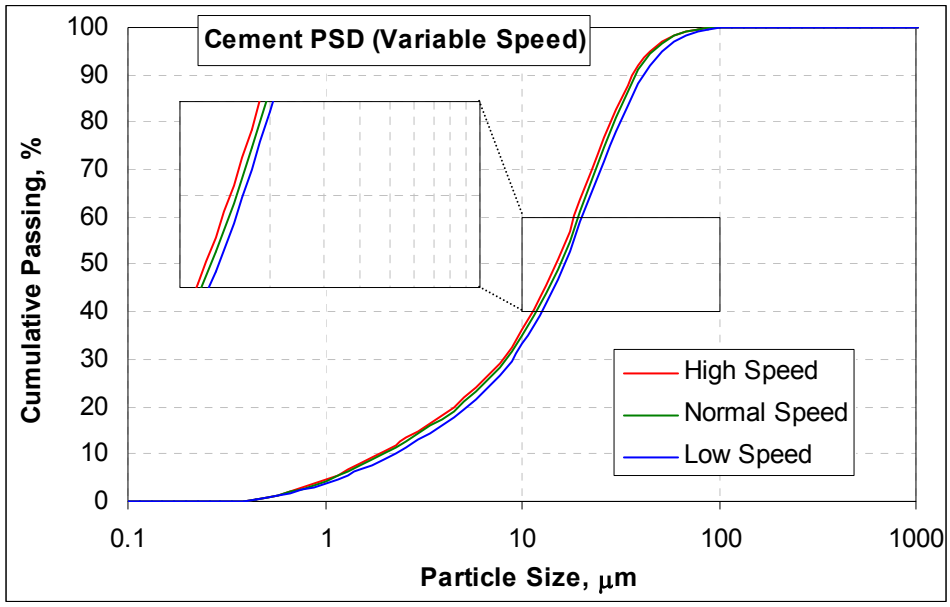

(a)

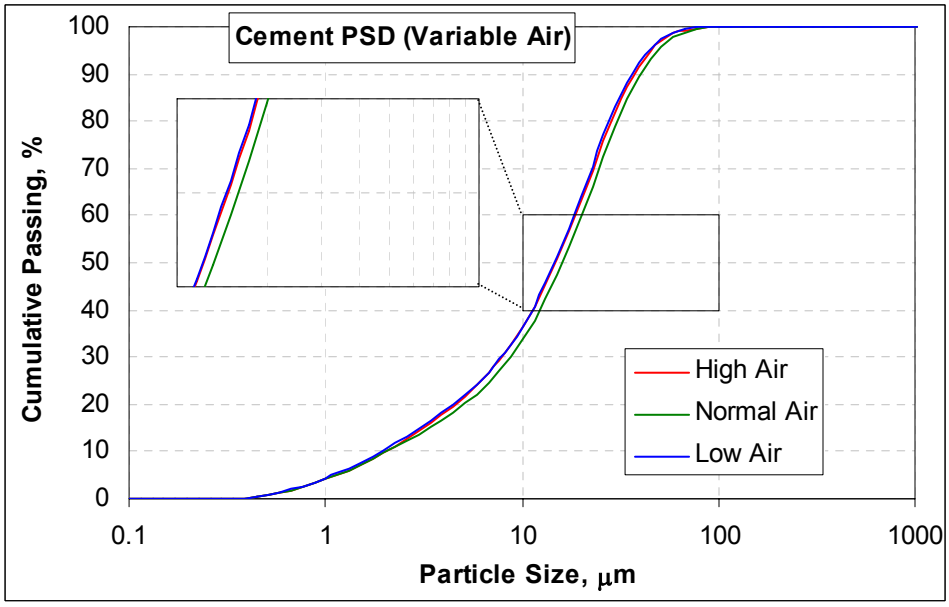

(b)

Figure 4.8. Final Product PSD's in Different Testing Regimes
(a – Variable Separator Speed; b – Variable Separator Air Flow).

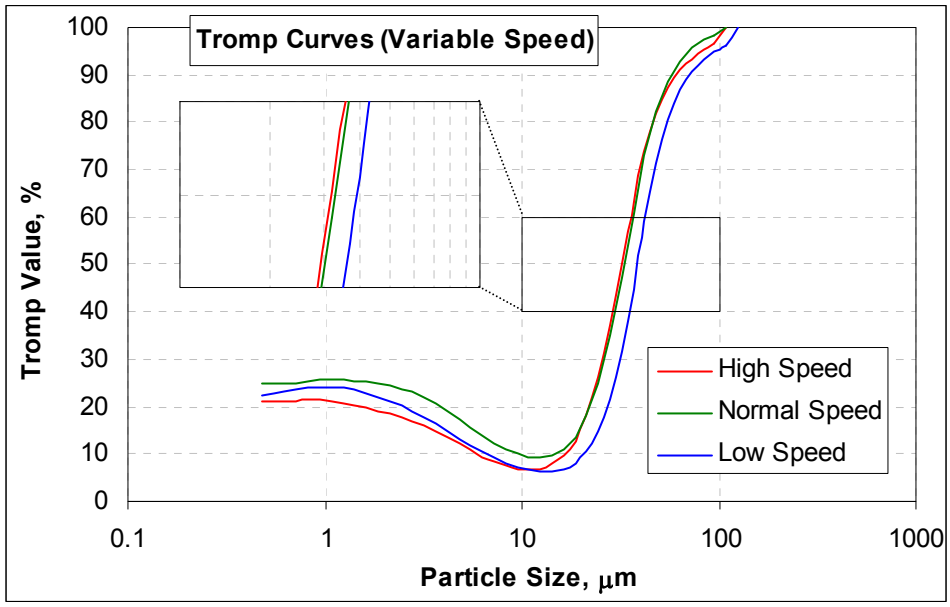

(a)

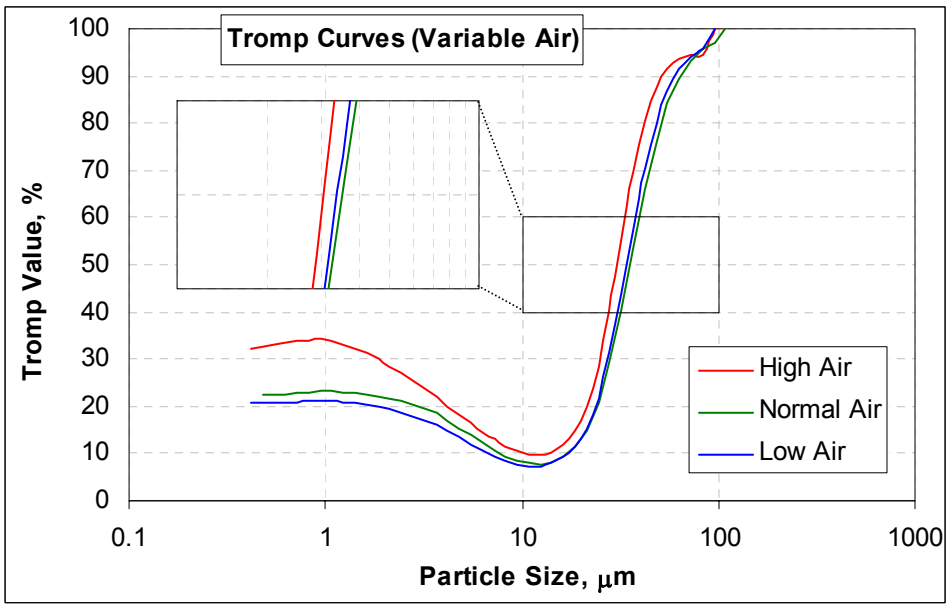

(b)

Figure 4.9. Separator Tromp Curves in Different Testing Regimes (a – Variable Separator Speed; b – Variable Separator Air Flow).

4.3.5. Analysis of the Test Results

The mean and median sizes of the cement PSD curve, its 45 μm percent passing value, size factor of the Rosin-Rammler distribution, d_0, measured and calculated Blaine surface values are all indicators of the material's fineness. The calculated values of these parameters are generally consistent with the testing conditions (see Table 4.4). That is, since a higher separator rotor speed rejects more coarse particles, it yields a higher fineness of the final product. The higher fineness entails lower values of the size distribution parameters and higher values of the 45 μm percent passing and material's specific surface area.

The inconsistencies incurred during of the second day testing, however, have been confirmed by the PSD analysis of the cement samples. For a nearly constant separator rotor speed (see Table 4.3), the high value of the air flow rate was expected to generate the coarsest final product of the second day and demonstrate the highest values of the PSD parameters along with the lowest Blaine and 45 μm percent passing values. The nominal and low air flow rates, with regard to one another, produced cement finenesses that were in line with expectations.

Analysis of the Tromp curve pertaining to the Normal Speed – High Air regime of the separator (red line) reveals a prominent fish-hook effect: see Figure 4.9(b). The left side of the Tromp curve rises as high as 34.2%, which suggests significant agglomeration of the very fine particles in the classification zone of the separator.

As established earlier, the Tromp curve defines the probability of a particle of a certain size to be rejected to the coarse stream of the separator. If the operating conditions favor producing a finer cement, the Tromp curve shifts to the left towards the smaller particle sizes. The effect of the high separator speed and high air flow on the fineness of the product is exactly the opposite. Since, in principle, the higher separator speed yields finer cement and the higher air flow coarser cement, the higher separator speed should shift the Tromp curve to the left (lower x_{50}), whereas the higher air flow rate to the right (higher x_{50}). Thus, the Normal Speed – High Air Tromp curve was supposed to be to the most right in Figure 4.9(b). Despite that, it is to the most left.

Clearly, the high air flow through the classification zone of the separator has affected the separation process and caused prominent agglomeration of the very fine particles. In order to better understand this observed phenomenon, the matter should be closely investigated in the future. The results of the second day testing will be used for identification of the Markov chain model only as a reference.

Analysis of the Rosin-Rammler parameters of the final product PSD's reveals that the shape factor, *n*, changes only marginally between 1.066 and 1.089 throughout the testing program (see Table 4.4), with slightly higher values demonstrated by the samples collected during the separator air flow adjustments of Day 2. The determined Tromp curve parameters suggest good performance characteristics of the separator with the bypass value between 6.3 and 9.8% and sharpness of separation between 1.698 and 1.803 instead of the expected value of 2.0 or more (Bhatty et al., 2004).

While exhibiting narrow operational ranges, both variable speed and air flow sampling results form the test space of the separator at the pilot plant. The range between the median sizes of the cement PSD curves was only 1.5 μm wide for the variable speed test and 1.35 μm wide for the variable air flow test; whereas, the cut size values of the Tromp curves spanned 6.7 μm and 4.9 μm, respectively (see Table 4.4). Although in a relatively narrow range, the variable separator speed test revealed a definite relationship between the separator rotor speed and the fineness characteristics of the final product. In order to provide a larger operational space, the circuit sampling should be repeated for a wider range of values of the tested separator parameters.

Extra care should be exercised when comparing the ASTM-measured and PSD-calculated specific surface area values. Being in line with the rest of the fineness parameters, the ASTM-measured results are consistently higher than the PSD-calculated values. There are certain sources of variability associated with both measuring methods, and, perhaps, the most significant one is due to the human factor intrinsic to both techniques (see the following section).

The obtained PSD and Tromp curve data will be utilized for identification of the Markov chain model.

4.4. SOURCES OF ERROR

Due to the strong empirical nature of the sampling procedure, there are several sources of error associated with collecting, selecting, and testing the material samples. At least two major sources can be easily identified as:

1. Sampling error, and
2. Measurement error.

Each source can be divided into several aspects. The sampling error includes:

- Non-simultaneous sampling of the material streams
- Extracting a possibly non-representative material sample from the air slide
- Obtaining a non-representative specimen for testing from the sample bag

The material samples were collected from the sampling points sequentially, i.e., one after the other. Even though the grinding circuit was considered stable during the sampling procedure, minor fluctuations within the circuit may have altered the characteristics of the material streams.

Due to the nature of the scooping technique, a bias in sampling the material streams is inevitable. Depending on how deep the scoop is inserted into the material duct and for how long it is left in the duct, the sampling results will vary. For this reason, each plastic bag was loaded with several scoops of the extracted material in attempt to reduce the variability due to the scoop sampling.

During the delivery process, the sampling bags were subjected to vibrations and impacts that might have caused segregation of the material fractions in the bags. Without thoroughly mixing and quartering the sample bag, the extracted specimen may not be representative of the original source adding its share to the overall sampling error.

The measurement error includes the following aspects:

- Use of a low quality dispersing liquid
- Insufficient dispersion of the sample in the measuring cell
- Background particles in the measuring cell
- Instrumental error of the analyzer: random particle shape, discrete size grid, etc.

First of all, different dispersing liquids have different refractive indices, which should be accounted for in the course of measurement. Secondly, the liquid should possess sufficient dispersing characteristics with respect to the material being tested. Finally, the highly volatile ethanol liquid may not be absolutely inert to the cement and may cause a minor degree of the material hydration. Without proper dispersion, the particles may start to agglomerate in the optical cell which will skew the test results.

Dust particles and occasional air bubbles may occur inside the optical cell and add to the background noise of the measured diffraction image. The background reading should be taken to minimize this measurement error.

As it was described in section 2.1.1.1, the laser scattering analyzer assumes all particles to be spherical. The actual shapes of the tested cement particles may differ causing the representation of elongated particles as spherical ones. Sufficient dispersion of the sample particles ensuring their random orientation inside the optical cell will minimize this error.

The particle distribution of the cement material is a continuous function of the particle size. Confining particles of a similar but not identical size into fractions imposes an error associated with the discretization of the PSD test results.

Every measurement device is characterized by a certain level of precision and the Horiba analyzer is not an exception. Timely calibrations using standard size samples and proper maintenance will help to tune and preserve the analyzer in a workable state.

During all sampling and testing procedures, proper measures were taken in an effort to minimize these errors.

In order to further assess the variability of the test results due to the scoop sampling technique and due to the human factor in measuring the laboratory Blaine value, a minor diversion from the original experimental design was made. For this, a total of 10 samples were extracted from the separator's final product stream during the first day of sampling for the "Normal Speed – Normal Air" test regime. The sample bags were brought to the quality control lab, and two different experienced technicians were asked to independently perform Blaine analyses on the cement samples as per ASTM C 204.

Furthermore, it was requested that each sample bag be tested twice by each technician. The results of this experiment are presented in Table 4.5.

Table 4.5. Variability of the Blaine Measurements as per ASTM C 204.

Sample No.	Technician 1		Technician 2		m^2/kg	
	Blaine 1	Blaine 2	Blaine 1	Blaine 2	Average	STD
1	388	383	378	381	**382.5**	**4.20**
2	383	383	378	376	**380.0**	**3.56**
3	391	386	352	381	**377.5**	**17.48**
4	400	400	382	382	**391.0**	**10.39**
5	391	393	390	382	**389.0**	**4.83**
6	396	398	374	374	**385.5**	**13.30**
7	407	407	388	388	**397.5**	**10.97**
8	400	398	386	386	**392.5**	**7.55**
9	386	383	370	374	**378.3**	**7.50**
10	378	373	376	374	**375.3**	**2.22**
Average	**391.2**		**378.6**			
STD	**9.43**		**8.41**			
Average	**384.9**					
STD	**10.88**					

Since the variability of the Blaine results were caused by both the duct sampling and the Blaine measurement errors, the average and standard deviation values were calculated for each material sample (rows) and each technician (columns) in Table 4.5.

The highest standard deviation between the results obtained by two technicians reached 17.5 m^2/kg with an average value of 377.5 m^2/kg for the sample bag No. 3. The first technician yielded a slightly higher standard deviation performing the Blaine tests (9.4 m^2/kg) compared to that of the second technician (8.4 m^2/kg).

The control strategy implemented at the pilot cement plant attempts to maintain the Blaine value of the final product within 380 ± 5 m^2/kg. However, the results above

show that the laboratory Blaine test may produce results ranging ±19.5 m^2/kg (±5.2%) around the average value of 377.5 m^2/kg (bag No. 3).

With a lab technician measuring only one cement sample and only one time every 2 to 4 hours, the lab Blaine results should be applied to the process adjustments in a very sensible manner. As far as maintaining the Blaine objectives in the finish mill control strategy, a reliable value for the Blaine value is crucial in delivering the required quality of the final product.

In order to eliminate the human component of the error in determining the Blaine value of the final product, the specific surface value of the cement samples calculated based on the measured PSD data and Equation (2.21) was used in further derivations.

5. NUMERICAL SIMULATION AND ANALYSIS

The Markov chain model was constructed and the analysis of the finish mill grinding circuit was performed using the MATLAB software. This computer program favors matrix algebra (MAT – Matrix and LAB – Laboratory) and therefore facilitates matrix operations within the proposed model. The matrices of grinding and classification derived above and the obtained data from the sampling procedure at the pilot plant allow the identification of the Markov chain model parameters for the grinding process, specifically for the examined finish mill circuit.

5.1. MODEL IDENTIFICATION

The collected data for the nominal regime, observed during the first day of testing and characterized by "Normal Speed – Normal Air" operation of the separator, was used to identify the parameters of the Markov chain model.

The input variables of the model were:

- $Q_1(x)$, $Q_2(x)$, $Q_3(x)$, and $Q_0(x)$ – Particle size distributions in the cumulative percent passing form describing the separator streams and fresh feed mixture;
- B_0 – Rate of the fresh feed to the entire circuit.

The set of computational sieves was calculated using Equation (3.1), and all particle size distributions of the circuit including the grade efficiency curve of the separator were converted to this set of sieves via Equation (3.2). The full range of particle sizes from the fresh feed (coarse material) to the final product (fine material) was covered using 42 computational sieves. To enable the population (fraction) balance calculations of the model, the cumulative PSD of the fresh feed was converted to the differential form using Equation (3.3).

The elements of the matrix of grinding, G, were calculated as per Equation (3.7). The selection breakage function was determined using Equation (3.4), whereas the distribution function was modified from its form presented in Equation (3.6) to account for the attrition of the clinker particles inside the mill.

As it was described in section 2.2.1.1, the comminution of particles in the second compartment of the tube mill is based on the shear-friction forces. These forces are not likely to break the clinker particle into parts of comparable size; they will rather shave the dust-like pieces off of the particle's surface. In terms of the particle transition between the size fractions, this means that even a very large particle has a substantial probability of producing a product-sized particle when subjected to attrition (Zhukov et al., 2005).

The effects of the shear-friction forces were included in the model by introducing the step distribution breakage function shown in Figure 5.1. The number of the recipient fractions accounting for attrition, q, and the probability of the particle transition into these fractions, p, were treated as the model identification parameters. Within each step of the breakage function, the calculation of the distribution parameter, b_{ij}, for each size fraction followed Equation (3.6). This arrangement guaranties that each fraction, no matter how large or small its size, will deliver a p portion of its ground particles into the dust group, i.e., into fractions less than x_q.

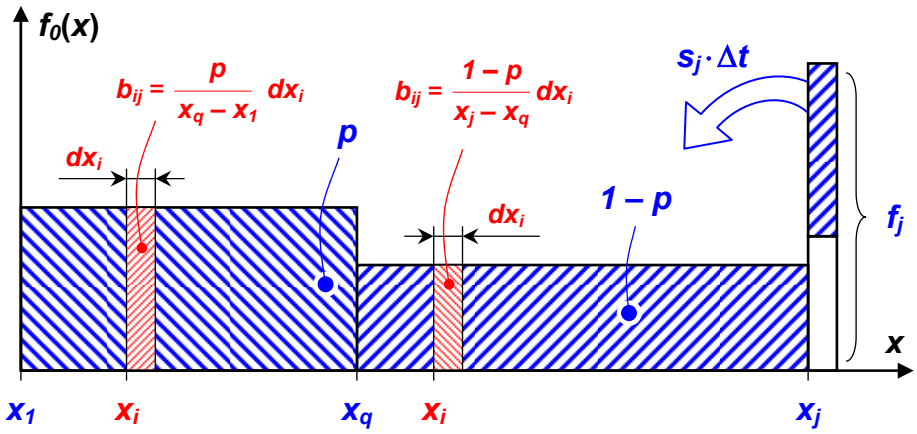

Figure 5.1. Step Distribution Breakage Function.

The elements of the classification matrix, C, were calculated using the values of the grade efficiency curve of the separator as per Equation (2.34). With the matrix of classification defined via measured PSD data, the identification of the model is reduced to determining the following parameters, characterizing the grinding matrix, G:

- Duration of the elementary time interval, Δt, defined in Equation (2.52);
- Coefficients of the selection function α and β in Equation (3.4);
- Coefficients of the step distribution function q and p introduced via Figure 5.1;
- Number of elementary cells of the mill representing its residence time, k;
- Reference throughput rate, B_R, required to scale the matrix of grinding to the observed throughput rate of the actual tube ball mill.

Rewriting Equation (3.10) and applying the reference throughput rate, B_R, the transitions of particles during grinding in the mill can be described as:

$$[F_1] = \left([G]^k\right)^{\frac{B_R}{B_1}} [F_0], \tag{5.1}$$

where,

G – Matrix of grinding;

k – Number of elementary Markov cells inside the mill;

F_0 – State vector of the fresh feed;

F_1 – State vector of the separator feed;

B_R – Reference throughput of the mill, tph;

B_1 – Model-calculated throughput of the mill, tph.

In the initial trial, the identification parameters were assigned arbitrary values. Since there is no accumulation of material inside the grinding circuit, the fresh feed rate, B_0, must be equal to the final product rate, B_3. With this, the model iterations were executed solving the system of mass balance Equations (3.24) until the following stopping criterion was satisfied:

$$\frac{|B_3 - B_0|}{B_0} < \varepsilon, \tag{5.2}$$

where,

B_0 – Measured fresh feed rate of the grinding circuit, tph;

B_3 – Model-calculated final product rate, tph;

ε – Tolerance level (0.0001) for the difference between B_0 and B_3.

All model-calculated material flow rates (B_1, B_2, and B_3) were determined using Equation (3.28). The number of iterations required to satisfy the stopping criterion in Equation (5.2) was recorded and employed as a measure of convergence of the model.

After the initial trial, the iterations of the model were repeated in search for the best identification parameters of the model. The Monte Carlo method was utilized as the search engine, whereas the best solution was estimated using the Least Square Method, which compared the calculated PSD's of the separator streams with the measured ones:

$$Error = \sum_{i=1}^{3} \sum_{j=1}^{n} \left[f_i^{(c)}\left(x_j\right) - f_i^{(m)}\left(x_j\right) \right]^2 , \tag{5.3}$$

where,

i – Number of the current material flow;

j – Number of the current size fraction;

$f_i^{(c)}\left(x_j\right)$ – Calculated fraction content of size x_j in the i-th flow;

$f_i^{(m)}\left(x_j\right)$ – Measured fraction content of size x_j in the i-th flow.

The set of parameters yielding the minimal error, as per Equation (5.3), represented the Markov chain model parameters identified for the finish mill grinding circuit running at the "Normal Speed – Normal Air" (NSNA) conditions. The specific surface area of the final product was determined via Equation (2.21) for both the model-calculated and measured particle size distributions. The specific surface results were compared and used as an additional verification criterion for identification of the Markov chain model.

The measured and calculated particle size distributions of the three separator flows along with the GEC are shown in Figure 5.2. In two text columns, the figure also presents the identified model parameters. The specific surface area and 45-μm sieve percent passing values determined using the measured PSD data of the final product are shown in red color below the model-calculated parameters.

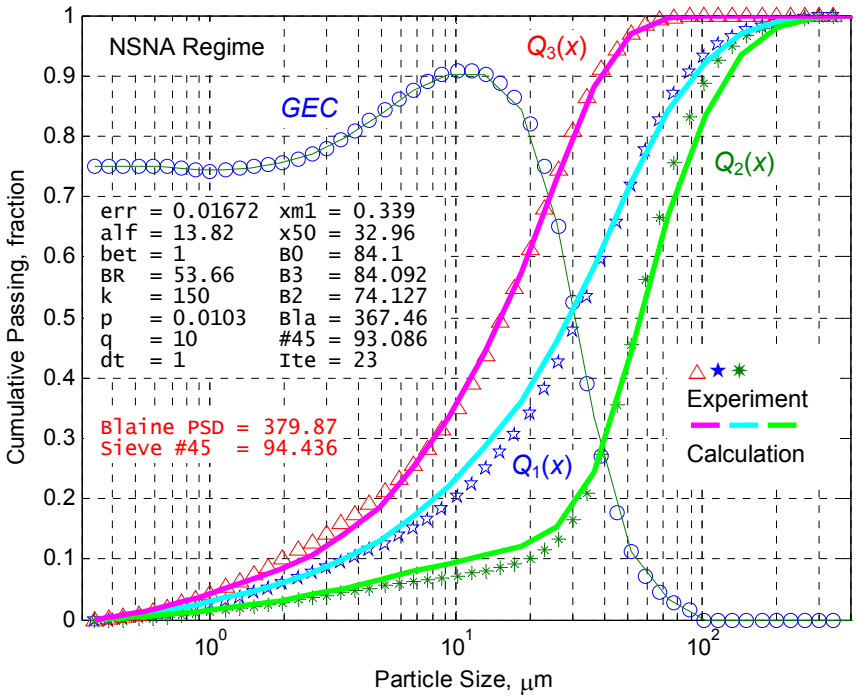

Figure 5.2. Identification of the Markov Chain Model Parameters.

The abbreviated notations shown in the two test columns in the figure above stand for the following model-calculated parameters:

- err – Calculated least square error
- alf – α of the selection function
- bet – β of the selection function
- BR – Reference throughput rate
- k – Number of grinding cells
- p – Step distribution function, p
- q – Step distribution function, q
- dt – Elementary time interval, Δt
- xm1 – First computational sieve
- x50 – Cut size of the GEC
- B0 – Experimental feed rate, B_0
- B3 – Calculated product rate, B_3
- B2 – Calculated rejects rate, B_2
- Bla – Product specific surface area
- #45 – Product 45 μm sieve value
- Ite – Iterations till convergence

As seen from the data shown in Figure 5.2, the modeled process favored Rittinger's law of grinding and thus resulted in the selection function coefficient $\beta = 1$ (see section 3.1.2). The number of fractions, q, receiving the dust particles due to the attrition effects inside the tube mill was found to be equal to 10. The probability of the

material transfer from any fraction lager than q = 10 into the dust size fractions within a single transition was determined as p = 1.03%. The first computational sieve was matched with the first measured sieve, defined by the grid of sieves of the laser particle size analyzer, that had zero cumulative passing values in all three PSD's of the separator material streams. The calculated regime required 23 iterations to achieve the product flow rate within 0.01% of the fresh feed rate, which asserted a rapid convergence of the proposed model. The fastest convergence was reached at k = 150 grinding cells of the tube mill. The model-defined specific surface area of 367.5 m^2/kg and 45-μm sieve passing of 93.1% were used as the reference values in further regime simulations. The elementary time interval, Δt, was preset for all calculations at one second.

With these parameters, the rest of the tested regimes were identified as well using the method of least square differences between the measured and calculated particle size distributions of the separator flows as per Equation (5.3). Requiring between 14 and 23 iterations, the model exhibited fast calculation convergence for all tested regimes and generated graphs similar to the one shown in Figure 5.2 for the NSNA regime.

Table 5.1. Model-Calculated Specific Surface Area vs. Measured Values.

Testing Regime		Specific Surface Area, m^2/kg		
Separator Speed	Air Flow	ASTM C 204	PSD Measured	Model Calculated
Hi	Ok	428	393	372
Ok	Ok	383	380	367
Lo	Ok	373	351	358
Ok	Hi	398	377	364
Ok	Ok	378	365	361
Ok	Lo	426	390	369

The specific surface values derived from the model-calculated size distributions of the final product were consistent with the corresponding testing conditions. It should be noted, however, that these model-calculated specific surface values fell well below

the laser PSD-measured values and even more so with respect to the ASTM-measured values (see Table 5.1). It becomes evident that the use of the specific surface area as the identification parameter should be limited due to the high variability of the results obtained from different estimation methods.

The derived parameters identified the Markov chain model for the plant specific grinding process and were held constant during the simulation calculations of various operational regimes presented next. The full-length MATLAB code of the model for the "Normal Speed – Normal Air" regime is presented in Appendix B of the dissertation.

5.2. IDEAL GRADE EFFICIENCY CURVE

An ideal separator allows all particles smaller than the cut size of the separator to become the final product and sends all particles larger than the cut size into the rejects material stream (section 2.2.2.2). Although physically impossible, this is the most desired property for any industrial separator to have as the efficiency of such a separator is 100%. This means that none of the coarse particles become the final product and none of the fine particles escapes to the rejects stream. Consequently, the grade efficiency curve values of the ideal separator are equal to 1 for all fractions less than x_{50} and 0 for fractions larger than x_{50}.

Using the identified Markov chain model, the ideal grade efficiency curve can be simulated and analyzed. Figure 5.3 shows how the particle size distributions for the NSNA operating regime would look like if the separator was ideal.

If the separator was ideal, the entire PSD of the final product, $Q_3(x)$, would lie below the cut size of the separator, x_{50} = 32.96 μm, whereas the PSD of the rejected material, $Q_2(x)$, would be situated above the cut size. Since all the particles of the final product would be finer than 32.96 μm, the 45-μm sieve passing value would be 100% and the specific surface area of the product would increase from 367.5 m^2/kg of the real classification conditions (Figure 5.2) to 376.5 m^2/kg of the ideal ones (Figure 5.3).

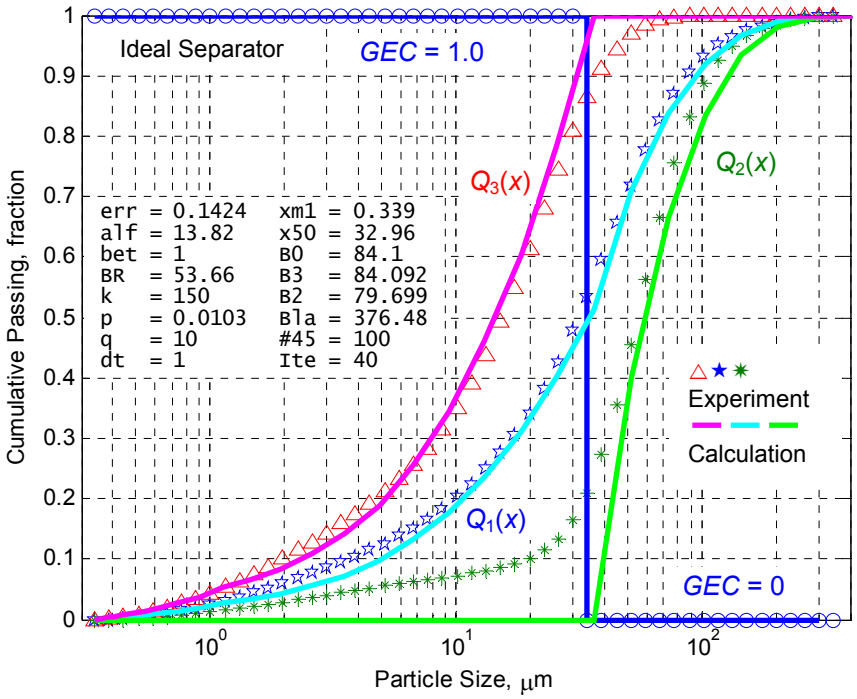

Figure 5.3. Simulation of the Ideal Classification.

The increase of the product's fineness level was anticipated due to the following characteristic features of the ideal GEC (or ideal Tromp curve):

- Zero bypass
- Lack of the "fish-hook" effect
- Unit sharpness of separation

Zero bypass and absence of the "fish-hook" effect in the ideal GEC entail that no agglomeration of the fine particles takes place in the classification zone and all of them are sent to the final product stream, thus increasing the fineness level of the product. The unity sharpness of separation suggests that the cut size of the separator, x_{50}, is an absolute value, at which the fine and coarse particles are ideally divided into two corresponding streams.

5.3. PARAMETRIC RESPONSE OF THE CIRCUIT

After reviewing the process parameters of the closed milling circuit presented in Table 2.6, it becomes apparent that the only parameters that can be directly adjusted by the plant operator are:

- Separator rotor speed,
- Separator air flow, and
- Fresh feed rate.

The rest of the parameters are measured in the field and can be influenced only indirectly by virtue of the cause-effect chain reactions to the change in the magnitude of the manipulated parameters. Therefore, the analysis of the response of the circuit to the changes in the manipulated parameters is a critical step towards understanding the circuit's dynamics.

The fresh feed rate is an input parameter of the Markov chain model and is readily available for analysis. On the other hand, both separator rotor speed and air flow changes were reported to have linear relationships with the cut size of the grade efficiency curve (Benzer et al., 2001). This permits simulation of the alterations in both separator speed and air flow by shifting horizontally the cut size value of the GEC.

5.3.1. Response to the Fresh Feed Adjustments

Using the model parameters identified in section 5.1, the finish mill circuit was calculated for several fresh feed input values. All other parameters of the model were kept constant. The calculated particle size distributions are shown in Figure 5.4 along with the specific surface area and Rosin-Rammler *n*-values defined for the PSD of the final product.

With the fresh feed rate increasing, all particle size distributions shifted to the right toward the larger particle sizes. Because of the shift, the specific surface area of the product dropped for the higher fresh feed rates and its PSD became wider resulting in lower values of the Rosin-Rammler shape factor, *n* – see Figure 5.5 (a) and (b).

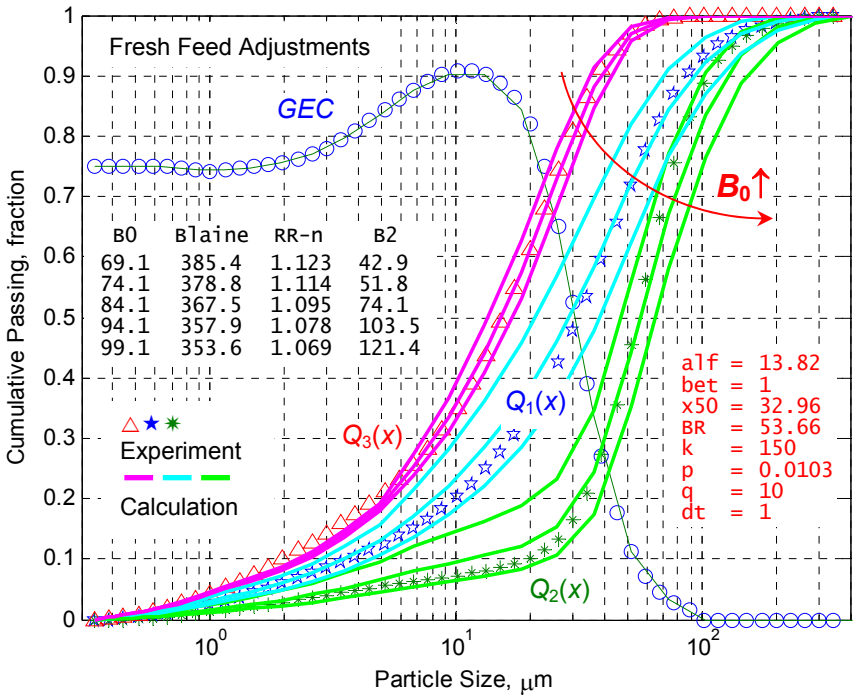

Figure 5.4. Model Response to the Fresh Feed Adjustments.

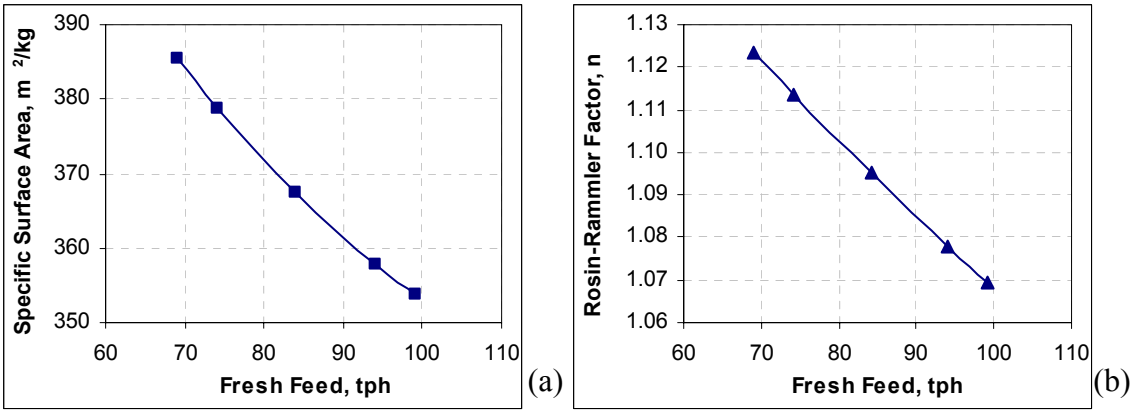

Figure 5.5. Product Fineness Response to the Fresh Feed Adjustments
(a – Specific Surface Area; b – Rosin-Rammler Shape Factor).

The modeled response of the circuit to the change in the fresh feed rate is consistent with the physical nature of the classification process. With the separator

parameters remaining unchanged (the cut size of the grade efficiency curve was kept constant throughout the fresh feed variations). The amount of material per unit volume of air in the classification zone increased, which in turn impaired the classification process and led to the increased number of the finer particles bypassing the separator and turning into the coarse material stream (see section 2.2.2.1).

5.3.2. Rejects Rate Correlation

The process value of the rejects flow rate is registered by the impact flow-meter installed in the air slide that carries the coarse particles from the separator to the mill's inlet for an additional cycle of grinding. The functionality of the impact-flow meter is based on the measurement of a kinetic impulse imposed by a moving material stream upon a hinged gate installed inside the air slide. The measured impulse is interpreted as the rejects flow rate value. The operation of the impact flow-meter is characterized by a high level of variability due to the spike nature of the instrument's signal. An accurate initial calibration of the flow-meter after installation followed by the periodic tunings is crucial for reliable reproducible measurements. The obtained rejects flow rate is stored in the PDH system and is part of the historical data collected from the pilot plant.

The rejects rate calculated from the population balance approach differs from the value measured by the impact flow-meter. For the time of sampling during the "NSNA" conditions, the flow-meter rejects rate reached 192.9 tph (see Table 4.3), whereas the population balance method and the Markov chain model estimated the rejects rate at 74.1 tph (see Figure 5.2). Such a difference may be a consequence of an improper installation or calibration of the impact flow-meter. Although the value measured in the air slide may be off in magnitude, the population balance calculated and flow-meter measured rejects rates may be correlated, assuming that the flow-meter measurements are consistent with respect to the first order changes of the flow rate.

Since the majority of the historical process data representing the rejects flow rate is available in the form determined by the impact flow-meter, the model-calculated rejects rate should be corrected to correspond to the flow-meter values:

$$B_2^{cor} = K \cdot B_2^{cal}, \tag{5.4}$$

where,

B_2^{cal} – Model-calculated rejects flow rate, tph;

K – Correction coefficient;

B_2^{cor} – Corrected rejects flow rate, tph.

The correction coefficient, *K*, serves as a scaling factor between the two available rejects rate values and can be derived from the data collected during the analysis of the circuit's response to the fresh feed adjustments in the previous section. Because the fresh feed adjustments were performed for a constant cut size of the grade efficiency curve (i.e., constant speed and air flow of the separator), the circulation load and the circulation factor defined, respectively, in Equations (2.36) and (2.37) should be constant. With this, *K* can be calculated using the following expression:

$$K = \frac{\text{C.F.}^{cal}}{\text{C.F.}^{test}} = \frac{B_2^{test}}{B_0^{test}} \cdot \frac{B_{0i}^{cal}}{B_{2i}^{cal}}, \tag{5.5}$$

where,

B_2^{test} – Rejects rate estimated by the impact flow-meter, tph;

B_0^{test} – Feed rate at the time when the flow-meter reading was taken, tph;

B_{0i}^{cal} – A set of feed rates used in calculation of the circuit response, tph;

B_{2i}^{cal} – A set of model-calculated reject flow rates, tph.

Equation (5.5) allows one to define a relationship between the correction coefficient, *K*, and the model-calculated rejects flow rates shown in Figure 5.5. The correlation curve and the regression formula are given in Figure 5.6. An excellent R^2-value of 0.9999 proves that the derived relationship is legitimate.

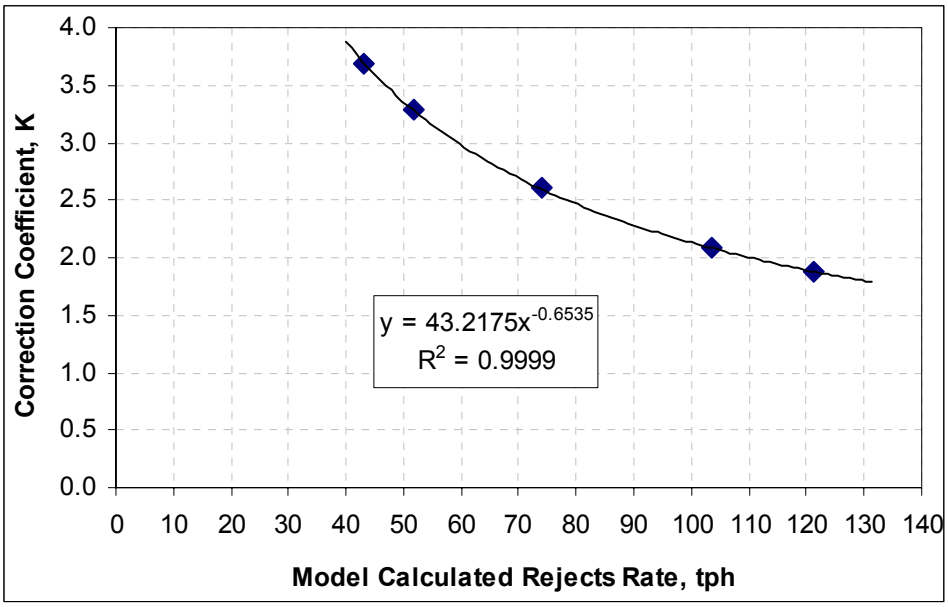

Figure 5.6. Correction Coefficient for the Rejects Rate Correlation.

5.3.3. Response to the Separator Cut Size Adjustments

Similarly to the analysis of the fresh feed adjustments, the finish mill circuit was calculated for several values of the separator cut size using the model parameters identified in section 5.1. The grade efficiency curve defined for the "NSNA" testing conditions of Day 1 was linearly transformed for different cut size values along the horizontal axis as suggested by Benzer et al. (2001). The calculated PSD's of the final product are shown in Figure 5.7 and accompanied by both calculated and corrected rejects flow rates, specific surface area, and Rosin-Rammler *n*-values.

With an increase in the separator cut size, induced by either an increase of the separator air flow or a decrease of the rotor speed, the particle size distributions shifted to the right. The specific surface area of the final product dropped for the higher cut size values and its PSD became wider, resulting in lower values of the Rosin-Rammler shape factor, *n* – see Figure 5.8 (a) and (b).

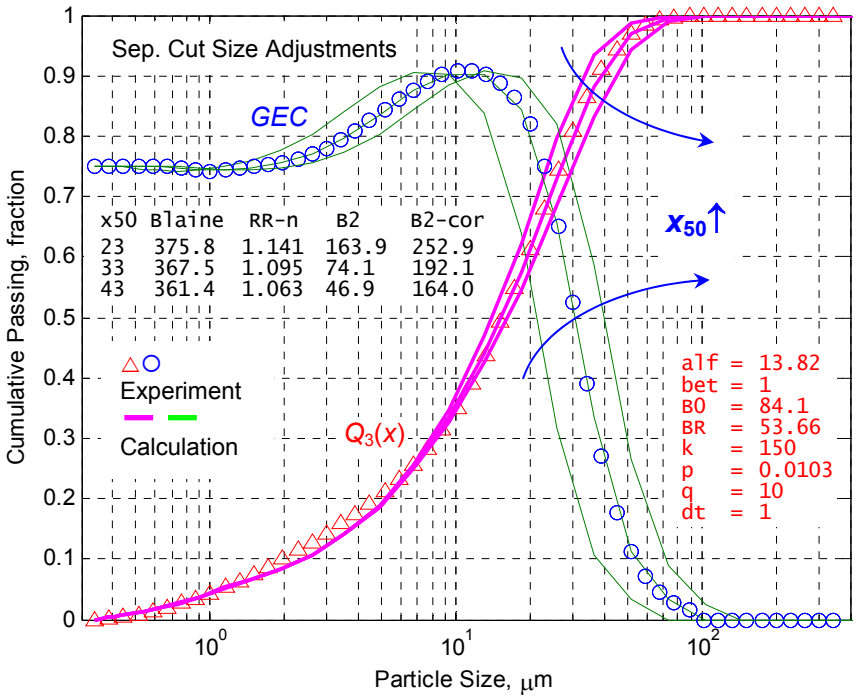

Figure 5.7. Model Response to the Separator Cut Size Adjustments.

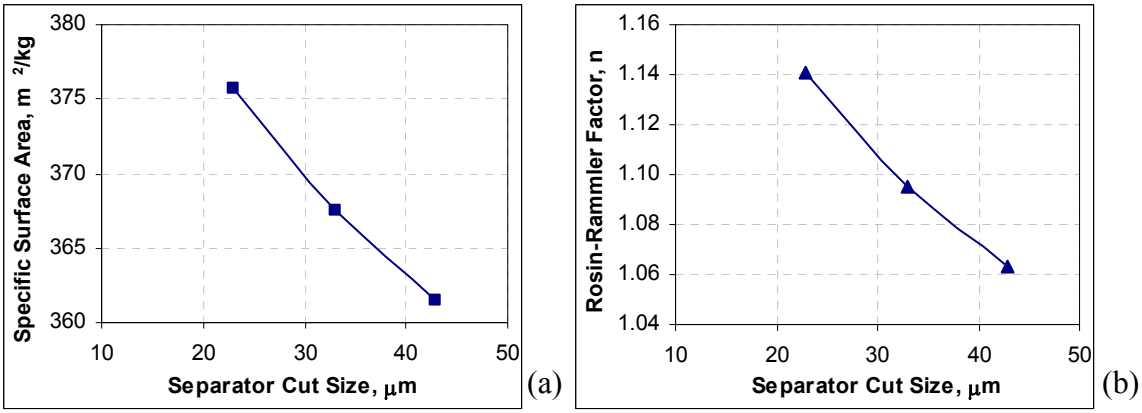

Figure 5.8. Product Fineness Response to the Separator Cut Size Adjustments (a – Specific Surface Area; b – Rosin-Rammler Shape Factor).

The circuit's response to the change in the cut size of the separator is consistent with both the physical nature of the classification process and various regimes during the

field data collection (see Table 4.4). For the constant fresh feed rate, an increase in the cut size value, for instance, due to a decrease in the separator rotor speed, allows more coarse particles to enter the fine fraction stream. This reduces both the rejects flow rate (Figure 5.7) and the fineness of the final product (Figure 5.8).

5.3.4. Specific Surface Area Control

The quality control objective of the grinding process assumes maintaining the specific surface area of the final product at the target value by virtue of adjusting the manipulated parameters of the circuit: separator cut size and fresh feed rate. The identified Markov chain model was used to simulate such quality control procedures.

In the previous sections, the adjustments of the fresh feed rate and separator cut size were performed independently. The cement fineness control, however, calls for the simultaneous regulation of the above parameters. The outcome of the simulation of the specific surface area control is shown in Figure 5.9.

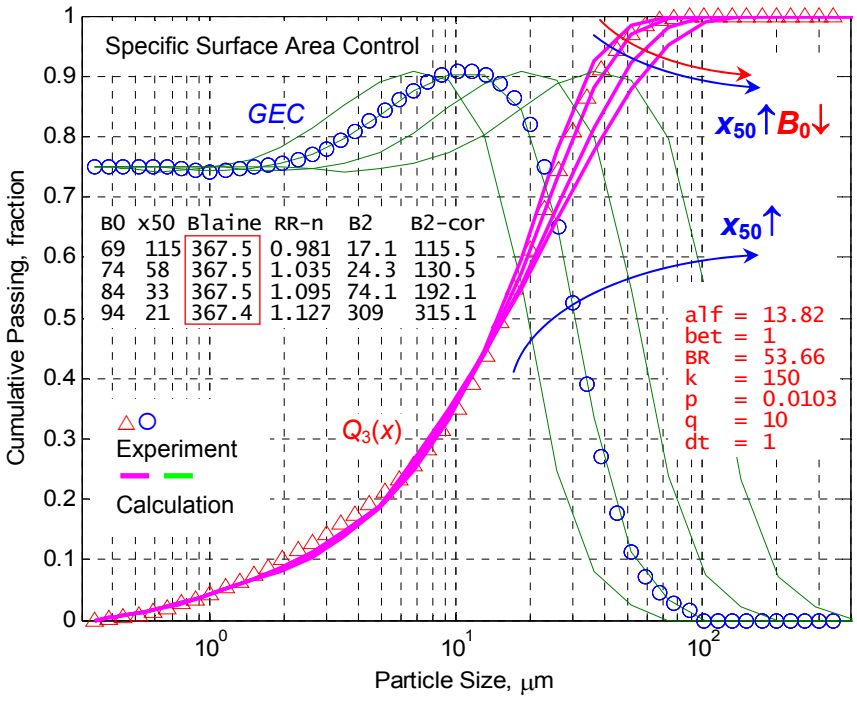

Figure 5.9. Simulation of the Specific Surface Area Control.

To produce the results shown in the figure above, the fresh feed rate was changed in the neighborhood of the nominal "NSNA" value of 84.1 tph, for which the model parameters were identified. At the same time, the cut size of the separator was adjusted so that the calculated specific surface area was equal to the value of 367.5 m^2/kg achieved at the nominal regime. Since an increase in the fresh feed rate causes a decrease of the specific surface area, the cut size of the separator had to be decreased in order to maintain the surface area target. In terms of adjusting the actual manipulated parameters of the separator, this reduction in the cut size can be fulfilled by either increasing the separator rotor speed or decreasing the separator air flow.

Even though the specific surface area was maintained at the target value, the particle size distribution of the final product was effected by the changes in the fresh feed rate and separator cut size. As seen from Figure 5.9, the cut size adjustments had a more prominent effect on the Rosin-Rammler shape factor, *n*, such that the calculated results followed the tendency observed in the previous section, where the higher cut size values produced wider particle size distributions and lower RR *n*-values.

The response of the rejects flow rate to the fineness control procedure was in line with the earlier introduced separate responses to the fresh feed rate and separator cut size. The rejects rate increases with the feed rate increase and separator cut size decrease.

5.3.5. Clinker Grindability and Circulation Load of the Circuit

In section 2.3.4, it was shown that the circulation load (C.L.) of the circuit can be used as an indicator of the grindability of clinker. Based on the results achieved in the analysis of the circuit's parametric response, different levels of clinker grindability would entail the following circuit's dynamics.

For the constant fresh feed rate, a sudden change in the grindability of clinker would require an adjustment of the separator cut size in order to maintain the target specific surface area of the final product. For instance, if the clinker hardness increases, the tube mill will produce a coarser product after one passage of the material through the mill. Because of that, the concentration of the coarser particles in the classification zone of the separator will increase and a higher number of larger particles will be able to

escape into the final product flow decreasing the fineness of the final product. The plant operator will be required to decrease the separator cut size in order to maintain the target specific surface area of the product, which will cause the rejects flow rate to increase. Therefore, for the same fresh feed rate and harder clinker nodules, the circulation load of the circuit determined by Equation (2.36) will increase.

In the Markov chain model, the clinker grindability is comprised within parameter α of the selection function defined in Equation (3.4). In order to investigate the effect of the clinker hardness on the production rate of the process, the coefficient α was correlated with several levels of clinker grindability expressed through the circulation load of the circuit. For the constant "NSNA" fresh feed rate and separator cut size, a set of α-values was identified to produce a set of C.L. values. The derived relationship, shown in Figure 5.10, is consistent with the physical meaning of the parameter α. As the hardness of clinker increases and the circulation load of the circuit goes up, the amount of the material, $s_j \Delta t$, transferred from the origin fraction, j, into the recipient fraction, i, decreases (see Figure 3.3).

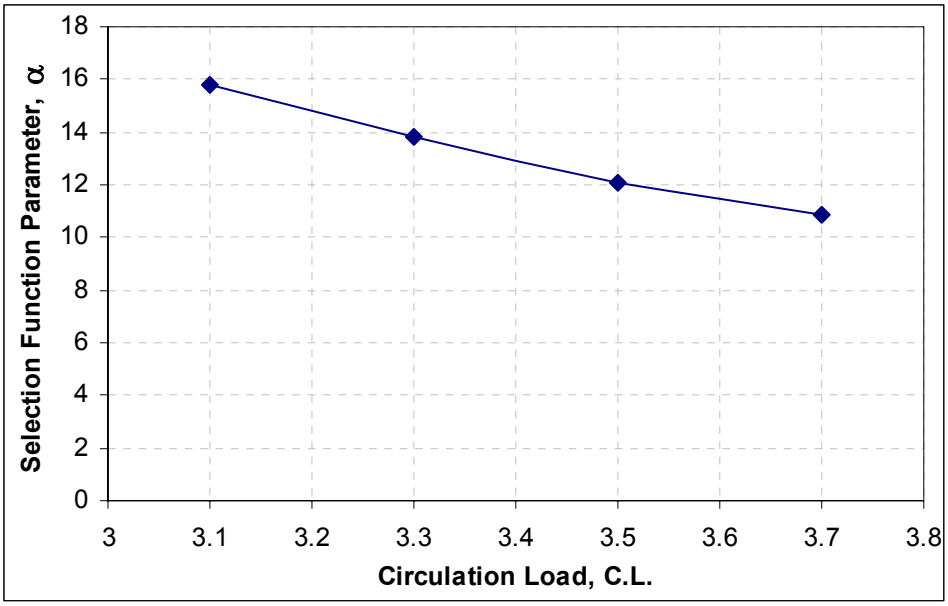

Figure 5.10. Selection Function α-Parameter vs. Circulation Load of the Circuit.

For each α, the model was calculated for a set of fresh feed rates. The adjustments to the separator cut size value were used to produce the circulation load values of the circuit of 3.1, 3.3, 3.5, and 3.7 as well as maintain the nominal calculated specific surface value of 367.5 m^2/kg. The results are presented in Table 5.2.

Table 5.2. Model Calculations for Different Circulation Loads of the Circuit.

α	B_0	B_2^{cal}	B_2^{cor}	C.L.^{cor}	Ave. Blaine
1/s	tph	tph	tph	–	m^2/kg
15.815	75.0	41.8	157.5	3.1	368.3
	80.0	50.3	168.0		
	85.0	59.9	178.5		
	90.0	70.7	189.0		
13.820	72.0	48.3	165.6	3.3	367.5
	77.0	58.6	177.1		
	81.0	67.8	186.3		
	84.1	75.6	193.4		
	87.0	83.4	200.2		
12.103	64.0	43.7	160.0	3.5	366.9
	68.0	52.1	170.0		
	72.0	61.4	180.0		
	76.0	71.8	190.0		
	80.0	83.2	200.0		
10.895	61.0	47.5	164.7	3.7	366.2
	64.0	54.6	172.8		
	67.0	62.3	180.9		
	70.0	70.7	189.0		
	74.0	83.0	199.8		

The simulated process data shown in the table above provides data for determining the rejects rate vs. fresh feed relationship for different levels of clinker grindability. This data will be used in the next section of the dissertation to formulate the control strategy objective for the grinding circuit at the pilot cement plant.

6. CONTROL ALGORITHM SUGGESTIONS

In this section, the control strategy objectives are formulated based on the calculation results of the Markov chain model, production rate and energy goals of the cement manufacturer, and the desired particle size characteristics of the final product.

6.1. REJECTS-FRESH FEED SPACE

When plotted, the simulated data presented in Table 5.2 forms a space of calculated values of the rejects and fresh feed rates. In order to compare the simulated results with the actual process values, the PDH system was queried for the retrospective values of the fresh feed and reject flow rates. From a total of two years of data, only the points collected after the mill upgrade procedure described in section 2.3.4 were used in this query. Similarly to the data search performed in section 4.2.1, the following criteria were used to isolate the one-hour periods of circuit's stable operation, for which the process values were obtained:

- Same type of cement being produced
- Blaine value at the target of 380 m^2/kg (in the range of 375-385 m^2/kg)
- Rejects rate between 150 and 210 tph
- Rejects rate STD < 20.0 tph
- Fresh feed rate STD < 5.0 tph
- Separator rotor speed STD < 3.0 rpm

The extracted database contained the rejects-fresh feed pairs, for which the Blaine specific surface area target was met and the process parameters of the circuit did not fluctuate much, resulting in low standard deviation values of their measured signals. If plotted without sorting, the rejects-fresh feed rate values form a shapeless blot of data points as shown in Figure 6.1, "All data" points. However, if the circulation load is calculated using the obtained flow rates and the database is sorted using the C.L. values, the rejects-fresh feed space transforms into a series of rising lines, each characterized by the specific C.L. value. Moreover, the simulated data from Table 5.2 plotted in the same coordinated complements the whole picture virtually flawlessly: see Figure 6.1.

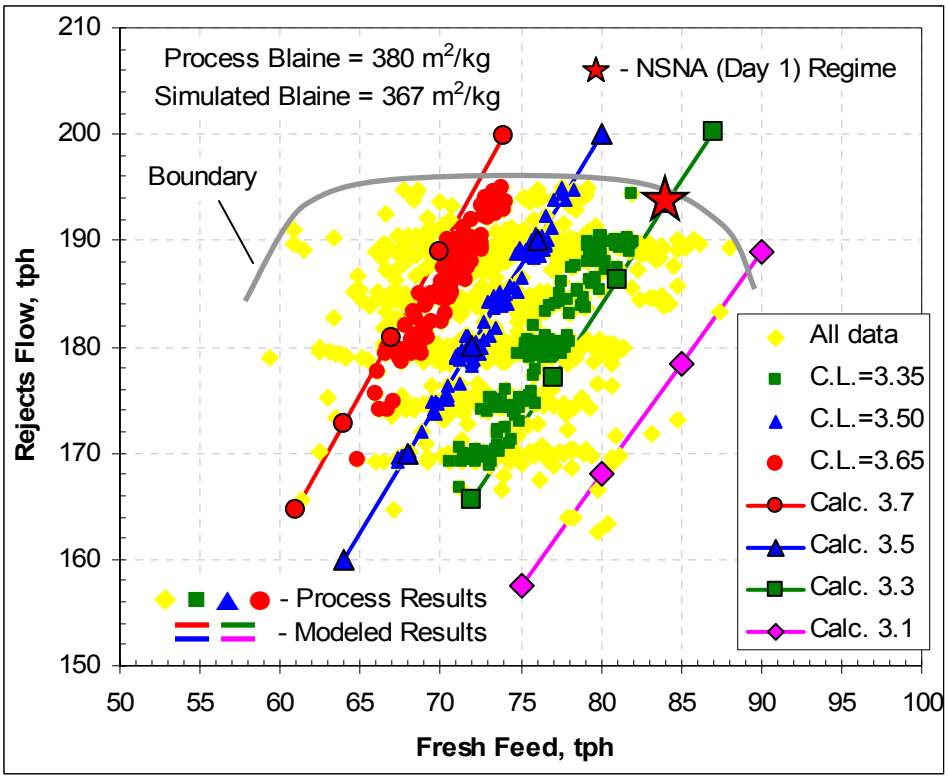

Figure 6.1. Rejects-Fresh Feed Operational Space.

The reject-fresh feed lines for the higher circulation loads are located to the left side of the operational space. This means that in order to grind a harder clinker (higher C.L.) and produce the same specific surface area of the final product as the softer clinker (lower C.L.), the fresh feed rate should be decreased. Indeed, the volume of the mill has a constant value, so in order to accommodate a harder material requiring multiple passages trough the mill, the input of the fresh unground clinker should be reduced.

6.2. BOUNDARY CONDITIONS

Since the proposed simulation model of the grinding process does not employ any process constraining parameters, the circuit can be calculated for virtually any fresh

feed rate, both realistic and non-realistic. The historical process data and equipment specification data should be used to define the running limits of the system.

The topmost values of the graph shown in Figure 6.1 represent the highest production rates for each C.L. ratio achieved during the observed time period. These topmost values, fringed by the gray "Boundary" line (see figure above), can be viewed as the constraint data for the Markov chain model. When attempting to surpass the boundary line, the running limits of such pieces of equipment as elevator, separator rotor motor, separator fan motor, and material flow capacity of the mill's inter-compartment division screen should be carefully analyzed for each circulation load value. Then, taking this information into account, the increase of the production rate can be performed only while maintaining the final product quality and guaranteeing the equipment safety.

It should be strongly emphasized that the production rates during the field sampling procedure were already neighboring the operational boundary. For instance, the feed rate value during the "Normal Speed – Normal Air" operating conditions on the first day of sampling was in the immediate proximity of the highest rate value ever observed for the current circulation ratio (see the red star in Figure 6.1). This may explain the difficulty to produce wide operating conditions of the separator on the sampling days, resulting in narrow test space formed by the three Tromp curves.

6.3. CONTROL STRATEGY OBJECTIVES

Based on the state of the art review of the industrial clinker grinding proposed in the beginning of this dissertation, the objectives of the milling process can be divided into three groups:

1. Maximization of the production rate
2. Minimization of the specific electrical consumption of the circuit
3. Meeting the cement fineness and PSD shape requirements

As it was introduced in section 2.3.4, the first and second objectives can be combined in one, since the increase in the production rate automatically decreases the

specific electrical consumption of the mill, in particular, and the grinding circuit, as the whole. It was also justified that the softer clinkers will require lower circulation load of the circuit and allow for the higher production rates and lower electrical energy intake. The literature review revealed that various levels of fineness of the final product and the engineered shapes of its PSD can be used to improve target performance characteristics of the cement. By means of the developed Markov chain model, the effect of the manipulated parameters of the circuit, namely the fresh feed rate and the separator cut size, on the specific surface area and particle size distribution shape of the final product was analyzed via a numerical simulation.

Using all the findings presented in this dissertation, the key points of the control algorithm for the closed-circuit finish grinding process can be formulated as the following.

1. For a given hardness of clinker, the fresh feed can be increased until the circuit's constraint conditions are met as per Figure 6.1. The increased fresh feed rate will guarantee reduction of the specific electrical consumption of the circuit.
2. While increasing the fresh feed rate, the separator cut size should be adjusted simultaneously in order to maintain the target specific surface area of the final product as per simulation results described in section 5.3.4.
3. The separator cut size should be regulated by changing either the rotor speed or the air flow in the classification zone of the separator. The separator rotor speed is a more sensitive parameter and should be utilized first in controlling the surface area of the product.
4. If a certain shape of the particle size distribution of the final product is desired, the combination of the fresh feed and separator cut size adjustments can be utilized as per simulation results described in section 5.3.4 in order to achieve that shape. While maintaining the target Blaine value, different combinations of the fresh feed and separator cut size will move the operating point along the C.L. line shown in Figure 6.1 and produce different *n*-values of the Rosin-Rammler distribution. In this case, the maximization of the production rate objective may be sacrificed in order to achieve the desired cement PSD shape.

6.4. CLINKER GRINDABILITY PATTERN

Prediction of the clinker grindability can further enhance the control strategy of the finish milling process. The PDH data obtained for the rejects-fresh feed space analysis was used to plot the circulation load values as a function of time: Figure 6.2 (a).

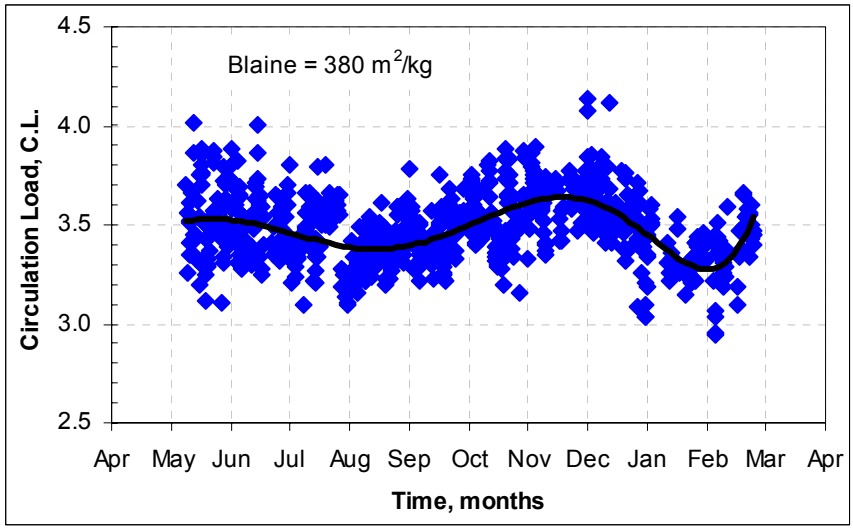

(a)

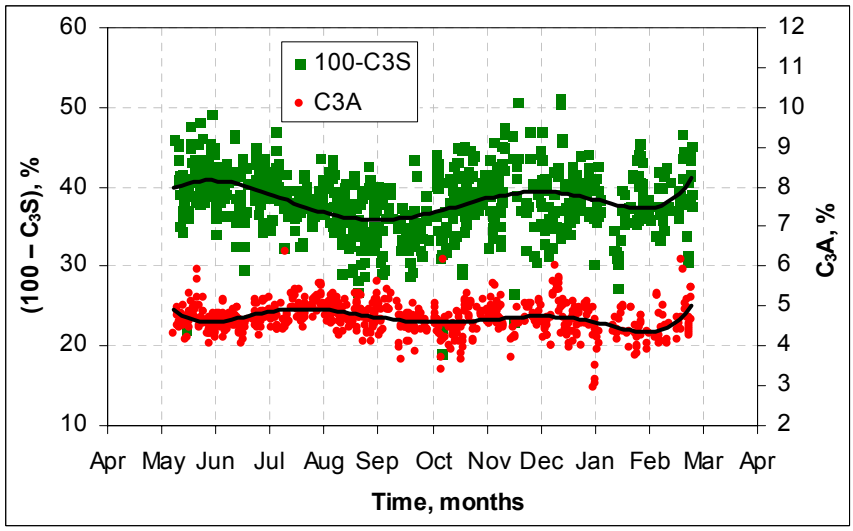

(b)

Figure 6.2. Variation of Clinker Grindability with Time
(a – Circulation Load vs. Time; b – Clinker Mineralogy vs. Time).

The circulation value versus time plot revealed a distinct pattern with the periodic ups and downs of the grindability of clinker. In attempt to explain such a pattern, the contents of the selected mineralogical phases of clinker were plotted against time as well: see Figure 6.2 (b). As it was described in section 2.3.1, the C_3S phase is the softest phase of clinker, whereas the C_3A phase is among the hardest. The inverted content of the alite phase of (100% – C_3S) was calculated and plotted against time in order to have all of the grindability parameters indicate the hardness of clinker.

The inverted alite phase content produced a grindability pattern similar to one by the circulation load. The two parameters show an apparent correlation. The aluminate phase, however, did not exhibit a clear pattern that could be correlated with the circulation load of the grinding circuit. The latter observation is in line with that of Hills (1995), who reported that the C_3A phase effect on the grindability of clinker could not be clearly determined.

The correlation of clinker mineralogy with circulation load of the circuit and the parameter α of the selection function of the Markov chain model should be thoroughly investigated. By means of the numeric analysis, the prediction of the clinker grindability can be incorporated into the control algorithm of the finish mill circuit and improve its dynamic characteristics.

7. CONCLUSIONS AND RECOMMENDATIONS FOR FUTURE WORK

7.1. CONCLUSIONS

The main goal of the proposed dissertation was to reveal the relationships among the factors, affecting the cement finish milling process. The numerical simulation based on the Markov chain theory was employed to examine these relationships. The developed model was shown as a suitable and effective tool in simulation of the grinding process in a closed circuit. Knowing the relationships among the cement's performance characteristics, its fineness properties, process parameters of the circuit, and hardness of the clinker nodules, it became possible to suggest the process control steps towards improving both energy and fineness aspects of efficiency of the cement finish grinding.

7.1.1. Cement Quality Target Related Conclusions

- The state of the art of industrial clinker grinding was reviewed and the key parameters of the cement quality influencing its performance as a construction material were identified as the specific Blaine surface area, the percent passing though 45-μm sieve, and the particle size distribution shape.
- The literature review revealed that, besides the commonly applied increase of the Blaine specific surface area when an early strength of the product is desired, various engineered shapes of the cement's PSD (narrow, wide, multimodal, etc.) can also be utilized to affect certain performance and hydration characteristics of the cements: strength development, rate of hydration, setting time, heat release, water demand, workability, chemical shrinkage, porosity, and other.
- The literature review also showed that while it is feasible to engineer a particular particle size distribution of the cement under laboratory conditions, it is not evident how to generate the desired PSD in the industrial finish mill. Specific recommendations for producing the desired PSD at the cement plant are required.

7.1.2. Field Sampling Results Related Conclusions

- Total of six separator regimes were analyzed at the pilot cement plant. Three regimes were characterized by the change of the separator rotor speed and other three – by the change of the separator air flow.
- Out of 6 analyzed regimes, 5 were consistent with the testing conditions. However, the "Normal Speed – High Air" operating regime on the second day of the sampling procedure produced anomalous PSD and Tromp curve results. The preliminary analysis of the regime suggested an excessive agglomeration of the particles in the classification zone of the separator and would need verification.
- The separator adjustments showed only a minor effect of the separator rotor speed and air flow changes on the width of cement's PSD with the Rosin-Rammler distribution shape factor, *n*, ranging between 1.066 and 1.089. The separator air adjustments produced a slightly higher average *n*-value of 1.080 (narrower PSD) compared to the separator speed alterations with an average *n*-value of 1.071 (wider PSD).
- The calculated Tromp curve results suggested good performance characteristics of the installed separator with the bypass value between 6.3 and 9.8% and the sharpness of separation between 1.698 and 1.803 versus expected 2.0 or more.
- The operating point of the pilot circuit during both sampling days was diagnosed to be located in a close proximity of the constraint boundary of the rejects-fresh feed space. In other words, the circuit was running close to its maximum capacity at the given clinker grindability. This might have contributed to the difficulty to produce wide operating space of the separator while adjusting its rotor speed and air flow noted earlier.
- Sampling and measurement errors inherent to the field and laboratory testing procedures were identified and the specific measures were exercised in effort to minimize these errors.
- The Blaine specific surface measurements as per the ASTM C 204 test method were shown to exhibit a high level of variability with a maximum observed

deviation from the average value of ±5.2%. Such error was contributed to the human factor in material sampling and conducting the air permeability test. The data implied that the laser particle size distribution should be employed to estimate the specific surface area of the produced cement. If a laser analyzer is not available at the cement plant, then multiple Blaine value measurements should required in order to achieve representative specific surface area results.

7.1.3. Model Related Conclusions

- The Markov chain theory was introduced to describe the processes of grinding, classification, and particle transport in a closed finish mill circuit and resulted in a flexible inexpensive analysis tool.
- The parameters of the Markov chain model were successfully identified using the collected particle size distribution and process data.
- The developed Markov chain model was used to analyze the parametric response of the closed grinding circuit to the changes in the manipulated parameters, namely, the fresh feed rate and the separator cut size. Their effect on the specific surface area and PSD shape of the final product was established via a numerical simulation.
- The influence of the separator cut size adjustments on the Rosin-Rammler shape factor, *n*, of the cement's PSD ranging between 1.063 and 1.141 was stronger than that of the fresh feed with the RR *n*-value ranging between 1.069 and 1.123. The simultaneous regulation of both manipulated parameters in order to maintain the target specific surface area of the final product produced RR *n*-values ranging between 0.981 and 1.127.
- The Markov chain model was used to calculate the rejects-fresh feed operational space for different levels of clinker grindability. Using the historical process data collected form the pilot plant, the simulation results were successfully validated and the process constraint conditions were identified.
- Using the historical and simulation data, the relationships among the grindability of clinker, circulation load of the circuit, contents of the alite phase, and parameters of the selection function were recognized and suggested for further development.

7.1.4. Control Algorithm Related Conclusions

- The production, energy, and product quality objectives were identified for the industrial process of clinker grinding. The production and energy objectives were combined due to their distinct interrelationship.
- The effect of the circuit's process parameters on the production rate, specific energy consumption of the mill, and particle size distribution of the final product was analyzed using the developed Markov chain model.
- An outline of a control algorithm for a closed finish milling circuit was introduced. The algorithm describes particular procedures for increasing the production rate, decreasing the specific electrical consumption, maintaining the specific surface area, and regulating the shape of the particle size distribution of the final product of an industrial mill.

7.2. RECOMMENDATIONS FOR FUTURE WORK

The following are the recommended research activities that are anticipated to benefit and complement the study proposed in this dissertation.

7.2.1. Model Related Recommendations

The main calculating unit of the Markov chain model is the matrix of grinding, G. Below are recommendations for improving the accuracy of matrix G.

- The relationship between the clinker fracture characteristics, phase mineralogy, and the selection function coefficient α should be identified and included in the calculation of the entries of matrix G.
- The relationship between the number of elementary cells of the model, k, and the residence time of the tube mill should be identified and applied to the model.
- A study on possible agglomeration of the particles inside the mill should be carried out and the results should be included in the model by introducing the non-zero entries of the lower triangle of the matrix of grinding, G.

- A study on the attrition characteristics of the grinding process inside the tube ball mill should be performed introducing different breakage distribution functions: e.g., trapezoidal, power, exponential, etc. The results should be correlated with the clinker fracture characteristics and incorporated in the matrix of grinding, *G*.

  The classification matrix, *C*, can be complemented in the following way:
- The analytical functions representing the grade efficiency curve and accounting for the laws of aerodynamics, geometrical configuration of the classification zone, separator gas and rotor velocity, and other effects should be introduced in calculation of the classification matrix, *C*. The results should be compared with those achieved using the balance population method for determining GEC.

7.2.2. Process Analysis Related Recommendations

- The circuit sampling should be repeated for a wider range of values of the tested parameters without concerns about their impact on the final product quality. This will provide a more meaningful operational space of the separator speed and air flow values.
- The difference between the rejects flow rates measured by the impact flow-meter and calculated using the population balance method should be elucidated.
- The elevator motor kilowatts signal should be correlated with the throughput rate of the mill as a replacement of the less reliable rejects flow meter signal.
- The effect of the increased air flow through the separator on the efficiency of the classification process should be investigated. The pronounced agglomeration of the very fine particles at high air should be analyzed and understood.
- The correlation between the grindability of the fresh feed mix and the amount of gypsum and limestone in the mix should be defined.

7.2.3. Control Strategy Recommendation

- The control strategy should be established to predict the specific surface area of the final product based on the clinker mineralogical data, current fresh feed rate, circulation load, separator rotor speed and air flow.

REFERENCES

Alsop, P. (2001). *Cement plant operations handbook for dry process plants*, Tradeship Publications Ltd., Portsmouth, United Kingdom.

Andreev, A., Otwinovski, H., Urbaniak, D., and Mejeoumov, G. (2006). "Analysis of the dynamic classifier efficiency." *Proceedings of the XIX-th International Scientific Conference: Mathematical Methods in Engineering and Technology*, Voronezh, Russia, 120 (in Russian).

ASTM C 115. (2003). "Standard test method for fineness of portland cement by the turbidimeter." *American Society for Testing and Materials*, West Conshohocken, PA.

ASTM C 150. (2005). "Standard specification for portland cement." *American Society for Testing and Materials*, West Conshohocken, PA.

ASTM C 183. (2002). "Standard practice for sampling and the amount of testing of hydraulic cement." *American Society for Testing and Materials*, West Conshohocken, PA.

ASTM C 188. (2003). "Standard test method for density of hydraulic cement." *American Society for Testing and Materials*, West Conshohocken, PA.

ASTM C 204. (2005). "Standard test method for fineness of hydraulic cement by air-permeability apparatus." *American Society for Testing and Materials*, West Conshohocken, PA.

ASTM C 430. (2003). "Standard test method for fineness of hydraulic cement by the 45-μm (No. 325) sieve." *American Society for Testing and Materials*, West Conshohocken, PA.

ASTM C 786. (2003). "Standard test method for fineness of hydraulic cement and raw materials by the 300-μm (No. 50), 150-μm (No. 100), and 75-μm (No. 200) sieves by wet methods." *American Society for Testing and Materials*, West Conshohocken, PA.

ASTM C 1157. (2003). "Standard performance specification for hydraulic cement." *American Society for Testing and Materials*, West Conshohocken, PA.

ASTM D 409. (2002). "Standard test method for grindability of coal by the Hardgrove-machine method." *American Society for Testing and Materials*, West Conshohocken, PA.

Austin, L., Bagga, P., and Celik, M. (1981). "Breakage properties of some materials in a laboratory ball mill." *Powder Technology*, 28, 235-241.

Bentz, D., Garboczi, E., Haecker, C., and Jensen, O. (1999). "Effects of cement particle size distribution on performance properties of portland cement-based materials." *Cement and Concrete Research*, 29, 1663-1671.

Benzer, H., Ergun, L., Lynch, A., Oner, M., Gunlu, A., Celik, I., and Aydogan, N. (2001). "Modeling cement grinding circuits." *Minerals Engineering*, 14(11), 1469-1482.

Berger, M. (1993). *An introduction to probability and stochastic processes*, Springer-Verlag New York, Inc., New York, NY.

Berthiaux, H. (2000). "Analysis of grinding process by Markov chains." *Chemical Engineering Science*, 55, 4117-4127.

Berthiaux, H., Mizonov, V., and Zhukov, V. (2005). "Application of the theory of Markov chains to model different processes in particle technology." *Powder Technology*, 157, 128-137.

Bhatty, J., Miller, F., and Kosmatka, S. (2004). *Innovations in portland cement manufacturing*, CD-ROM: SP400, Portland Cement Association, Skokie, IL.

van Breusegem, V., Chen, L., Werbrouck, V., Bastin, G., and Wertz, V. (1994). "Multivariable linear quadratic control of a cement mill: an industrial application." *Control Engineering Practice*, 2(4), 605-611.

Ching, W.-K., and Ng, M. (2006). *Markov chains: models, algorithms and applications*, Springer Science+Business Media, Inc., New York, NY.

Delagrammatikas, G., and Tsimas, S. (2004). "Grinding process simulation based on Rosin-Rammler equation." *Chemical Engineering Communications*, 191, 1362-1378.

Djamarani, K., and Clark, I. (1997). "Characterization of particle size based on fine and course fractions." *Powder Technology*, 93, 101-108.

Drzymala, J. (2003). "Sorting as a procedure of evaluating and comparing separation results." *Physicochemical Problems of Mineral Processing*, 37, 19-26.

Ferraris, C., Hackley, V., Avilés, A., and Buchanan, C. (2002). "Analysis of the ASTM Round-Robin test on particle size distribution of portland cement: Phase I." *National Institute of Standards and Technology Report No. 6883*, Technology Administration, U.S. Department of Commerce, Washington, DC.

Fortsch, D. (2005). "Wear impacts in slag grinding in various grinding technologies." *Cement Industry Technical Conference Record*, Kansas City, MO, 177-191.

Frias, M., Sanchez de Rojas, M., Luxan, M., and Garcia, N. (1991). "Determination of specific surface area by the laser diffraction technique. Comparison with the Blaine permeability method." *Cement and Concrete Research*, 21, 709-717.

Frigione, G., and Marra, S. (1976). "Relationship between particle size distribution and compressive strength in portland cement." *Cement and Concrete Research*, 6(1), 113-128.

Fuerstenau, M., and Han, K. (2003). *Principles of mineral processing*, Society for Mining, Metallurgy, and Exploration, Inc., Littleton, CO.

Gill, A. (1999). "Calculating clinker grindability using an automated laboratory and computer technology." *Portland Cement Association Fall Technical Session*, M228-8, Oak Brook, IL.

Hawkins, P., Tennis, P., and Detwiler, R. (2003). *The use of limestone in portland cement: a state-of-the-art review*, EB227, Portland Cement Association, Skokie, IL.

Hills, L. (1995). *The effect of clinker microstructure on grindability*, RP 331, Portland Cement Association, Skokie, IL.

Hills, L. (1999). *Under the microscope: an introduction to clinker microscopy*, R&D Serial No. 2413, Portland Cement Association, Skokie, IL.

Juhasz A., and Opoczky L. (1990). *Mechanical activation of minerals by grinding: pulverizing and morphology of particles*, Ellis Horwood Limited Publishers, Chichester, United Kingdom.

Kawatra, S. (2006). *Advances in comminution*, Society for Mining, Metallurgy, and Exploration, Inc., Littleton, CO.

Kelly, E., and Spottiswood, D. (1982). *Introduction to mineral processing*, John Wiley & Sons, Inc., New York, NY.

Kemeny, J., and Snell, J. (1960). *Finite Markov chains*, D. Van Nostrand Company, Inc., Princeton, NJ.

King, R. (2001). *Modeling and simulation of mineral processing systems*, Butterworth-Heinemann, Oxford, United Kingdom.

Laurent, A. (1997). *Développement de nouveaux adjuvants destinés à la fabrication du ciment (agents de mouture) et à l'amélioriationd es propriétés rhéologiques du béton*, M.S. Thesis, University of Sherbrooke, Sherbrooke, Canada (in French).

Magdalinovic, N. (1989). "A procedure for rapid determination of the Bond work index." *International Journal of Mineral Processing*, 27, 125-132.

Martin, G., and McGarel, S. (2001). "Nonlinear mill control." *ISA Transactions*, 40, 369-379.

McElroy, M. (2002). *The atmospheric environment: effects of human activity*, Princeton University Press, Princeton, NJ.

Mehta, P. (1986). *Concrete: structure, properties, and materials*, Prentice-Hall, Inc., Englewood Cliffs, NJ.

Mejeoumov, G., Zhukov, V., and Mizonov, V. (2005a). "Application of the theory of Markov chains to model a closed milling circuit." *University Transactions: Chemistry and Chemical Engineering*, 48(4), 135-137 (in Russian).

Mejeoumov, G., Zhukov, V., and Mizonov, V. (2005b). "Simulation of a cement tube mill using the theory of Markov chains." *Proceedings of the XII-th International Scientific and Technical Conference: Current State, Prospects and Development of Electrical Technology (Benardosovskie Chtenia)*, Ivanovo, Russia, 124 (in Russian).

Mejeoumov, G., Zhukov, V., Andreev, A., and Kaniowski, P. (2007a). "Matrix model of a dynamic classifier." *Proceedings of the XX-th International Scientific Conference: Mathematical Methods in Engineering and Technology*, Yaroslavl, Russia, 160-161 (in Russian).

Mejeoumov, G., Zhukov, V., and Mizonov, V. (2007b). "Identification of the cell model of the closed cement milling circuit." *Proceedings of the XIV-th International Scientific and Technical Conference: Current State, Prospects and Development of Electrical Technology (Benardosovskie Chtenia)*, Ivanovo, Russia, 185 (in Russian).

Mishulovich, A. (2004). *Development of Crushability Criteria: Literature review*, R&D Serial No. 2785, Portland Cement Association, Skokie, IL.

Mizonov, V., Zhukov, V., and Bernotat, S. (1997). *Simulation of grinding: new approaches*, Ivanovo State Power Engineering University Press, Ivanovo, Russia.

Mizonov, V., Berthiaux, H., and Zhukov, V. (2002). *Application of the theory of Markovian chains to simulation and analysis of processes with granular media*, Ecole des Mines Press, Albi, France.

Mizonov, V., Berthiaux, H., Zhukov, V., and Bernotat, S. (2004). "Application of multi-dimensional Markov chains to model kinetics of grinding with internal classification." *International Journal of Mineral Processing*, 74S, S307-S315.

Mizonov, V., Zhukov, V., Korovkin, A., and Berthiaux, H. (2005). "On possible instability of throughputs in complex milling circuits." *Chemical Engineering and Processing*, 44, 267–272.

Navi, P., and Pignat, C. (1999). "Effects of cement size distribution on capillary pore structure of the simulated cement paste." *Computational Materials Science*, 16, 285-293.

Neville, A. (1995). *Properties of concrete*, Pearson Education Ltd., Singapore.

Rogers, L., and Williams, D. (2000). *Diffusions, Markov processes, and martingales*, Cambridge University Press, Cambridge, United Kingdom.

Ruth, M., Worrell, E., and Price, L. (2000). "Evaluating clean development mechanism projects in the cement industry using a process-step benchmarking approach." *Energy Analysis Department Report No. LBNL-45346*, University of California, Berkeley, CA.

Schnatz, R. (2004). "Optimization of continuous ball mills used for finish-grinding of cement by varying the L/D ratio, ball charge filling ratio, ball size and residence time." *International Journal of Mineral Processing*, 74S, S55-S63.

Skvara, F., Kolar, K., Novotny, J., and Zadak Z. (1981). "The effect of cement particle size distribution upon properties of pastes and mortars with low water-to-cement ratio." *Cement and Concrete Research*, 11, 247-255.

Strohman, N. (2000). "When, how, why, and what of grinding aids." *Portland Cement Association Fall Technical Session*, M229-8, Oak Brook, IL.

Tamir, A. (1998). *Applications of Markov chains in chemical engineering*, Elsevier, Amsterdam, The Netherlands.

Theisen, K. (1993). "Estimation of cement clinker grindability." *Proceedings of the 15th International Conference on Cement Microscopy*, Dallas, TX, 1-14.

Topalov, A., and Kaynak, O. (2004). "Neural network modeling and control of cement mills using a variable structure systems theory based on-line learning mechanism." *Journal of Process Control*, 14, 581-589.

Touil, D., Belaadi, S., and Frances, C. (2006). "Energy efficiency of cement finish grinding in a dry batch ball mill." *Cement and Concrete Research*, 36, 416-421.

Tsivilis, S., Voglis, N., and Photou, J. (1999). "Technical note: a study on the inter-grinding of clinker and limestone." *Minerals Engineering*, 12(7), 837-840.

Velez, K., Maximilien, S., Damidot, D., Fantozzi, G., and Sorrentino, F. (2001). "Determination by nanoindentation of elastic modulus and hardness of pure constituents of Portland cement clinker." *Cement and Concrete Research*, 31, 555-561.

Wang, L., Pereira, N., and Hung, Y.-T. (2004). *Handbook of environmental engineering Volume 1: air pollution control engineering*, Humana Press Inc., Totowa, NJ.

Wills, B. (1992). *Mineral processing technology*, Pergamon Press, Oxford, United Kingdom.

Yin, G., and Zhang, Q. (2005). *Discrete-time Markov chains*, Springer Science+Business Media, Inc., New York, NY.

Zhang, Y., and Napier-Munn, T. (1995). "Effects of particle size distribution, surface area and chemical composition on portland cement strength." *Powder Technology*, 83, 245-252.

Zhukov, V., Grekov, A., and Mizonov V. (1993). "Influence of gradation of the grinding media on kinetics of grinding." *Theoretical Foundations of Chemical Engineering*, 27(2), 199-201 (in Russian).

Zhukov, V., and Mizonov, V. (1995). "Optimal distribution of the grinding media sizes along the body of a tube ball mill." *Theoretical Foundations of Chemical Engineering*, 29(6), 646-650 (in Russian).

Zhukov, V., Mejeoumov, G., Ogurtsov, A., and Otwinovski, H. (2005). "Simulation of attrition in a fluidized bed." *Proceedings of the XII-th International Scientific and Technical Conference: Current State, Prospects and Development of Electrical Technology (Benardosovskie Chtenia)*, Ivanovo, Russia, 130 (in Russian).

APPENDIX A

LASER PARTICLE SIZE DISTRIBUTION DATA

Table A.1. Separator PSD Data Collected During Sampling Procedure (Day 1).

Particle Diameter	High Speed – Normal Air			Normal Speed – Normal Air			Low Speed – Normal Air		
	Cumulative Passing			Cumulative Passing			Cumulative Passing		
	Feed	Rejects	Fines	Feed	Rejects	Fines	Feed	Rejects	Fines
µm	%	%	%	%	%	%	%	%	%
0.339	0	0	0	0	0	0	0	0	0
0.389	0.109	0	0.175	0	0	0.165	0	0	0.149
0.445	0.287	0	0.461	0.163	0	0.438	0.163	0	0.392
0.510	0.545	0.132	0.875	0.401	0.119	0.837	0.398	0.127	0.743
0.584	0.882	0.302	1.415	0.710	0.274	1.359	0.702	0.294	1.198
0.669	1.288	0.508	2.066	1.084	0.460	1.989	1.066	0.497	1.743
0.766	1.757	0.746	2.811	1.513	0.676	2.710	1.479	0.735	2.366
0.877	2.279	1.011	3.638	1.992	0.918	3.506	1.936	1.006	3.057
1.005	2.857	1.302	4.548	2.522	1.187	4.378	2.437	1.309	3.820
1.151	3.496	1.621	5.555	3.109	1.485	5.338	2.987	1.646	4.668
1.318	4.202	1.966	6.668	3.757	1.811	6.394	3.591	2.016	5.611
1.510	4.967	2.330	7.879	4.460	2.160	7.539	4.246	2.411	6.647
1.729	5.785	2.707	9.176	5.212	2.527	8.766	4.947	2.825	7.770
1.981	6.648	3.090	10.543	6.004	2.908	10.061	5.690	3.248	8.970
2.269	7.549	3.473	11.966	6.828	3.298	11.415	6.472	3.673	10.239
2.599	8.487	3.851	13.437	7.682	3.690	12.826	7.293	4.094	11.575
2.976	9.461	4.219	14.954	8.564	4.081	14.293	8.157	4.503	12.975
3.409	10.477	4.574	16.528	9.478	4.467	15.827	9.073	4.899	14.451
3.905	11.550	4.915	18.183	10.438	4.845	17.452	10.057	5.279	16.022
4.472	12.697	5.243	19.952	11.459	5.214	19.196	11.128	5.644	17.715
5.122	13.938	5.558	21.876	12.562	5.573	21.098	12.313	5.997	19.567
5.867	15.301	5.864	24.019	13.775	5.924	23.213	13.641	6.340	21.631
6.720	16.816	6.165	26.450	15.126	6.269	25.601	15.146	6.677	23.964
7.697	18.510	6.465	29.245	16.645	6.611	28.329	16.855	7.011	26.629
8.816	20.402	6.774	32.479	18.355	6.955	31.460	18.786	7.345	29.689
10.097	22.514	7.102	36.222	20.278	7.309	35.057	20.952	7.684	33.202
11.565	24.865	7.467	40.536	22.437	7.688	39.174	23.360	8.039	37.224
13.246	27.488	7.901	45.458	24.859	8.112	43.856	26.018	8.423	41.801
15.172	30.428	8.455	50.994	27.585	8.620	49.126	28.944	8.862	46.958
17.377	33.751	9.216	57.084	30.665	9.272	54.965	32.167	9.394	52.675
19.904	37.542	10.333	63.582	34.162	10.168	61.284	35.731	10.084	58.868
22.797	41.897	12.050	70.238	38.146	11.474	67.900	39.691	11.041	65.356
26.111	46.906	14.737	76.719	42.673	13.446	74.527	44.102	12.441	71.871
29.907	52.615	18.878	82.664	47.769	16.456	80.807	49.007	14.557	78.083
34.255	58.980	24.956	87.766	53.401	20.949	86.376	54.412	17.776	83.670
39.234	65.824	33.210	91.843	59.445	27.314	90.953	60.259	22.552	88.392
44.938	72.818	43.369	94.873	65.683	35.658	94.413	66.399	29.252	92.135
51.471	79.524	54.573	96.968	71.826	45.598	96.807	72.595	37.918	94.924
58.953	85.494	65.626	98.321	77.570	56.267	98.321	78.543	48.074	96.885
67.523	90.400	75.441	99.142	82.670	66.592	99.198	83.938	58.779	98.197
77.340	94.107	83.380	99.615	86.982	75.673	99.666	88.541	68.946	99.037
88.583	96.697	89.350	99.870	90.459	83.099	99.896	92.246	77.877	99.546
101.460	98.342	93.475	100	93.121	88.660	100	95.028	84.982	99.839
116.210	99.284	96.116	100	95.065	92.500	100	96.959	90.107	100
133.103	99.770	97.719	100	96.450	95.013	100	98.202	93.545	100
152.453	100	98.669	100	97.448	96.648	100	98.966	95.801	100
174.616	100	99.242	100	98.200	97.764	100	99.432	97.320	100
200.000	100	99.603	100	98.792	98.567	100	99.716	98.359	100
229.075	100	99.836	100	99.267	99.157	100	99.891	99.066	100
262.376	100	100	100	99.660	99.609	100	100	99.567	100
300.518	100	100	100	99.879	99.861	100	100	99.845	100
344.205	100	100	100	100	100	100	100	100	100

Table A.2. Separator PSD Data Collected During Sampling Procedure (Day 2).

Particle Diameter	Normal Speed – High Air			Normal Speed – Normal Air			Normal Speed – Low Air		
	Cumulative Passing			Cumulative Passing			Cumulative Passing		
	Feed	Rejects	Fines	Feed	Rejects	Fines	Feed	Rejects	Fines
µm	%	%	%	%	%	%	%	%	%
0.339	0	0	0	0	0	0	0	0	0
0.389	0.114	0	0.161	0.102	0	0.158	0.121	0	0.176
0.445	0.298	0.114	0.420	0.270	0	0.415	0.316	0.104	0.458
0.510	0.566	0.278	0.790	0.512	0.118	0.786	0.596	0.253	0.860
0.584	0.916	0.495	1.268	0.828	0.272	1.270	0.958	0.446	1.381
0.669	1.341	0.761	1.843	1.209	0.458	1.856	1.393	0.680	2.008
0.766	1.835	1.072	2.505	1.646	0.675	2.529	1.894	0.950	2.728
0.877	2.390	1.425	3.246	2.135	0.920	3.279	2.452	1.254	3.530
1.005	3.009	1.818	4.070	2.674	1.193	4.107	3.071	1.592	4.419
1.151	3.700	2.253	4.994	3.272	1.496	5.026	3.760	1.968	5.407
1.318	4.468	2.727	6.030	3.933	1.828	6.045	4.524	2.381	6.507
1.510	5.307	3.229	7.176	4.653	2.184	7.154	5.358	2.824	7.710
1.729	6.207	3.750	8.425	5.426	2.559	8.343	6.256	3.290	9.006
1.981	7.157	4.277	9.766	6.243	2.946	9.597	7.205	3.771	10.377
2.269	8.146	4.800	11.191	7.097	3.341	10.904	8.201	4.259	11.811
2.599	9.166	5.313	12.695	7.987	3.739	12.259	9.237	4.747	13.301
2.976	10.215	5.807	14.274	8.910	4.134	13.660	10.314	5.229	14.845
3.409	11.296	6.282	15.938	9.871	4.523	15.120	11.439	5.699	16.453
3.905	12.421	6.738	17.707	10.882	4.904	16.664	12.625	6.158	18.149
4.472	13.607	7.176	19.606	11.960	5.275	18.322	13.892	6.604	19.965
5.122	14.874	7.599	21.673	13.124	5.637	20.138	15.264	7.039	21.945
5.867	16.251	8.010	23.960	14.402	5.991	22.168	16.772	7.465	24.147
6.720	17.770	8.414	26.524	15.821	6.339	24.477	18.445	7.887	26.639
7.697	19.457	8.813	29.425	17.407	6.685	27.134	20.309	8.310	29.491
8.816	21.338	9.213	32.722	19.183	7.033	30.202	22.383	8.740	32.773
10.097	23.435	9.622	36.468	21.165	7.390	33.740	24.680	9.189	36.547
11.565	25.771	10.053	40.711	23.374	7.770	37.797	27.215	9.674	40.867
13.246	28.377	10.531	45.487	25.834	8.194	42.412	30.015	10.226	45.770
15.172	31.295	11.096	50.813	28.581	8.696	47.601	33.122	10.893	51.265
17.377	34.584	11.818	56.659	31.665	9.332	53.342	36.609	11.754	57.307
19.904	38.312	12.817	62.929	35.145	10.196	59.554	40.571	12.941	63.773
22.797	42.555	14.305	69.432	39.090	11.438	66.073	45.127	14.667	70.442
26.111	47.371	16.647	75.884	43.556	13.297	72.646	50.391	17.257	76.993
29.907	52.779	20.427	81.937	48.574	16.118	78.950	56.432	21.161	83.054
34.255	58.722	26.446	87.255	54.119	20.328	84.648	63.202	26.896	88.276
39.234	65.040	35.512	91.592	60.089	26.323	89.459	70.463	34.850	92.432
44.938	71.461	47.869	94.852	66.286	34.266	93.227	77.753	44.994	95.465
51.471	77.643	62.461	97.102	72.439	43.873	95.951	84.468	56.637	97.493
58.953	83.243	76.800	98.525	78.245	54.379	97.766	90.050	68.484	98.736
67.523	88.006	88.086	99.349	83.435	64.760	98.880	94.197	79.078	99.441
77.340	91.811	94.953	99.787	87.833	74.087	99.511	96.940	87.367	99.815
88.583	94.678	98.375	100	91.372	81.882	99.842	98.578	93.210	100
101.460	96.700	99.661	100	94.057	87.847	100	99.441	96.803	100
116.210	98.033	100	100	95.977	92.048	100	99.837	98.702	100
133.103	98.867	100	100	97.290	94.834	100	100	99.555	100
152.453	99.369	100	100	98.172	96.645	100	100	99.884	100
174.616	99.674	100	100	98.786	97.848	100	100	100	100
200.000	99.870	100	100	99.235	98.672	100	100	100	100
229.075	100	100	100	99.578	99.240	100	100	100	100
262.376	100	100	100	99.849	99.648	100	100	100	100
300.518	100	100	100	100	99.874	100	100	100	100
344.205	100	100	100	100	100	100	100	100	100

APPENDIX B

MATLAB CODE FOR THE MARKOV CHAIN MODEL

Below is the source code of the Markov chain model identified for the "Normal Speed – Normal Air" (NSNA) operating conditions. Special thanks go to Guillaume Flandin for a very useful free utility that converts the input m-file into an rtf-file adding line numbering and highlighting comments, strings, and MATLAB keywords. The World Wide Web address of this utility is http://www.artefact.tk/software/matlab/highlight/.

```
001 % Markov Chain Model of a Finish Mill in a Closed Circuit (FM1300.m)
002 % Normal Speed - Normal Air (Day 1)
003
004 clear; % Clears all variables and matrices from memory
005 clf('reset'); % Clears the figure window and resets properties to default
006
007 % INPUT DATA
008
009 % F0 = PSD of Fresh Feed to the Entire Circuit
010 % Cumulative Percent Passing
011
012 %       Size    F0
013 %       [µm]    [%]
014 RF0=[
015         75      0.0
016         500     5.6
017         1168    7.9
018         2360    12.4
019         4750    22.8
020         9420    49.6
021         15900   75.8
022         32000   100.0
023 ];
024
025 % Load separator PSD's and GEC from F.txt file
026 load F.txt;
027
028 % Column 1: Sieve sizes [µm]
029 % Column 2: F1 [%] = PSD of Separator Feed
```

```
% Column 3: F2 [%] = PSD of Rejects
% Column 4: F3 [%] = PSD of Fine Product
% Column 5: GEC [%] = Grade Efficiency Curve
%           All Cumulative Percent Passing

x=RF0(:,1)'; % Experimental sieves for Fresh Feed F0
ne=length(x); % Number of experimental sieves for Fresh Feed F0
F0e=0.01*RF0(:,2)'; % Fresh Feed F0 cumulative values (fractions)
% figure(2);semilogx(x,F0e,'*'); grid on; hold on;

x_exp=F(:,1)'; % Experimental sieve grid for F1, F2, F3 PSDs
n_exp=length(x_exp); % Number of experimental sieves for F1, F2, F3
F1e=0.01*F(:,2)'; % Experimental F1
F2e=0.01*F(:,3)'; % Experimental F2
F3e=0.01*F(:,4)'; % Experimental F3
Fie=0.01*F(:,5)'; % Experimental Grade Efficiency Curve -GEC- of separator (inversion of Tromp)

figure(1); % F1, F2, F3 plots
semilogx(x_exp,F1e,'bp'); hold on; % Separator Feed F1 plot
semilogx(x_exp,F2e,'*','Color',[0 0.5 0]); hold on; % Rejects F2 plot
semilogx(x_exp,F3e,'r^'); hold on; % Fines F3 plot
axis([0.3 400 0 1]);
% Fines F3 PSD on a separate graph
% figure(2);semilogx(x_exp,F3e,'r^'); grid on; hold on; axis([0.3 400 0 1]);

% Determining mean experimental sieve sizes (n_exp-1)
for i=1:n_exp-1
    xe_mean(i)=(x_exp(i+1)+x_exp(i))/2; % Center between two adjacent experimental sieves
end

% Matching GEC values with the experimental sieve sizes
Fie=[Fie(1) Fie]; % One extra point to the left at the same value as the first point Fie(1)
% Abscissa of GEC extends outside from the first computational sieve (to the left)
xe_or=[0.001 x_exp]; % Using experimental sieves
% xe_or=[0.001 xe_mean x_exp(n_exp)]; % Using mean experimental sieves (an extra point on the right)
nefi=length(xe_or); % Number of experimental sieves for GEC
% figure(2);semilogx(xe_or,Fie,'rv-'); grid on; hold on;

% Experimental Blaine value from laboratory F3 PSD, [m^2/kg]
rho=3054.9; % Density of cement for Blaine calculation, [kg/m^3]
Blaine_exp=0;
for i=1:(n_exp-1)
    Blaine_exp=Blaine_exp+6*(F3e(i+1)-F3e(i))*log(x_exp(i+1)/x_exp(i))/(rho*(x_exp(i+1)-x_exp(i))*1e-6);
    % [m^2/kg] = [m^2/kg]       [fraction]                          /([kg/m^3] * [m] * µm-to-m-coef)
end

% Experimental cumulative percent passing through sieve #325 (45 µm) from F3 PSD
```

```
Sieve45_exp=0;
for i=1:n_exp
    if x_exp(i+1)>45
        Sieve45_exp=100*(F3e(i)+(F3e(i+1)-F3e(i))*(45-x_exp(i))/(x_exp(i+1)-x_exp(i))); break;
    end
end

% CALIBRATION PARAMETERS

Result_matrix=[]; % Matrix to be filled with the best model parameters
err_min=10^6; % Initial minimal error in search for the best model parameters (any large number)
xminBl=[]; % Matrix to be filled with the best xMin value to match Blaine
errBl_min=10^6; % Initial minimal error in search for xMin (any large number)
B3_B0=0.0001; % Target error in calculating the difference between B3 and B0

x50_e=32.96; % Experimental cut size (x50) by interpolation of GEC
x50=x50_e; % Separator cut sizes that define a set of Grade Efficiency Curves - possibly: range with a step
B0_e=84.1; % Experimental fresh feed rate
B0=B0_e; % Fresh feed flow rates - possibly: range with a step, e.g., 80:1:90

% Parameters of the computational sieve grid 'xm'
nm=41; % Number of computational sieves, (nm+1) gives the largest sieve
xe1=F(1,1); % First experimental sieve, [µm]
xMin=xe1; % First computational sieve, or xm(1)

% Selection function - defines the portion of material that leaves the fraction: s=alf*(x/x_max)^bet
alf=13.82; % Parameter of Selection function
bet=1; % Power index of Selection function: 1 = Rittinger's Law; 0.5 = Bond's Law
dt=1; % Time step in Selection function

% Parameters of the Grinding Matrix
BpitR=53.655; % Reference time in power index of matrix of Grinding; units of Feed flow
k=150; % Power index of grinding matrix G, or ~ number of Markov chain cells

% Parameters of the breakage function b(x)=integral of f(p,q,r,x)
p1=0.0103; p2=0.026; q1=10; q2=15; % For double-step breakage function
p=p1; q=q1; r=0; % Power, exponential, and other functions

% CALCULATION

for calc=1:1

% Do not randomize parameters when only one cycle is calculated
if calc ~= 1 % Not equal to one
    % alf=1+rand*20; % 1 .. 21
    % p1=0.00001+rand*0.1;
    % p2=0.01+rand*0.02; % 0.01 .. 0.03
```

```
    % q1=1+round(rand*15); % 1 .. 16
    % q2=17+round(rand*15); % 17 .. 31
    % r=0.1+rand*5; % 0.1 .. 5.1
    % bet=0.9+rand*0.2; % 0.9 .. 1.1
    % dt=0.95+rand*0.1; % 0.95 .. 1.05
    % BpitR=45+rand*15; % 45 .. 60
    % k=100+round(rand*200); % 100 .. 200
    % xMin=0.1+rand*0.25; % 0.1 .. 0.35
    % if xMin < xe1 xMin=xMin; else xMin=xe1; end
end

    xm=[]; % Vector of computational sieves - clearing vector and reseting its size
    xm1=[]; % Vector of mean computational sieves
    dx=[]; % Width of fraction (they maybe different, e.g., log scale, sqrt scale)

    % Defining computational sieves 'xm' starting with 2nd (first one is xMin)
    % Vector of computational sieves xm [µm] is based on sqrt(2) progression:
    % [xMin, coef * {1, sqrt(2), 2, sqrt(8),...}]
    for i=2:nm+1 % (nm+1) is required to calculate the last computational sieve
        xm(i)=xMin+0.05*2^((i-2)/2); % For nm=41
        % xm(i)=xMin+0.05*2^((i-2)/6); % For nm=119
    end
    % Defining fraction widths 'dx' in the computational sieve grid
    for i=2:nm
        dx(i)=xm(i+1)-xm(i); % Fraction width
        xm1(i)=(xm(i+1)+xm(i))/2; % Center of each fraction
    end
    % Assigning xMin to the FIRST computational sieve
    xm(1)=xMin; % First computational sieve = xMin [µm] for current iteration
    dx(1)=xm(2)-xm(1); % Width of the first fraction
    xm1(1)=(xm(2)+xm(1))/2; % Center of the first fraction

    % Converting cumulative passing values of F0 to the computational sieves grid - Fm

    Fm=zeros(nm+1,1); % Re-zeroing Fm vector defined for the computational sieves
    for i=1:nm+1 % Cycle for computational sieves
        for j=1:ne-1 % Cycle for experimental F0 sieves
            if xm(i)<=x(j+1)
                if xm(i)>=x(j)
                    Fm(i)=F0e(j)+(F0e(j+1)-F0e(j))*(xm(i)-x(j))/(x(j+1)-x(j)); % Linear interpolation
                end
            end
            if xm(i)>x(ne) % Computational sieves above experimental sieves
                Fm(i)=1; % Cumulative passing values through the largest sieves = 100%
            end
        end
    end
```

```
% figure(2);semilogx(x,F0e,'bo',xm,Fm,'r*-'); grid on; hold on; axis([10 100000 0 1]);

f00=[]; % Initial portion of the Fresh Feed material in each fraction (i)
for i=1:nm
    f00(i)=Fm(i+1)-Fm(i);
end

% Converting experimental F1, F2, F3 to the computational sieves grid - F1m, F2m, F3m

F1m=zeros(nm+1,1);F2m=zeros(nm+1,1);F3m=zeros(nm+1,1); % Re-zeroing vectors defined for the computational sieves
for i=1:nm+1 % Cycle for computational sieves
    for j=1:n_exp-1 % Cycle for experimental F0 sieves
        if xm(i)<=x_exp(j+1)
            if xm(i)>=x_exp(j)
                F1m(i)=F1e(j)+(F1e(j+1)-F1e(j))*(xm(i)-x_exp(j))/(x_exp(j+1)-x_exp(j));
                F2m(i)=F2e(j)+(F2e(j+1)-F2e(j))*(xm(i)-x_exp(j))/(x_exp(j+1)-x_exp(j));
                F3m(i)=F3e(j)+(F3e(j+1)-F3e(j))*(xm(i)-x_exp(j))/(x_exp(j+1)-x_exp(j));
            end
        end
        if xm(i)>x_exp(n_exp) % Computational sieves above experimental sieves
            F1m(i)=1; F2m(i)=1; F3m(i)=1; % Cumulative passing values through the largest sieves = 100%
        end
    end
end
% figure(2);semilogx(x_exp,F1e,'bp',xm,F1m,'co-'); grid on; hold on;
          % semilogx(x_exp,F2e,'g*',xm,F2m,'go-'); grid on; hold on;
          % semilogx(x_exp,F3e,'r^',xm,F3m,'mo-'); grid on; hold on; axis([0.3 400 0 1]);

% Selection Function
for i=1:nm
    s(i)=alf*(xm(i)/xm(nm))^bet;
    if s(i)>1; s(i)=1;end; % Selection Function cannot be > 1
end
s(1)=0; % The smallest fraction does not break down!

% Matrix of Grinding
G1=[]; b=[];
for j=2:nm % Fractions being ground (smallest fraction j=1 is not ground)
    for i=1:nm % Fractions receiving ground material
        G1(i,j)=0;
        if i==j % Diagonal of matrix
            G1(i,j)=1-s(j)*dt; % Material, remained in fraction (j)
        end
        if i<j % That is, row < column, i.e., in the upper triangle of the matrix

            % Distribution breakage function

```

```
% Power distribution function: db/dx=r+p*x^q (If q=0, then even distribtion)
% h=xm(j)-xm(1);
% s1=(p/(q+1))*(h^(q+1));
% s2=r*h;
% a1=(p/(q+1))*((xm(j)-xm(i))^(q+1)-(xm(j)-xm(i)-dx(i))^(q+1));
% a2=r*dx(i);
% b(i,j)=(a1+a2)/(s1+s2); % Area for width dx(i) wrt total area under the curve

      % Exponential distribution function: db/dx=p*exp(q*x)
      % h=xm(j)-xm(1);
      % s1=(p/q)*(exp(q*h)-1);
      % a1=(p/q)*(exp(q*(xm(j)-xm(i)))-exp(q*(xm(j)-xm(i)-dx(i))));
      % b(i,j)=a1/s1; % Area for width dx(i) wrt total area under the curve

% Step distribution function: b=p*[x(q)-x(1)] + (1-p)*[x(j)-x(q)]
% if j<=q
%    b(i,j)=dx(i)/(xm(j)-xm(1));
% else
%    if i<q
%        b(i,j)=dx(i)*p/(xm(q)-xm(1));
%    else
%        b(i,j)=dx(i)*(1-p)/(xm(j)-xm(q));
%    end
% end

      % Double step distribution function
      if j<=q1
          b(i,j)=dx(i)/(xm(j)-xm(1));
      elseif j>q1 & j<=q2
          if i<q1
              b(i,j)=dx(i)*p1/(xm(q1)-xm(1));
          elseif i<q2 & i>=q1
              b(i,j)=dx(i)*(1-p1)/(xm(j)-xm(q1));
          end
      elseif j>q2
          if i<q1
              b(i,j)=dx(i)*p1/(xm(q1)-xm(1));
          elseif i<q2 & i>=q1
              b(i,j)=dx(i)*p2/(xm(q2)-xm(q1));
          elseif i>=q2
              b(i,j)=dx(i)*(1-(p1+p2))/(xm(j)-xm(q2));
          end
      end

% Even distribution breakage function (no p,q,r parameters)
% b(i,j)=dx(i)/(xm(j)-xm(1)); % The ground material in fraction (j) is evenly
% distributed along xm(j)-xm(1), and the smaller fractions (i) receive portions
```

```
                % of that ground material in proportion to their fraction widths, dx(i)

                G1(i,j)=b(i,j)*s(j)*dt;
            end
        end
    end
    G1(1,1)=1; % The smallest fraction stays within itself
    G1=G1^k; % Grinding effort of all Markov chain cells, k

    % Shifting Grade Efficiency Curve using different trial cut sizes, x50

    for x50_it=1:length(x50) % Counter for different x50

        % Grade efficiency curve of separator Fie in the computational sieves grid - Fi

        Fi=zeros(nm,1); % Re-zeroing GEC vector defined for the computational sieves
        xe=xe_or*x50(x50_it)/x50_e; % Normalization wrt experimental cut size, x50_e, and
                                    % transition to a new cut size defined by x50
        for i=1:nm % Cycle for computational sieves
            for j=1:nefi-1 % Cycle for experimental GEC sieves
                if xm(i)<=xe(j+1)
                    if xm(i)>=xe(j)
                        Fi(i)=Fie(j)+(Fie(j+1)-Fie(j))*(xm(i)-xe(j))/(xe(j+1)-xe(j));
                    end
                end
                if xm(i)>xe(nefi) % Computational sieves above experimental sieves
                    Fi(i)=0; % Probability of big stones to become fine product = 0%
                end
            end
        end
        figure(1); % GEC plots
        semilogx(xe_or,Fie,'bO'); hold on; % Original GEC
        semilogx(xm(1:nm),Fi,'-','Color',[0 0.5 0]); hold on; % Computational GEC
        % figure(3);semilogx(xe_or,Fie,'bo',xm(1:nm),Fi,'r*-'); grid on; hold on; axis([0.3 400 0 1]);

        % Matrix of Classification
        C2=[];
        for i=1:nm
            for j=1:nm
                C2(i,j)=0;
                if i==j; C2(i,j)=Fi(i); end % Diagonal matrix of GEC
            end
        end

        f0=[];f1=[];f2=[];f3=[]; % Differential PSD's in [ton]
        F1new=zeros(nm+1,1);F2new=zeros(nm+1,1);F3new=zeros(nm+1,1); % New calculated cumulative PSD's

```

```
312         % Main Calculations
313
314         for B0_it=1:length(B0) % Counter for different Fresh Feed values
315
316             % On the first interation - into an empty mill
317             f0=B0(B0_it)*f00'; % Differential PSD of the Fresh Feed into the circuit [ton]
318             fpit=f0; % Same input into the empty mill
319             B1=B0(B0_it); % Flow rate into the empty mill; later on - throughput
320             B3=0; % Product flow from the separator (empty mill)
321             istop=0; % Iteration counter
322             I=eye(nm);
323
324             while (abs(B3-B0(B0_it))/B0(B0_it)) > B3_B0
325                 istop=istop+1; % Counter
326                 if istop > 200; break; end; % Not more than 200 iterations
327                 f1=(G1^(BpitR/B1))*fpit; % Grinding action; BpitR/B1 = Ratio of the feed residence times
328                 % Reference throughput over actual throughput = Actual time over reference time
329                 f3=C2*f1; % Classification; Fines PSD [ton]
330                 f2=(I-C2)*f1; % Classification; Rejects PSD [ton]
331                 fpit=f0+f2; % New input to the mill PSD [ton]
332                 B1=sum(fpit); % Throughput [ton]
333                 B3=sum(f3); % Product flow [ton]
334             end
335             B2=sum(f2); % Rejects flow [ton]
336             F1new=[0; cumsum(f1)/B1]; % New cumulative F1 with a shift to the right by one sieve
337             F2new=[0; cumsum(f2)/B2]; % New cumulative F2 with a shift to the right by one sieve
338             F3new=[0; cumsum(f3)/B3]; % New cumulative F3 with a shift to the right by one sieve
339
340             % Blaine value using calculated Fine Product PSD
341             Blaine=0;
342             for i=1:nm
343                 Blaine=Blaine+6*f3(i)*log(xm(i+1)/xm(i))/(B3*rho*(xm(i+1)-xm(i))*1e-6);
344                 % [m^2/kg] =    [ton]                  /([ton]*[kg/m^3]*[m]*µm-to-m)
345             end
346             % Finding xMin providing Blaine value close to the experimental one
347             errBl=0;
348             errBl=abs(Blaine_exp-Blaine); % Error between exp. and calc. Blaine values
349             if errBl < errBl_min % Search for minimal error
350                 errBl_min=errBl;
351                 xminBl=[xminBl; Blaine xMin];
352             end
353
354             % Cumulative percent passing through sieve #325 (45 µm) using calculated Fine Product PSD
355             Sieve45=0;
356             for i=1:nm
357                 if xm(i+2)>45
358                     Sieve45=100*(sum(f3(1:i))+f3(i+1)*(45-xm(i+1))/(xm(i+2)-xm(i+1)))/B3;
```

```
                    break;
                end
            end

            % Error Estimation - Least Square Method
            err=0; err1=0; err2=0; err3=0;
            for i=1:nm+1 % Estimation throughout all (nm+1) computational sieves
                err1=(F1new(i)-F1m(i))^2; % Error contributed by F1 PSD
                err2=(F2new(i)-F2m(i))^2; % Error contributed by F2 PSD
                err3=(F3new(i)-F3m(i))^2; % Error contributed by F3 PSD
                err=err+err1+err2+err3;
            end
            if err < err_min % Search for the minimal error
                err_min=err;
                Result_matrix=[Result_matrix; % Construction of the Results matrix
                    % err_min alf bet BpitR p1 p2 q1 q2; % First line of data into the Result_matrix
                    err_min alf bet BpitR k p q dt; % First line of data into the Result_matrix
                    xMin x50(x50_it) B0(B0_it) B3 B2 Blaine Sieve45 istop]; % Second line of data
            end

            % Calculated F1, F2, and F3 curves
            figure(1); semilogx(xm,F1new,'c-','linewidth',2.5); hold on; % Calculated F1 curve
            figure(1); semilogx(xm,F2new,'g-','linewidth',2.5); hold on; % Calculated F2 curve
            figure(1); semilogx(xm,F3new,'m-','linewidth',2.5); hold on; % Calculated F3 curve
                % figure(2); semilogx(xm,F3m,'bo',xm,F3new,'rx-'); grid on; hold on; axis([0.3 400 0 1]);
            axis([0.3 400 0 1]);

        end % Different B0 cycle
    end % Different x50 cycle
end % Calc cycle

% Text Output on the Graph

ErrSiz=size(Result_matrix,1); % Number of rows in Result_matrix
figure(1); grid on; xlabel('Particle Size, \mum'); ylabel('Cumulative Passing, fraction');
set(figure(1),'DefaulttextBackground','White');
set(figure(1),'DefaulttextFontName','Lucida Console');
set(figure(1),'DefaulttextFontSize',9);

text(0.32,0.95,' NSNA (Day 1) ','Color',[0 0.5 0]);

% labels1=[' err =   ';' alf =   ';' bet =   ';' BR  =   ';' p1  =   ';' p2  =   ';' q1  =   ';' q2  =   '];
labels1=[' err =   ';' alf =   ';' bet =   ';' BR  =   ';' k   =   ';' p   =   ';' q   =   ';' dt  =   '];
text(0.32,0.55,labels1);
text(0.70,0.55,num2str(Result_matrix(ErrSiz-1,:)','%-8.4g')); % Next to the last row of Result_matrix displayed as column

labels2=[' xm1 =    ';' x50 =    ';' B0  =    ';' B3  =    ';' B2  =    ';' Bla =    ';' #45 =    ';' Ite =    '];
```

```
406 text(1.70,0.55,labels2);
407 text(3.80,0.55,num2str(Result_matrix(ErrSiz,:)','%-7.5g')); % The last row of Result_matrix displayed as column
408
409 text(0.32,0.30,[' Blaine PSD =     ';' Sieve #45  =     '],'Color','Red'); % Experimental Blaine and Sieve 45µm
410 text(1.63,0.30,num2str([Blaine_exp;Sieve45_exp],'%-5.5g'),'Color','Red');
411
412 % Data Output
413
414 % ['    err_min' '    alf' '      bet' '      BR' '      k    ' '      p' '        q' '           r    ';
415 %  '    xMin' '      x50 ' '     B0' '       B3' '      B2' '      Blaine' '    Sieve45  ' 'Iterations']
416 % Result_matrix
```

VITA

Name:	Gleb Gennadievich Mejeoumov
Address:	Zachry Department of Civil Engineering c/o Dr. Dan Zollinger Texas A&M University, MS 3136 College Station, TX 77843-3136
E-mail:	gleb @ tamu.edu

Education:

- B.S. in Electromechanical Engineering from Ivanovo State Power University, Russia, 1998
- M.S. in Electromechanical Engineering from Ivanovo State Power University, Russia, 2000
- Ph.D. in Civil Engineering from Texas A&M University, USA, 2007

Research Interests:

- Industrial process control and optimization
- Manufacturing equipment: simulation and analysis
- Product development and research
- Material science: cement and fly ash

Gleb Gennadievich Mejeoumov was born and raised in Russia, in the city of Ivanovo, located approximately 320 km (200 miles) north-east of Moscow. He received his Bachelor of Science degree in electromechanical engineering from Ivanovo State Power (Engineering) University, Russia in June 1998. He then entered the master's program at the same university and obtained the Master of Science degree in the abovementioned engineering field in June 2000. In September that year, Mr. Mejeoumov continued at his alma mater with a Ph.D. program with the emphasis on powder science and grinding technology. While maintaining close ties with his academic advisors at Ivanovo State Power (Engineering) University, Mr. Mejeoumov formally left the program in August 2001 to become a doctoral student at Texas A&M University in the Department of Civil Engineering with specialization in material science.